

Multi-sensor Attitude and Heading Reference System Design using Genetically  
Optimized Kalman Filter

by

Meron Gessesse

A thesis submitted to the Faculty of Graduate and Postdoctoral Affairs in partial  
fulfillment of the requirements for the degree of

Master of Science

in

Electrical and Computer Engineering

Carleton University  
Ottawa, Ontario

©2018, Meron Gessesse

## **Abstract**

Attitude and Heading Reference System (AHRS) is a self-contained sensors assembly that can estimate full 3D orientation of an object. 3D orientation estimation is of great importance in many applications such as robot navigation, augmented/virtual reality, and mobile mapping. The AHRS system model involves integration of angular rate measurements from gyroscope which are fused with absolute measurements from magnetometer/accelerometer using Extended Kalman Filter (EKF). EKF accuracy is greatly affected by process noise parameters and measurement noise parameters. Therefore, this thesis developed a systematic method of EKF noise parameters optimization using a hybrid stochastic, Genetic Algorithms (GA)-based approach supported by Design of Experiments (DoE) technique. Noise parameters are partially obtained using stochastic modeling methods such as Gauss-Markov (GM) and Allan Variance (AV). Then, further optimization is performed using GA and DoE methods. The proposed approach has been developed in MATLAB and tested on simulation data and verified on real data collected under different scenarios. Results showed that the proposed approach can provide 40-60% better accuracy compared to conventional methods within few GA iterations. In addition, application of DoE technique reduces GA iterations to convergence by approximately 60%.

## **Acknowledgements**

I am always grateful for God's unconditional love and abundant grace. First and foremost, I would like to show my gratitude to my research advisor, Dr. Mohamed Atia, for his constant support and kindness. I am glad that I worked under Dr. Atia's supervision. This thesis would not have been possible without his assistance. I would also like to thank my family and friends for their unwavering support over the years. They have always been there to encourage and motivate me. Finally, I would like to thank EMS lab team members for their help and support and for providing valuable feedback and recommendations.

# Table of Contents

<b>Abstract.....</b>	<b>2</b>
<b>Acknowledgements .....</b>	<b>3</b>
<b>List of Tables .....</b>	<b>6</b>
<b>List of Figures.....</b>	<b>7</b>
<b>List of Acronyms .....</b>	<b>11</b>
<b>1 Chapter: Introduction .....</b>	<b>13</b>
1.1 Motivation .....	13
1.2 Problem Statement .....	14
1.3 Previous Work.....	15
1.4 Thesis Objectives .....	16
1.5 Contributions.....	17
1.6 Thesis organization .....	18
<b>2 Chapter: MEMS based IMUs .....</b>	<b>20</b>
2.1 MEMS IMU components.....	21
2.2 Examples of MEMS IMUs and Their Applications .....	24
2.3 MEMS IMU Measurements Errors .....	25
2.4 Error Analysis of MEMs IMUs using Allan Variance and Gauss-Markov Methods .....	30
2.5 Analysis of the MPU-9250 MEMS IMU used in This Research .....	33
<b>3 Chapter: AHRS using MEMS IMU .....</b>	<b>39</b>
3.1 Reference Frames.....	39
3.2 Orientation Representation and Coordinate Transformation .....	41
3.3 AHRS System Model.....	45
3.4 Absolute Tilt calculation from accelerometer .....	50
3.5 Absolute Heading Calculation from Magnetometer .....	52

3.6	Integrated AHRS using Extended Kalman Filter (EKF).....	54
<b>4</b>	<b>Chapter: AHRS using Genetically Optimized Kalman Filter .....</b>	<b>61</b>
4.1	Nominal Design Point .....	61
4.2	EKF Performance using the Nominal Design Point.....	61
4.3	Design of Experiment Analysis.....	65
4.4	Optimizing the EKF parameters using Genetic Algorithms .....	68
4.5	Application of GA to EKF-based AHRS .....	75
<b>5</b>	<b>Chapter: Simulation and Experimental Results .....</b>	<b>76</b>
5.1	Simulation Test .....	76
5.2	Zero-speed Experimental Test .....	86
5.3	Dynamic Physical Test.....	96
5.4	Comment on Execution Time and Error values .....	102
<b>6</b>	<b>Chapter: Conclusion.....</b>	<b>104</b>
6.1	Contributions.....	105
6.2	Future work .....	107
	<b>References .....</b>	<b>108</b>

## List of Tables

Table 2-1: GM estimated time constant and standard deviation.....	36
Table 2-2: Random Walk Values as estimated by AV test.....	37
Table 4-1: Simulation Test: EKF-Performance using Nominal Design Parameters .....	63
Table 4-2: Zero-speed experimental Test: Nominal Design Parameters .....	65
Table 4-3: Low and High Setting for the factors .....	66
Table 4-4: Error values for changing the R matrix .....	66
Table 4-5: Basic GA Algorithm.....	70
Table 4-6: GA Selection .....	73
Table 4-7: GA Crossover .....	73
Table 4-8: GA Mutation.....	74
Table 5-1: Gyro and Accelerometer Noise parameters.....	77
Table 5-2: Performance of the EKF using nominal design parameters .....	80
Table 5-3: EKF-Performance using GA without DoE for the simulation test.....	85
Table 5-4: EKF-Performance using GA with DoE the simulation test .....	85
Table 5-5: GM-Estimated Noise Parameters .....	88
Table 5-6: EKF results for zero-speed experimental test using nominal design point .....	90
Table 5-7: EKF-Performance using GA without DoE for the Physical Stationary Test .....	93
Table 5-8: Performance of DoE-supported GA for zero-speed experimental test.....	95
Table 5-9: EKF Results for dynamic experimental test using nominal design point .....	98
Table 5-10: EKF-Performance for dynamic experimental Test .....	102
Table 5-11: Information summary of all experiments .....	103

## List of Figures

Figure 1-1: Simple block diagram of AHRS .....	15
Figure 2-1. Typical IMU Components.....	22
Figure 2-2: Typical accelerometer with proof mass along sensitive axis .....	23
Figure 2-3: Typical Gyroscope Diagram when angular velocity is applied .....	24
Figure 2-4. Examples of MEMS IMUs.....	25
Figure 2-5. Sensor input versus output with a bias error .....	26
Figure 2-6: Scale factor error .....	27
Figure 2-7: Misalignment of sensor sensitive axes with respect to the body frame .....	27
Figure 2-8. One Minute Record of Stationary Gyro Data measured by MPU-9250 IMU. ....	29
Figure 2-9. Result of integrating gyro random walk for one minute at 100Hz rate. ....	29
Figure 2-10: Autocorrelation of 1 <sup>st</sup> Order Gauss Markov Process .....	31
Figure 2-11: Allan curve for gyroscope.....	33
Figure 2-12: SparkFun 9DoF Razor IMU M0 and the sensing axes .....	34
Figure 2-13: Sample stationary data collected by gyro .....	34
Figure 2-14: Sample stationary data collected by accelerometer .....	35
Figure 2-15. GM Autocorrelation Sequence of Gyro .....	36
Figure 2-16: GM Autocorrelation Sequence of Accelerometer.....	36
Figure 2-17: Allan Variance results for x-axis of the MPU9250 IMU gyroscope .....	37
Figure 2-18: Allan Variance results for y-axis of the MPU9250 IMU gyroscope .....	37
Figure 2-19: Allan Variance results for z-axis of the MPU9250 IMU gyroscope.....	38
Figure 3-1: The local-level ENU reference frame in relation to the ECI and ECEF frames.....	41
Figure 3-2. Bias and Random noise error .....	47

Figure 3-3: Ground-truth Simulated Angles .....	49
Figure 3-4: Roll angle drifts of AHRS System Model in 60 seconds.....	50
Figure 3-5: Pitch angle drifts of AHRS System Model in 60 seconds .....	50
Figure 3-6: Heading angle drifts of AHRS System Model in 60 seconds .....	50
Figure 3-7: Absolute Roll calculated from noisy Accelerometer data .....	51
Figure 3-8: Absolute Pitch calculated from noisy Accelerometer data .....	52
Figure 3-9: Mag-estimated Heading on Simulated Data .....	54
Figure 3-10: Block diagram of AHRS-EKF .....	59
Figure 4-1: Roll error of simulation data using nominal design point.....	62
Figure 4-2: Pitch error of simulation data using nominal design point .....	62
Figure 4-3: Heading error of simulation data using nominal design point .....	63
Figure 4-4: Roll error of zero-speed physical data using nominal design point.....	64
Figure 4-5: Pitch error of zero-speed physical data using nominal design point.....	64
Figure 4-6: Heading error of zero-speed physical data using nominal design point .....	64
Figure 4-7: Main Effects of $R$ parameters variations.....	68
Figure 4-8: Basic structure of Genetic Algorithm .....	70
Figure 4-9: Roulette wheel selection .....	72
Figure 4-10: GA Illustrative Example: maximizing a simple function .....	74
Figure 4-11: The proposed EKF tuning procedure .....	75
Figure 5-1: Ground Truth Simulated Angle.....	76
Figure 5-2: Portion of simulated noisy raw gyro stationary output .....	77
Figure 5-3: Portion of simulated noisy raw accelerometer stationary output.....	78
Figure 5-4. Portion of Simulated Raw Magnetometer Data .....	78

Figure 5-5: Heading performance using nominal design point .....	79
Figure 5-6: Pitch performance using nominal design point.....	79
Figure 5-7: Roll performance using nominal design point .....	80
Figure 5-8: DoE Pareto Charts for the Q and R parameters of the Simulation Test.....	81
Figure 5-9: Heading angle output from GA only.....	82
Figure 5-10: Pitch output from GA only on simulation data .....	82
Figure 5-11: Roll output from GA only on simulation data .....	83
Figure 5-12: Best, worst and Mean scores for twenty generations of GA.....	83
Figure 5-13: Best and Mean fitness values for GA optimization on simulation data.....	84
Figure 5-14: Comparison of GA fitness values with and without DoE.....	86
Figure 5-15: Raw Gyro data of the Experimental Zero-speed Test.....	87
Figure 5-16: Raw Accelerometer data of the Zero-speed Test .....	87
Figure 5-17: Raw Magnetometer data of the Experimental Zero-speed Test.....	87
Figure 5-18. Ground-Truth Angles to evaluate the proposed EKF-design.....	88
Figure 5-19: Heading results for zero-speed experimental test using nominal design point.....	89
Figure 5-20: Roll results for zero-speed experimental test using nominal design point .....	90
Figure 5-21: Pitch results for zero-speed experimental test using nominal design point .....	90
Figure 5-22: Gyro biases estimation for the zero-speed experimental test.....	91
Figure 5-23: DoE Pareto Charts for the Q and R parameters of zero-speed experimental test ....	92
Figure 5-24: Best, worst and Mean scores for twenty generations of GA.....	93
Figure 5-25: Best and Mean fitness values for GA optimization .....	93
Figure 5-26: GA fitness with and without DoE for the zero-speed experimental test.....	94
Figure 5-27: Fitness Value Statistics of GA with DoE.....	95

Figure 5-28: 2D trajectory taken in the dynamic test .....	96
Figure 5-29: Ground-truth heading of the dynamic test .....	96
Figure 5-30: Ground-truth roll/pitch in the dynamic test.....	97
Figure 5-31: Raw gyroscope data of the dynamic test.....	97
Figure 5-32: Raw X,Y accelerometer data of the dynamic test.....	98
Figure 5-33: DoE Analysis for the dynamic experimental test.....	99
Figure 5-34: Fitness Statistics of DoE-supported GA applied on dynamic experimental data ..	100
Figure 5-35: Heading output for the dynamic physical test using GA with DoE.....	100
Figure 5-36: Pitch output for the dynamic experimental test using GA with DoE.....	101
Figure 5-37: Roll output for dynamic experimental test using GA with DoE.....	101
Figure 5-38: Gyro biases for the dynamic test.....	102

## List of Acronyms

<b>Acronym</b>	<b>Definition</b>
ARW	Angle Random Walk
AHRS	Attitude Heading Reference System
AV	Allan Variance
CZM	Conventional Zero Meridian
DCM	Direction Cosine Matrix
DoE	Design of Experiment
EKF	Extended Kalman Filter
ECEF	Earth Centered Earth Fixed
ECI	Earth Centered Inertial
ENU	East North Up
GA	Genetic Algorithm
GM	Gauss Markov
GNSS	Global Navigation Systems
GPS	Global Position System
HMM	Hidden Markov Model
IMU	Inertial Measurement Unit
INS	Inertial Navigation Systems
KF	Kalman filter
MEMS	Micro Electronic Mechanical Systems
NED	North East Down

NWU	North West Up
PSD	Power Spectral Densities
RMS	Root Mean Squared
RMSE	Root Mean Squared Error
RF	Radio Frequency
SWD	South West Down

# 1 Chapter: Introduction

## 1.1 Motivation

Attitude and Heading Reference System (AHRS) consists of inertial measurement unit (IMU) and basic sensor-fusion firmware that estimates the attitude and heading of a platform. Recently, low-cost IMUs that include gyroscopes, accelerometers, supported by magnetometers became available thanks to Micro-electromechanical systems (MEMS) technology. AHRS utilizes Kalman Filter (KF) as an efficient method to estimate the state of a stochastic system by minimizing the mean of the squared errors related with the integration of accelerometers, gyroscopes, magnetometers and Global Navigation Satellite Systems (GNSS) such as Global Positioning Systems (GPS) (if available). KF is computationally efficient fusion algorithm compared to other common methods such as Unscented KF [1] and Particle Filter (PF) [2]. However, the accuracy of KF is dependent on accurate knowledge of noise parameters. Noise parameters consist of process noise covariance and measurement noise covariance. Although KF noise parameters can be partially approximated by Allan Variance (AV) and Gauss-Markov (GM) methods, in practice, the noise parameters need further optimization (i.e. tuning) to generate better results. Further optimization is commonly performed by experts following a kind of a trial-and-error manual approach which is time consuming and typically does not result in the best performance. Therefore, these limitations motivated us to develop a more systematic and efficient KF tuning method. Since KF parameter tuning problem lacks a closed form solution, the developed tuning procedure in this thesis combines stochastic methods (AV and GM) with evolutionary techniques (Genetic Algorithms “GA”) supported by Design of Experiments (DoE) approach.

## 1.2 Problem Statement

MEMS devices feature tiny structural part that can move, bend, stretch, deform and may contact each other [3, 4, 5]. They are quite significant as they promise smaller and cheaper systems. However, due to large MEMS noises, the stand-alone use of MEMS sensors in AHRS and other positioning systems such as inertial navigation system (INS) may deliver kilometer level positioning errors for the applications of several seconds duration [6, 7]. Thus, there is a need to improve the performance of MEMS based IMUs. This can be achieved by combining MEMS based IMUs with magnetometer data [6].

KF techniques help in combining different measurements in such a way that individual sensor shortcomings are minimized and, as a result, errors are reduced [8, 9, 10, 11]. The KF has a criterion of minimizing the mean squared error, and was designed for linear systems, however most practical systems are nonlinear [12]. So, an Extended Kalman filter (EKF) is used for nonlinear plant models [13]. EKF involves the linearization of system dynamic equation (system model) using first order Taylor series approximation through a prediction and update cycle [14, 15, 16]. Therefore, EKF is used to develop accurate and efficient AHRS.

Figure 1-1 illustrates the block diagram of a basic EKF based AHRS framework with the noise parameters are illustrated. The accuracy of the EKF greatly depends on the designed noise parameters. In the context of the AHRS integration, the process noise reflects the system noise associated with MEMS based gyroscope errors while the measurement noise represents the covariance matrix of the noise associated with roll and pitch updates from the MEMS based accelerometer and heading update from a magnetometer sensor. The noise parameters should be

adequately tuned to match the designed system to the real operational condition and, ideally can create the best possible outcome from the EKF integration.

There are some popular approaches that have been adopted in the literature for stochastic modeling of IMU errors. The most common methods are GM and AV techniques [8, 17]. However, less attention has been paid to the tuning of the EKF parameters in a systematic and optimized way. In this thesis, we overcome the current limitations in EKF parameter tuning such as mismatch between the actual covariance matrix and the ones obtained from error modelling, and the mismatch caused by disturbance or change in environment matches the real phenomenon.

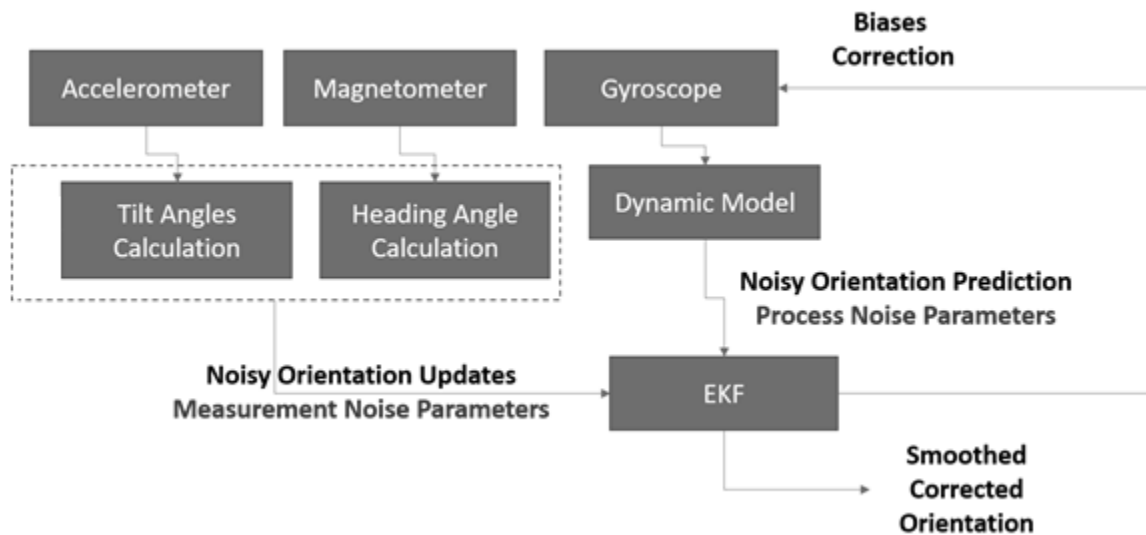


Figure 1-1: Simple block diagram of AHRS

### 1.3 Previous Work

Two common IMU errors have been modeled in several researches [7] [18]; biases and high-frequency noise (also known as random walk). IMU biases are commonly modelled as first order GM random process, which is a stationary Gaussian process with an exponential autocorrelation function [12, 17]. The IMU high-frequency random noise have been extensively

modelled using AV method too, which represents the root means square (RMS) random drift error as a function of averaging time [19, 18]. Various types of errors that are present in the inertial-sensor data can be characterised by performing certain operations over the entire length of the obtained data records [18].

The GM have been successfully used to model bias error behaviour in several practical systems [7] [20] [12]. However, the accuracy obtained is a function of the length of the available data. AV also has been used widely to model noise behaviour of sensors. However, the estimation accuracy of AV for a given time  $T$  depends on the number of independent clusters within the data set thus accuracy is dependent on adequate number of clusters [19]. In essence, the noise parameters resulting from GM and AV may not match those for the real process thus hampering the accuracy of Kalman filter estimation and may lead to divergence. The adaptive and fuzzy-logic EKF have been used in the literature to cope with such scenario [21, 22]. However, adaptive EKF adds more computation and complexity to the system.

#### **1.4 Thesis Objectives**

The ultimate objective of this thesis is to develop a robust and systematic approach to tuning the noise parameters of EKF-based AHRS. Angular random walk noise can be reasonably estimated by AV method. The statistical properties of gyroscope bias errors can be modeled as GM random process as indicated in [7, 23]. GM parameters can be estimated by processing a long stationary record of gyroscope measurements and calculating the autocorrelation function. The GM can only provide an initial nominal design value of gyroscope bias parameters, thus GA is applied to further optimize GM-estimated parameters and measurement noise parameters. Since

there is no exact closed-form solution for these EKF noise parameters optimization, the problem is approached as a nonlinear generic optimization problem [23, 24, 25] and approached by GA.

The GA maps a set of individual objects into a new set of population with the aim of finding an approximately good solution to the system by genetically breeding the set of individuals over a series of iterations. To accelerate the GA performance, we propose the utilization of DoE technique. We use DoE technique to determine the most significant parameters in the AHRS design. Then, we use DoE to direct the GA operators to work on the most significant parameters which accelerates the convergence of the GA.

We will be using the GM-estimated values as nominal design point to set upper and lower bounds on the values of the tuning parameters. A lower-upper bound should be set for measurement noise covariance values as well. To run the GA to estimate EKF parameters, raw IMU data along with ground truth angles were obtained. The fitness function of the GA is based on the error between the EKF output and the ground-truth angles. After GA iterations is performed, the values of noise parameters of the best individuals will be chosen as the best EKF parameters.

## **1.5 Contributions**

The main contributions of this thesis to the field of EKF-based sensor fusion and AHRS are:

- The development of a systematic hybrid tuning approach for EKF parameters tuning using a combination of AV, GM modelling and GA to achieve better attitude and heading estimation accuracy.
- The investigation of the validity and accuracy of the proposed method by testing on both simulation and real data.

- The application of the DoE concept to enhance the performance of the developed GA.
- After testing the proposed method on a low-speed test data, the results are further investigated on a dynamic scenario.
- Out of this thesis work, two conference papers have been published.

## 1.6 Thesis organization

The thesis is organized as follows:

- **Chapter 2** provides explanation of MEMS IMU, the concept of operation and some of the errors associated with them. Then, it briefly explains the two most common methods to characterize IMU errors called as the GM model and AV methods. MEMS based IMU available used in this thesis will be introduced, and some collected data set in a stationary condition will be presented.
- **Chapter 3** provides background information on AHRS and how it is approached within an EKF framework. It briefly reviews basic reference frames, orientation representation forms, AHRS system model that shows how attitude/heading is calculated by integrating gyroscope measurements. Measurement model that shows absolute attitude calculation from accelerometer and absolute heading calculation from magnetometer is also explained. Furthermore, the outputs of the EKF prediction and measurements of the both simulated and real-data are also presented.
- **Chapter 4** is dedicated to the proposed EKF parameters optimization approach. It shows how a nominal design parameters point is calculated using AV and GM, and how the EKF performance is influenced by the nominal design values. Then, the chapter explains the GA

and DoE methods. This chapter concludes by explaining the proposed approach and its application in AHRS design optimization.

- **Chapter 5** presents the experimental results that demonstrates the performance of the proposed approach under different conditions and on different data sets. Simulation results are used to highlight the performance of the method based on its comparison with those obtained from conventional methods. Then, the approach is further verified on real IMU data collected under different scenarios. Detailed analysis and discussions of the results are provided in this chapter.
- **Chapter 6 (Conclusion)** provides a summary of this work, main contributions, and list of publications produced during the thesis work. It concludes with a discussion about future work directions.

## 2 Chapter: MEMS based IMUs

INS-based navigation is used aircrafts, automobile, ships, cellphones and other devices that require navigation information. The INS being self-reliant doesn't need external signals such as signals from satellites or ground stations, to provide navigation information [26, 27, 28, 29]. Instead, the INS use measurements provided by IMU to generate navigation solution (position, velocity, and attitude). An IMU typically contains two sensors: an accelerometer which measures specific force and a gyroscope which measures angular velocity. Operating principle of the IMU is based on Newton's first law of motion which states that an object at rest remains at rest or in uniform motion unless an external force is applied. Thus, if external force acts upon a rigid object on which IMU is attached, acceleration is created which will be detected by accelerometers and by integrating this acceleration twice, the change in the state of the object with respect to the initial conditions can be calculated. The accelerometer measurements are measured in body frame. However, they are required in different navigation frames such as North-East-Down frame. Therefore, the gyroscope measurements are necessary to provide the transformation between different coordinate frames (In Chapter 3, more information regarding different computational frames of references is given).

Recently, MEMS technology has been used to develop very-low cost IMUs that measure surrounding conditions such as temperature and orientation of mechanical components. MEMS integrate sensors, actuators and hardware on a typical silicon substrate through the usage of microfabrication innovation [20]. MEMS devices are of great interest since they offer small, low-cost, and lightweight sensors in comparison to available technologies [26, 30]. MEMS technology has a potential for a lot of applications, such as inertial sensing using gyros and accelerometers, communications using RF-MEMS and the medical field using MEMS pressure sensors to monitor

blood pressure amongst others. These sensors offer excellent characteristics that are favored by many manufactures and consumers, such as, low power consumption, low cost, readily available, smaller packaging and less weight. By contributing such characteristics, MEMS technology has changed the concept of obtaining navigation data [20]. In the next two sub-sections, MEMS based IMUs components such as accelerometers and gyroscopes are going to be presented. IMUs error characteristics and error analysis of the IMUs are presented subsequently, as well.

## 2.1 MEMS IMU components

IMU comprises of a set of inertial sensors usually made up of three mutually orthogonal accelerometers and three gyroscopes aligned with the accelerometer [31, 32, 33]. Figure 2-1 shows the typical components of an IMU. IMU works based on dead reckoning where change in orientation, position or velocity is measured and integrated. The result from integrating the change in orientation, position or velocity is added to the previous state to obtain the current position. The output of MEMS IMU may be of potential difference, current, or pulses and are often converted into specific force and angular rate [2, 34, 35, 36]. These are then integrated over sampling interval  $\tau_i$  as follows:

$$v_{ib}^b(t) = \int_{t-\tau_i}^t f_{ib}^b(t') \quad (2.1)$$

$$\alpha_{ib}^b(t) = \int_{t-\tau_i}^t \omega_{ib}^b(t') dt' \quad (2.2)$$

where  $f_{ib}^b$  is the specific force and  $\omega_{ib}^b$  is the angular rate. It is to be noted that  $\alpha_{ib}^b$  are attitude increments while  $v_{ib}^b$  are velocity increments.

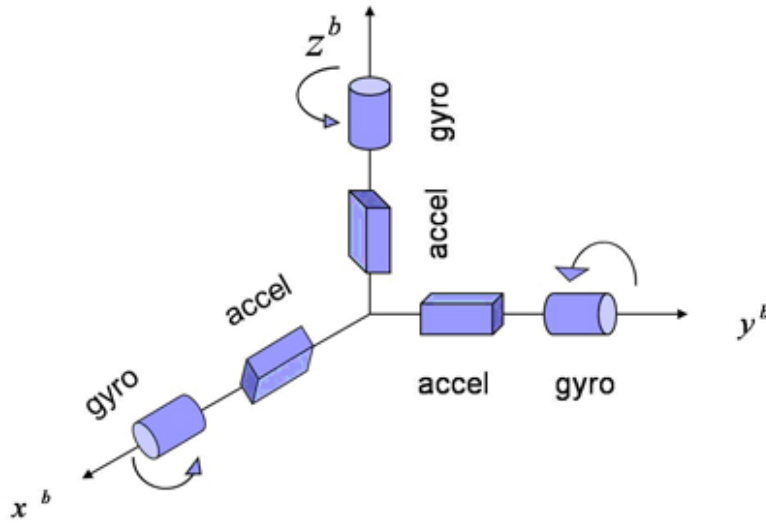


Figure 2-1. Typical IMU Components

### 2.1.1 Accelerometers

An accelerometer is normally made of three main basic components; a proof mass, a suspension and a pickoff which together are used to calculate the acceleration force of a body as the proof mass moves in the appropriate direction depending on the force being applied to the accelerometer. The suspension, a spring in a basic accelerometer, sometimes will try to hold the proof mass against the acceleration force while the pickoff relates the output of the movement of the proof mass to the induced acceleration being applied [20]. The specific force which is the output of an accelerometer is given by:

$$f = a - g \quad (2.3)$$

Where,  $f$  is specific force,  $a$  is acceleration with respect to an inertial frame, and  $g$  is gravitational acceleration. Simple principle of an accelerometer is depicted in Figure 2-2.

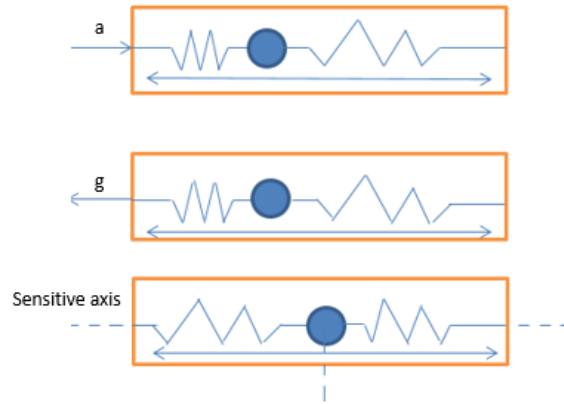


Figure 2-2: Typical accelerometer with proof mass along sensitive axis

### 2.1.2 Gyroscopes

Gyroscopes measure change in angle (angular rates) with respect to an initially known orientation within an inertial frame of reference. Vibrating proof mass are used in almost all micromachined gyros to monitor rotational motion by the principle of energy transfer between two vibration modes of a structure caused by Coriolis force [31]. Coriolis acceleration is proportional to the body velocity, the angle between the direction of motion of the body, and axis of rotation at a given rate of rotation of the observer is given by

$$A_c = -2\omega \times v \quad (2.4)$$

where  $v$  is the body velocity in the rotating frame and  $\omega$  is the angular velocity of the rotating platform. All vibrating gyroscopes implement the Coriolis effect for measuring the change in angles. In accordance with the actuation system wanted, capacitive, piezoresistive, or piezoelectric

methods can be used to sense the differential sinusoidal force created on the tines perpendicular to the main vibrations caused by Coriolis force when the system is rotated [20].

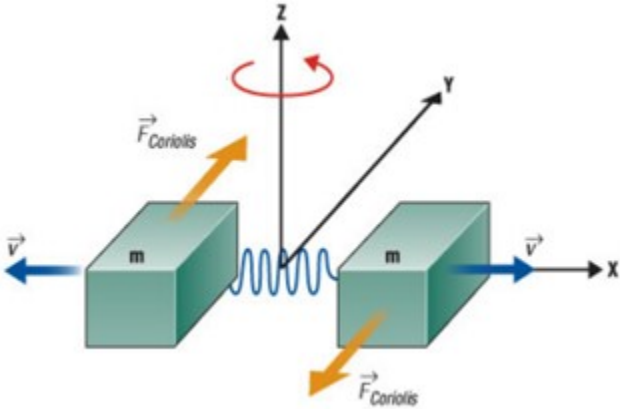


Figure 2-3: Typical Gyroscope Diagram when angular velocity is applied

## 2.2 Examples of MEMS IMUs and Their Applications

Example of a MEMS technology sensor in a restraint system is the inertial sensors used for vehicle rollover detection. The deployment time of the airbags and other devices in a rollover event relies on the sensing algorithm and the sensor data obtained from the gyroscopes and accelerometers. Listed below are some common IMU sensors used in different applications. The IMU used for experimental work in this thesis is the MPU-9250 IMU shown in the second row of Figure 2-4.



ADIS16475 IMU



MPU-9250 IMU



MPU-6000A IMU

**Figure 2-4. Examples of MEMS IMUs**

### **2.3 MEMS IMU Measurements Errors**

Although MEMS sensors have small size and can be of low-cost, they are prone to large errors which build up overtime giving less precise measurements [20]. That is why it is very important to remove these errors. The main error sources that contribute to the output of accelerometer and gyroscope are biases, scale factor, cross-coupling errors, and random noises which are going to be described in the following sub-sections.

#### **2.3.1 Biases**

The bias is characterized by an addition of deterministic error to accelerometer or gyro measurement, this is shown in Figure 2-5. IMU accelerometer and gyro bias can be denoted as  $\mathbf{b}_a = (b_{a,x}, b_{a,y}, b_{a,z})$  and  $\mathbf{b}_g = (b_{g,x}, b_{g,y}, b_{g,z})$  respectively and can be obtained by calibration or fusion algorithms [37, 38]. Given a triad of orthogonal accelerometers and gyroscopes,  $b_{a,x}$  denotes accelerometer bias in x-axis while  $b_{g,x}$  denotes gyro bias in the x-axis.

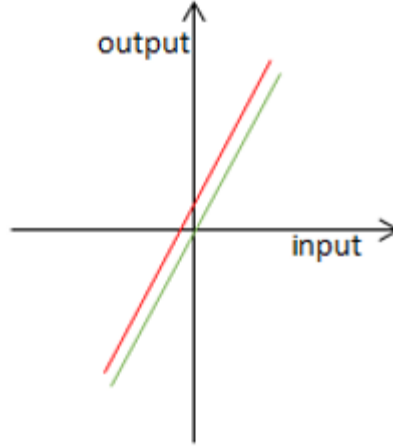


**Figure 2-5. Sensor input versus output with a bias error**

The IMU biases can be split into static,  $b_{as}$  and  $b_{gs}$  and dynamic,  $b_{ad}$  and  $b_{gd}$ , components,

$$b_a = b_{as} + b_{ad} \quad (2.5)$$

$$b_g = b_{gs} + b_{gd} \quad (2.6)$$

Gyroscope biases for MEMS IMUs lie in the range of  $100^\circ/\text{hr}$  and above while these biases are negligible for higher grade IMUs [31].

### 2.3.2 Scale factor

The departure of input-output gradient of a measuring instrument from unity after unit conversion of IMU is known as scale factor error [31, 39, 40]. This is illustrated in

Figure 2-6, the IMU accelerometer and gyro scale factor error are denoted by the vectors  $s_a = (s_{a,x}, s_{a,y}, s_{a,z})$  and  $s_g = (s_{g,x}, s_{g,y}, s_{g,z})$  respectively.

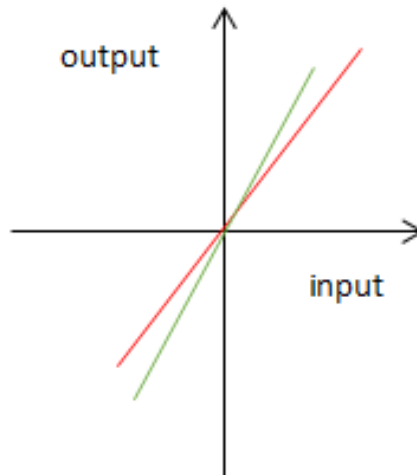


**Figure 2-6: Scale factor error**

### 2.3.3 Misalignment

Misalignment errors in IMU occurs due to the misalignment of the sensitivity axes of the inertial sensors with respect to the orthogonal axes of the body frame as result of manufacturing limitations as shown in Figure 2-7.

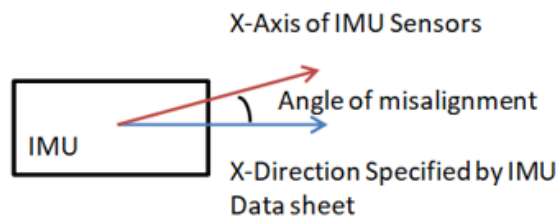


**Figure 2-7: Misalignment of sensor sensitive axes with respect to the body frame**

This type of error makes each accelerometer sensitive to the specific force along the axes orthogonal to its sensitivity axis and each gyro sensitive to the angular rate about the axes orthogonal to its sensitivity axis [41, 42, 43]. The scale factor and cross coupling error for a nominally orthogonal accelerometer and gyro triad can be expressed as

$$M_a = \begin{pmatrix} S_{a,x} & m_{a,xy} & m_{a,xz} \\ m_{a,yx} & S_{a,y} & m_{a,yz} \\ m_{a,zx} & m_{a,zy} & S_{a,z} \end{pmatrix} \quad (2.7)$$

$$M_g = \begin{pmatrix} S_{g,x} & m_{g,xy} & m_{g,xz} \\ m_{g,yx} & S_{g,y} & m_{g,yz} \\ m_{g,zx} & m_{g,zy} & S_{g,z} \end{pmatrix} \quad (2.8)$$

### 2.3.4 Random Noise

Random noises in MEMS IMUs may result from several sources such as mechanical instability, high frequency resonance, and vibration amongst others. The random noise associated with each IMU sample can be denoted as  $w_a = (w_{a,x}, w_{a,y}, w_{a,z})$  and  $w_g = (w_{g,x}, w_{g,y}, w_{g,z})$  for accelerometer and gyro respectively. The inertial sensor random noise is usually presented in terms of root of power spectral density (PSD). The commonly used units are  $\mu g/\sqrt{Hz}$  and  $^\circ/hr/\sqrt{Hz}$  for accelerometer and gyroscope random noise respectively. This units indicate that the random noise is proportional to the square root of the sampling frequency. The higher the sampling frequency the higher the random noise [31]. That is why the error due to accumulation of random noise is measured per square root time. The effect of random noise integration is known as Random Walk. The effect of random walk on angles calculated by a gyroscope can be seen in

Figure 2-8 and Figure 2-9 showing the Azimuth angle resulting from integrating approximately one minute of Z-axis gyroscope of MPU-9250 IMU data at 100Hz [44]. In one minute, we have  $0.3^\circ$  maximum azimuth error which corresponds to an angular random walk (ARW) of  $0.3^\circ/\sqrt{60s} \cong 0.0387^\circ/\sqrt{s}$  [20].

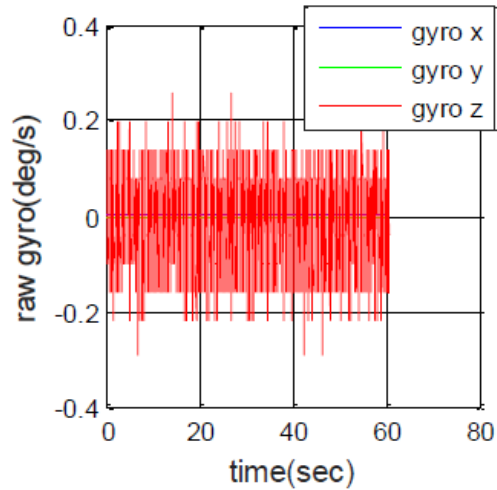


**Figure 2-8. One Minute Record of Stationary Gyro Data measured by MPU-9250 IMU.**

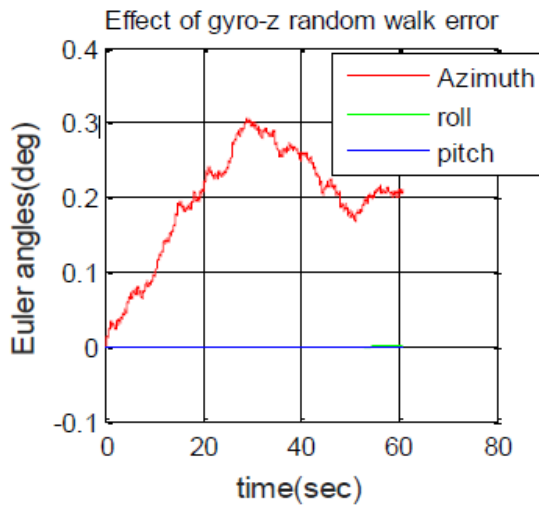


**Figure 2-9. Result of integrating gyro random walk for one minute at 100Hz rate.**

There are other IMU errors that can be examined in the literature. For the scope of this work, this thesis will consider random walk and bias errors only. However, the developed tuning procedure can be applied to any other source or type of errors.

## 2.4 Error Analysis of MEMs IMUs using Allan Variance and Gauss-Markov Methods

IMU errors have been significantly studied in the literature [19, 18, 45, 46]. The most commonly used methods for modeling IMU random errors are GM and AV [47, 48]. Identifying and modeling the random process can be done by these two mentioned common methods. In the coming sub-sections, GM and AV methods will be briefly discussed.

### 2.4.1 Gauss-Markov Random Process

GM is usually used to model random biases. GM process model is incorporated to define a process that exhibits a time correlation between values, which are separated in time. If the estimation period of a process is smaller than the time constant of the GM process, the process can be modeled by the random walk (RW) process. The GM process is a stationary Gaussian process with an exponential autocorrelation function [20]. It is very important model as it fits many real-world problems, and has relatively simple mathematical description given by:

$$\dot{x}(t) = -\beta x(t) + \sqrt{2\beta\sigma^2}w_u(t) \quad (2.9)$$

where  $\beta$  is the reciprocal of the time constant ( $1/\tau$ ),  $w_u$  is unity-variance zero-mean Gaussian noise, and  $\sigma$  is the standard deviation. The general shape of the autocorrelation function of GM process is shown in Figure 2 10. The autocorrelation function of GM process is given by:

$$R_x(\tau) = \sigma^2 e^{-\beta|\tau|} \quad (2.10)$$

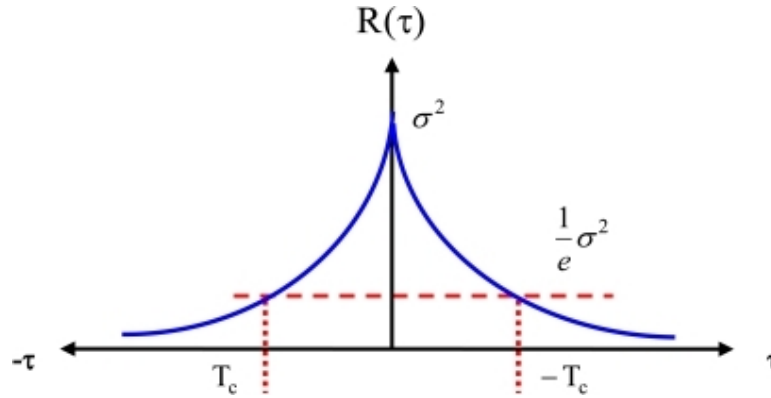


**Figure 2-10: Autocorrelation of 1<sup>st</sup> Order Gauss Markov Process**

Commonly, GM process are used to model the behavior of IMU biases and scale factors. Another most widely recognized modeling strategy to decide the characteristic for the inertial sensor noise for low cost MEMS IMUs is the AV which is described in the following sub-section.

#### **2.4.2 Allan Variance Methodology**

The Allan variance is a method by which the root means square (RMS) random drift error is represented as a function of averaging time [19, 18]. The technique can be used to characterize various types of error terms in the inertial-sensor data by performing certain operations on the entire length of data [18]. The Allan method assumes that one or more white noise sources of strength  $N_i^2$  drives the canonical function resulting in the same statistical and spectral properties as the actual device. Assuming that there are  $N$  sample points with sample time  $t_0$ , form  $n$  consecutive groups of data such that  $n < N/2$ , this is called a cluster. The time associated with the cluster is  $T = nt_0$ . Given the instantaneous output rate of an inertial sensor  $\Omega(t)$ , the cluster average is defined as

$$\bar{\Omega}_k(T) = \frac{1}{T} \int_{t_k}^{t_k+T} \Omega(t) dt \quad (2.11)$$

The average of the next cluster is given as:

$$\bar{\Omega}_{next}(T) = \frac{1}{T} \int_{t_{k+1}}^{t_{k+1}+T} \Omega(t) dt \quad (2.12)$$

where  $t_{k+1} = t_k + T$ .

The difference between two adjacent clusters can be obtained as:

$$\xi_{k+1,k} = \bar{\Omega}_{next}(T) - \bar{\Omega}_k(T) \quad (2.13)$$

For a chosen cluster time  $T$ , the ensemble of  $\xi'$ s forms a set of random variables. The variance of  $\xi'$ s over all the cluster is of the same size obtained from the entire data and it is the quantity of interest. Therefore the Allan variance of length  $T$  is defined as [2, 20]:

$$\sigma^2(T) = \frac{1}{2(N-2n)} \sum_{k=1}^{N-2n} [\bar{\Omega}_{next}(T) - \bar{\Omega}_k(T)]^2 \quad (2.14)$$

After processing a long stationary record of data, AV curve is plotted. The AV curve is unique for inertial sensors and can be used to estimate several noise parameters such as random walk standard deviation. Figure 2-11 shows a typical AV curve for gyroscope measurements [18].

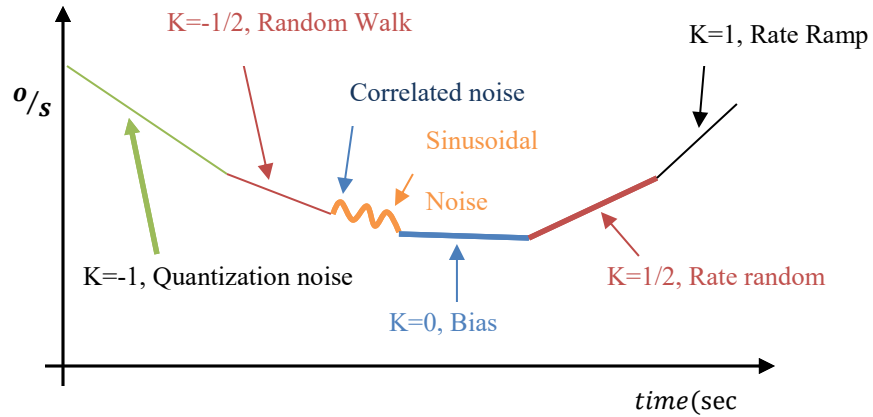


**Figure 2-11: Allan curve for gyroscope.**

The inertial sensor errors such as quantization noise, random walk, correlated noise, sinusoidal noise, bias instability can be obtained directly from AV curve. Commonly the AV curve is plotted on a log-log curve for better visibility. As can be seen from Figure 2-11, different errors corresponding to different slope (k) values can be estimated.

## 2.5 Analysis of the MPU-9250 MEMS IMU used in This Research

In this thesis, we used a reprogrammable SparkFun 9DoF Razor IMU-M0 sensor which combines a SAMD21 microprocessor with an MPU-9250 9DoF (nine degrees of freedom) sensor featuring three-axis sensors i.e. accelerometer, gyroscope, and aided by a magnetometer and thus able to sense linear acceleration, angular rate, and magnetic field. The reason for the incorporation of the magnetometer in the IMU is to improve accuracy of the heading. A common way to integrate accelerometer, gyroscope, and magnetometer outputs is through the AHRS using an EKF, which is described in detail in Chapter 3. The sensor and the sensing axes are shown in Figure 2-12.

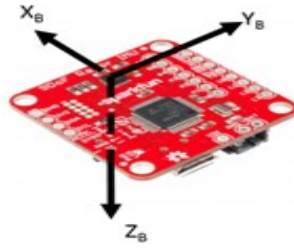


**Figure 2-12: SparkFun 9DoF Razor IMU M0 and the sensing axes**

To generate the GM autocorrelation plot and AV curve for our IMU, stationary data is collected at fixed frequency, at room temperature, for seven hours from fixed position IMU. Samples of these data collected are plotted in

Figure 2-13 and Figure 2-14. And then, the IMU was used in testing scenarios which served as a real data sets for the experimental work in this thesis.

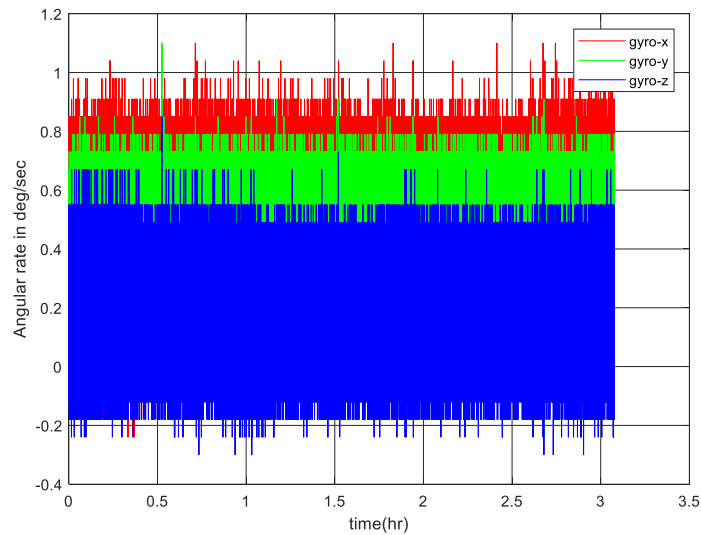


**Figure 2-13: Sample stationary data collected by gyro**

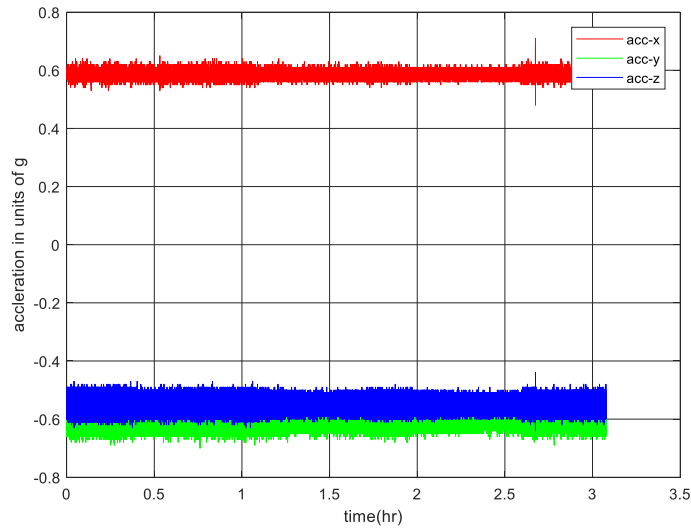


**Figure 2-14: Sample stationary data collected by accelerometer**

### 2.5.1 Error Analysis of MPU-9250 MEMS IMU using GM and AV

The autocorrelation sequence of the recorded stationary data set has been calculated and displayed. Figure 2-15 and Figure 2-16 shows the autocorrelation sequence of gyroscope and accelerometer measurements respectively. From Figure 2-15, the Gauss-Markov parameters (time constant  $\tau_\omega$  and standard deviation  $\delta_\omega$ ) of the gyroscope and accelerometer errors can be estimated. Since in this thesis we will focus on gyroscope errors, the values of the time constant and standard deviations of the gyroscope axes are shown in Table 2-1.

The AV curves for the gyroscope measurements are shown in Figure 2-17, Figure 2-18, and Figure 2-19. In all plots, the value at slope -0.5 (which correspond to the random walk noise) is shown. Taking the intersection of the AV curve with a line having -0.5 slope (at the time value of 1s), angular random walk can be estimated. As shown in the figure below, the approximate

value for gyroscopes ARW is  $0.007 \text{ }^\circ/\text{s}/\sqrt{\text{s}}$ . As the units of the ARW shows, the random walk value is proportionally increases with sampling rate. All values are shown in

Table 2-2 .

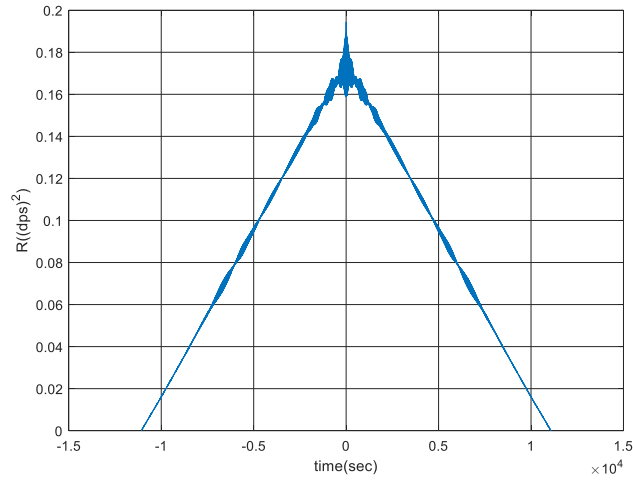


**Figure 2-15: GM Autocorrelation Sequence of Gyro**

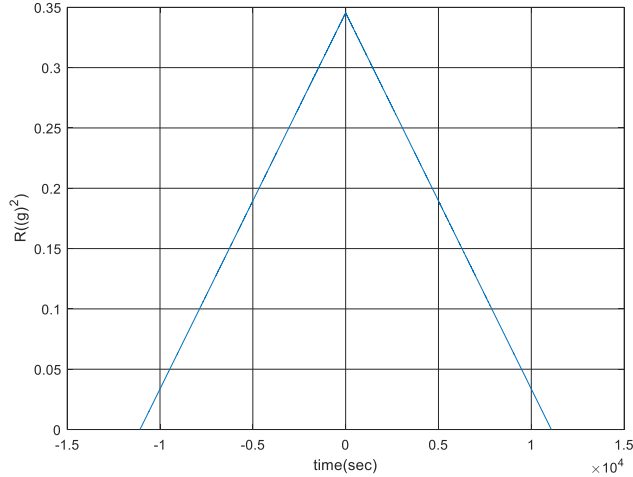


**Figure 2-16: GM Autocorrelation Sequence of Accelerometer**

**Table 2-1: GM estimated time constant and standard deviation**

$\tau_{\omega x}(\text{h})$	$\tau_{\omega y}(\text{h})$	$\tau_{\omega z}(\text{h})$	$\delta_{\omega x}(\text{ }^\circ/\text{s})$	$\delta_{\omega y}(\text{ }^\circ/\text{s})$	$\delta_{\omega z}(\text{ }^\circ/\text{s})$
1.62	1.83	1.83	0.46	0.44 ( $^\circ/\text{s}$ )	0.44 ( $^\circ/\text{s}$ )

**Table 2-2: Random Walk Values as estimated by AV test**

$rw_{\omega x} (^{\circ}/s/\sqrt{s})$	$rw_{\omega y} (^{\circ}/s/\sqrt{s})$	$rw_{\omega z} (^{\circ}/s/\sqrt{s})$
0.007611	0.007323	0.00777

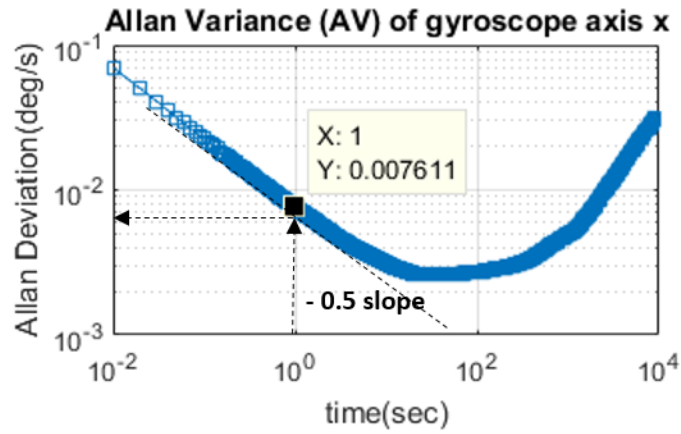


**Figure 2-17: Allan Variance results for x-axis of the MPU9250 IMU gyroscope**

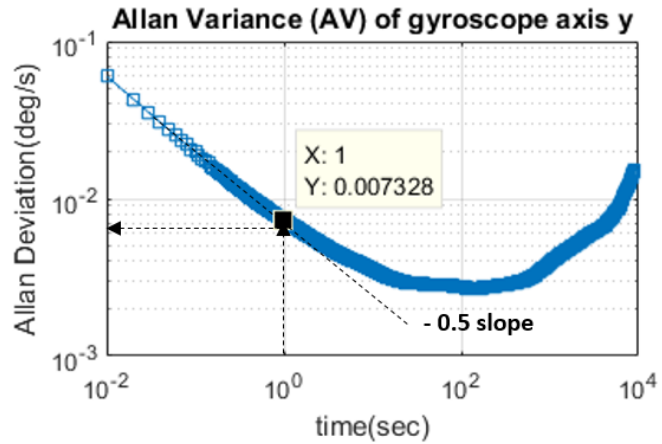


**Figure 2-18: Allan Variance results for y-axis of the MPU9250 IMU gyroscope**

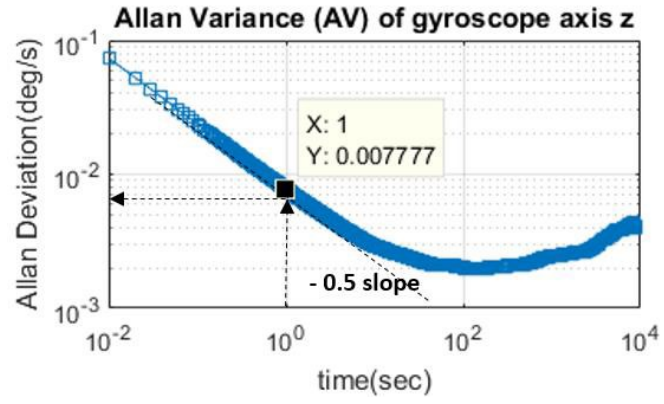


Figure 2-19: Allan Variance results for z-axis of the MPU9250 IMU gyroscope

## **3 Chapter: AHRS using MEMS IMU**

### **3.1 Reference Frames**

Coordinate frames are used to represent objects state including position, velocity, and orientation. It comprises of origin and axis of either an object or a point of reference. The object frame is used to represent a body whose position and orientation are to be calculated while the reference frame is used to describe a known space such as the earth, to which the position and orientation of the object is to be referenced. The main coordinate frames used in this thesis are Earth-Centered Inertial Frame (ECI), Earth-Centered Earth-Fixed Frame (ECEF), Local Navigation Frame (L), and Local Tangent-Plane Frame [31]. In the following sub-sections, we will briefly explain these reference frames.

#### **3.1.1 Earth-Centered Inertial Frame**

Inertial frame is a coordinate frame which does not accelerate or rotate with respect to the rest of the Universe. The Earth-Centered Inertial Frame is nominally centered at the earth's center of mass with the z-axis pointing along the earth's axis of rotation to the North Pole. The x- and y-axis are attached to the equatorial plane and do not rotate with earth, the y-axis is  $90^0$  ahead of the x-axis in the direction of the earth's rotation.

#### **3.1.2 Earth-Centered Earth-Fixed Frame**

The Earth-Centered Earth-Fixed Frame is like the Earth-Centered Inertial Frame but differs in the sense that the axis is fixed to and rotate with the earth. The x-axis points from the origin of the frame to a point where the equator and the Conventional Zero Meridian (CZM) intersects, the longitude of the CZM defines  $0^0$  longitude. The y-axis points from the origin of the frame to a

point where the equator and the  $90^0$  east meridian intersects. The z-axis is Earth-Centered Earth-Fixed Frame is coincident with that of the Earth-Centered Inertial Frame.

### **3.1.3 Local Navigation Frame**

The origin of the Local Navigation Frame is the position of the object for which the navigation solution is sorted. Its axes are aligned with topographic directions; North, East and Vertical. There are several conventions used namely, north east down (NED), east north up (ENU), north west up (NWU), south west down (SWD), all representing x, y and z respectively. In the NED convention, the z-axis or Down axis is the normal to the surface of the earth ellipsoid pointing towards the center of the earth, x-axis or North axis is orthogonal to the z-axis and points towards the north pole, and the y-axis or East axis points towards the east completing the orthogonal set. The north and east axes are undefined at the poles, resulting in singularity, hence navigation solution using this convention will not be suitable for applications near the poles.

### **3.1.4 Local Tangent-Plane Frame**

The origin of a Local Tangent-Plane Frame is fixed to the earth's surface, similar to the Local Navigation Frame, the z-axis is aligned to the vertical which may be up or down, the x- and y-axis may be aligned to environmental features such as road or building or topographic directions. In the latter case it is known as a local geodetic frame or topocentric frame. Figure 3-1 illustrates the relationship between the described frames. In this thesis, the orientation of the object will be described as a rotation relationship between the object frame (body frame  $B$ ) and the Local Navigation Frame ( $L$ ). But because IMU measurements are mainly with respect to the ECI frame and object motion is with respect to ECEF, all these frames are usually used in the orientation estimation equations.

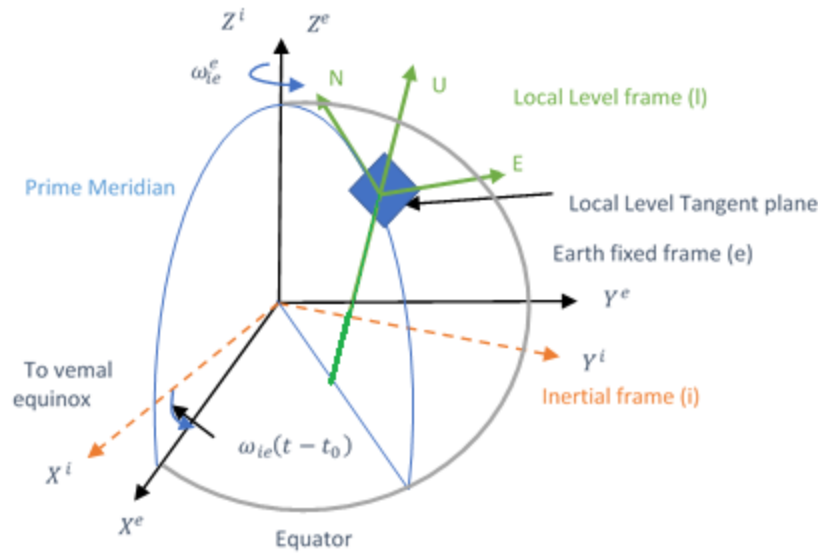


Figure 3-1: The local-level ENU reference frame in relation to the ECI and ECEF frames

## 3.2 Orientation Representation and Coordinate Transformation

This thesis focuses on the orientation estimation of objects. Orientation can be described as rotational transformation between object body frame (B) and a reference frame. This rotational transformation can be described in several forms as discussed in the following sub-sections.

### 3.2.1 Euler Angles

The Euler angles are an intuitive way of describing the orientation of one coordinate frame with respect to another [7, 31]. Three successive rotations are required with each rotation carried out about its predecessor and/or successor. The orientation of an object frame with respect to a reference frame can easily be represented using Euler angles to describe the rotation of a reference frame to coincide with the object frame. Given an object frame  $B$  and a reference frame  $L$ , the Euler angles describing the orientation of the object frame with respect to the reference frame are the roll  $r_{LB}$ , pitch  $p_{LB}$ , and heading (or azimuth)  $A_{LB}$ . The roll angle is the axis pointed out the nose and rotating the object about the x-axis. The pitch angle is the axis pointing out to the right and represents the inclination or declination while the azimuth angle is the axis pointing out the bottom

used in the calculation of the heading of the object. The Euler angles  $(r_{LB} + \pi, p_{LB} - \pi, A_{LB} + \pi)$  and  $(r_{LB}, p_{LB}, A_{LB})$  gives the same result and can be avoided by limiting the pitch rotation to the range  $(-90^0 \leq p_{LB} \leq 90^0)$ . Another difficulty with Euler angles is the singularity that occurs at  $\mp 90^0$  pitch angle which makes the roll and yaw inseparable.

### 3.2.2 Quaternions

One disadvantage of Euler angles is gimbal lock, gimbal lock occurs when two axes are aligned, such as when the pitch and the yaw axes are aligned, and with the rotation of the roll gimbal, the pitch and the yaw angle are both affected the same, therefore losing orientation [2]. One method to avoid gimbal lock that can be utilized is quaternions. The use of quaternions is like adding another gimbal or axis but only theoretically. Utilizing this method eliminates the need for adding more parts hence less weight to the device. This method is used to keep the efficiency up and represent attitude of given object or sensors. A quaternion is a similar idea to complex numbering, except that rather than one imaginary axis, there are three imaginary axes. To get 3D interpretation, four components must be present; one real component and three imaginaries represented as a vector. Quaternion operation is performed by scaling the vector with the real part, one of the imaginary components is used for the rotation axis and the other two components used for the orientation of the platform. The quaternions vector  $q = [a \ b \ c \ d]$  must satisfy the constraints:

$$a^2 + b^2 + c^2 + d^2 = 1 \tag{3.1}$$

### 3.2.3 Direction Cosine Matrix (DCM)

Orientation can also be described by direction cosine matrix (DCM) [7] [31]. DCM is a 3x3 matrix that contains the cosines of the nine possible pairs of axes of two different Cartesian

coordinate systems typically used to translate from the body frame into the reference frame (i.e.  $L$  frame). Ref [7, 31] provided information on how to use the DCM method integrated with IMUs. All forms of orientation representation discussed above to represent orientation can be obtained from each other. Euler angles can be converted to coordinate transformation matrix (e.g. DCM) by representing each rotation as a matrix and then multiplying the individual rotation matrices. Attitude can be represented as reference frame to object transformation  $C_L^B$  or object frame to reference transformation  $C_B^L$ . The reference frame to object coordinate matrix following the azimuth, pitch, roll rotations sequence is given by:

$$C_L^B = \begin{bmatrix} 1 & 0 & 0 \\ 0 & \cos r_{LB} & \sin r_{LB} \\ 0 & -\sin r_{LB} & \cos r_{LB} \end{bmatrix} \begin{bmatrix} \cos p_{LB} & 0 & -\sin p_{LB} \\ 0 & 1 & 0 \\ \sin p_{LB} & 0 & \cos p_{LB} \end{bmatrix} \begin{bmatrix} \cos A_{LB} & \sin A_{LB} & 0 \\ -\sin A_{LB} & \cos A_{LB} & 0 \\ 0 & 0 & 1 \end{bmatrix} \quad (3.2)$$

$$\begin{bmatrix} \cos r_{LB} \cos A_{LB} & \cos r_{LB} \sin A_{LB} & -\sin r_{LB} \\ \begin{pmatrix} -\cos r_{LB} \sin A_{LB} \\ +\sin r_{LB} \sin p_{LB} \cos A_{LB} \end{pmatrix} & \begin{pmatrix} \cos r_{LB} \cos A_{LB} \\ +\sin r_{LB} \sin p_{LB} \sin A_{LB} \end{pmatrix} & \sin r_{LB} \cos p_{LB} \\ \begin{pmatrix} \sin r_{LB} \sin A_{LB} \\ +\cos r_{LB} \sin p_{LB} \cos A_{LB} \end{pmatrix} & \begin{pmatrix} -\sin r_{LB} \sin A_{LB} \\ +\cos r_{LB} \sin p_{LB} \sin A_{LB} \end{pmatrix} & \cos r_{LB} \cos p_{LB} \end{bmatrix}$$

The Euler angles can be found from the coordinate transformation matrix as follows

$$r_{LB} = \arctan2(C_{L,2,3}^B, C_{L,3,3}^B) \quad (3.3)$$

$$p_{LB} = -\arctan2(C_{L,1,3}^B) \quad (3.4)$$

$$A_{LB} = \arctan2(C_{L,1,2}^B, C_{L,1,1}^B) \quad (3.5)$$

When the coordinate matrix represent object to reference frame transformation, it is given as

$$C_B^L = \begin{bmatrix} \cos r_{LB} \cos A_{LB} & \begin{pmatrix} -\cos r_{LB} \sin a_{LB} \\ +\sin r_{LB} \sin p_{LB} \cos a_{LB} \end{pmatrix} & \begin{pmatrix} \sin r_{LB} \sin A_{LB} \\ +\cos r_{LB} \sin p_{LB} \cos A_{LB} \end{pmatrix} \\ \cos r_{LB} \sin a_{LB} & \begin{pmatrix} \cos r_{LB} \cos a_{LB} \\ +\sin r_{LB} \sin p_{LB} \sin a_{LB} \end{pmatrix} & \begin{pmatrix} -\sin r_{LB} \sin A_{LB} \\ +\cos r_{LB} \sin p_{LB} \sin A_{LB} \end{pmatrix} \\ -\sin r_{LB} & \sin r_{LB} \cos p_{LB} & \cos r_{LB} \cos p_{LB} \end{bmatrix} \quad (3.6)$$

The corresponding Euler angles can be calculated as:

$$r_{LB} = \arctan_2(C_{B,3,2}^L, C_{B,3,3}^L) \quad (3.7)$$

$$p_{LB} = -\arctan_2(C_{B,3,1}^L) \quad (3.8)$$

$$A_{LB} = \arctan_2(C_{B,2,1}^L, C_{B,1,1}^L) \quad (3.9)$$

In this thesis, we will describe attitude and heading by a transformation from object (body) frame,  $B$ , to local navigation frame,  $L$ . A 3D position vector in the body fixed frame can be transformed to 3D positions in the  $L$  frame as follows,

$$\begin{bmatrix} x^L \\ y^L \\ z^L \end{bmatrix} = C_B^L \begin{bmatrix} x^B \\ y^B \\ z^B \end{bmatrix} \quad (3.10)$$

The coordinate transformation matrix from  $B$  frame to  $L$  frame can be expressed as a function of quaternion vector as follows [25]

$$C_B^L(1,1) = (a^2 + b^2 - c^2 - d^2) \quad (3.11)$$

$$C_B^L(1,2) = 2(bc - ad) \quad (3.12)$$

$$C_B^L(1,3) = 2(bd + ac) \quad (3.13)$$

$$C_B^L(2,1) = 2(bc + ad) \quad (3.14)$$

$$C_B^L(2,2) = (a^2 - b^2 + c^2 - d^2) \quad (3.15)$$

$$C_B^L(2,3) = 2(cd - ab) \quad (3.16)$$

$$C_B^L(3,1) = 2(bd - ac) \quad (3.17)$$

$$C_B^L(3,2) = 2(cd + ab) \quad (3.18)$$

$$C_B^L(3,3) = (a^2 - b^2 - c^2 + d^2) \quad (3.19)$$

the Euler angles can be extracted directly from quaternion vector as follows:

$$\begin{cases} r = \arctan \frac{2(cd - ab)}{a^2 + b^2 + c^2 + d^2} \\ p = \arcsin(2(ac - bd)) \\ A = \arctan \frac{2(bc + ad)}{a^2 + b^2 + c^2 + d^2} \end{cases} \quad (3.20)$$

### 3.3 AHRS System Model

AHRS system model is the equation that processes raw IMU measurements and provides orientation information. This orientation information can be represented in any of the formats discussed above. Quaternion form is preferred in the system equations as it does not suffer from singularity. In the following sub-section, we will describe the AHRS system model.

#### 3.3.1 Quaternion derivative equation

The quaternion derivative equation is given by [49]:

$$\dot{q} = \frac{1}{2} \Omega(\omega)q \quad (3.21)$$

where  $\Omega(\omega)$  is the gyroscope measurements matrix given by:

$$\Omega(\omega) = \begin{bmatrix} 0 & -\omega_x & -\omega_y & -\omega_z \\ \omega_x & 0 & \omega_z & -\omega_y \\ \omega_y & -\omega_z & 0 & \omega_x \\ \omega_z & \omega_y & -\omega_x & 0 \end{bmatrix} \quad (3.22)$$

where  $\omega = [\omega_x \ \omega_y \ \omega_z]$  represents the angular rate of the body frame represented in the body frame with respect to the ECI frame which is measured by a gyroscope. Using the notations of  $B$  and  $L$  frames, orientation system model can be given by:

$$\dot{q}_B^L = \frac{1}{2} \Omega(W_{LB}^B) [a \ b \ c \ d]^T \quad (3.23)$$

where

$$\Omega(W_{LB}^B) = \begin{bmatrix} 0 & -\omega_{LBx}^B & -\omega_{LBy}^B & -\omega_{LBz}^B \\ \omega_{LBx}^B & 0 & \omega_{LBz}^B & -\omega_{LBy}^B \\ \omega_{LBy}^B & -\omega_{LBx}^B & 0 & \omega_{LBx}^B \\ \omega_{LBz}^B & \omega_{LBy}^B & -\omega_{LBx}^B & 0 \end{bmatrix} \quad (3.24)$$

### 3.3.2 Gyroscope Measurement Model

The measured angular rate given by the gyroscope are contaminated by errors as described earlier. In this thesis, we consider biases and random walk errors as seen in Figure 3-2. Therefore, the gyroscope measurement model is given by [19, 18]:

$$\omega_m^b = \omega^b + b_g + w \quad (3.25)$$

where  $\omega_m^b$  is the measured angular rate,  $\omega^b = [\omega_x^b \ \omega_y^b \ \omega_z^b]^T$  is the true angular rate,  $b_g$  is a variable gyro bias, and  $w$  is a high frequency zero-mean Gaussian random noise.

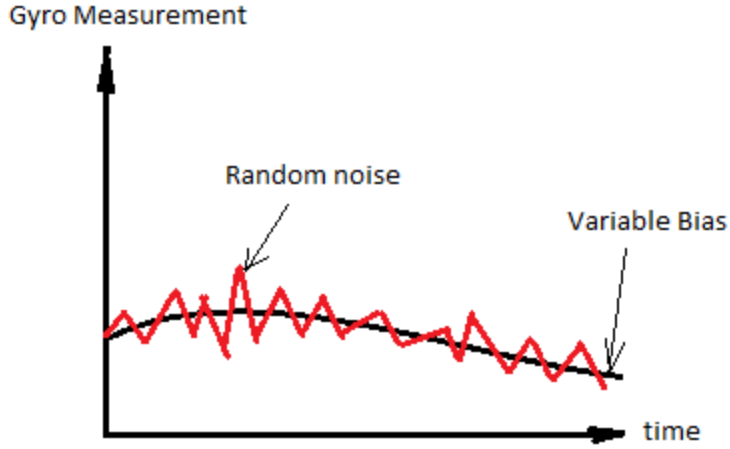


Figure 3-2. Bias and Random noise error

### 3.3.3 Compensation for Earth Rate, and Motion Dynamics

Because the gyroscope measures all rotations with respect to the global ECI frame, not only the pure body rotation, the gyroscope measurements need to be compensated for biases, Earth rotation and angular rate due to motion on ellipsoid surface of Earth (transport rate). Thus, gyroscope measurement vector  $[\omega_{LBx}^B \ \omega_{LBy}^B \ \omega_{LBz}^B]$  can be modeled as follows

$$\omega_{LB}^B = \omega_{IB}^B - b_g - C_L^B \omega_{IL}^I + w \quad (3.26)$$

Where  $\omega_{IB}^B$  is the measured gyroscope value,  $\omega_{IL}^I$  is the Earth + Transportation rates (superscript  $I$  refers to ECI frame) given by:

$$\omega_{IL}^I = \omega_{IE}^I + \omega_{EL}^I \quad (3.27)$$

$$\omega_{IE}^I = [w^e \cos(\varphi) \ 0 \ -w^e \sin(\varphi)] \quad (3.28)$$

where  $w^e$  is Earth rotation and  $\varphi, \lambda$  are latitude and longitude coordinates of the platform.

$$\omega_{EL}^I = \left[ \frac{v_e}{(R_n+h)} \quad \frac{-v_n}{(R_m+h)} \quad \frac{v_e}{(R_n+h)} \tan(\varphi) \right] \quad (3.29)$$

where  $h$  is the height of the vehicle,  $R_n$  and  $R_m$  are the normal and meridian radii of curvature of Earth ellipsoid at current latitude and velocity in  $L$  frame is  $v^L = [v_n \ v_e \ v_d]$ . In stationary or low-dynamics scenarios,  $v^L$  is set to zero. In dynamic scenarios at which the platform is moving at relatively high dynamics, velocity and position need to be calculated.

### 3.3.4 Velocity and Position System Model in Dynamic Scenarios

In dynamic scenarios, velocity is estimated by simply projecting the accelerometer measurements  $a_{SF}^B = [f_x \ f_y \ f_z]^T$  from body  $B$  frame to local level navigation frame  $L$  and integrate the results once after compensating for gravity force. However, because  $L$  is a rotating frame,  $a_{SF}^B$  must be compensated also for Coriolis Effect [7] [31]. Coriolis Effect is the acceleration the accelerometer will measure due to the rotation of  $L$  frame. Therefore, the velocity equation is calculated as follows:

$$v^L = C_L^B a_{SF}^B + g^L - (\omega_{EL}^L + 2\omega_{IE}^L) x v^L \quad (3.30)$$

Where  $g^L$  is the gravity vector in  $L$  frame,  $\omega_{EL}^L$  is rotation of  $L$  frame with respect to Earth (ECEF frame) due to body motion and  $\omega_{IE}^L$  is rotation of Earth with respect to the inertial (ECI frame).

Geodetic position (latitude, longitude, and height) can be then calculated by:

$$\dot{\varphi} = \frac{v_n}{(R_m + h)} \quad (3.31)$$

$$\dot{\lambda} = \frac{v_e}{(R_n + h)\cos(\varphi)} \quad (3.32)$$

$$\dot{h} = -v_d \quad (3.33)$$

where  $R_n$  and  $R_m$  are the normal and meridian radius of curvature of Earth at the current latitude ( $\varphi$ ), longitude ( $\lambda$ ), and altitude  $h$ .

### 3.3.5 Results of AHRS System Model on raw IMU Data

In this sub-section, we show the performance of the AHRS system model when it is applied to process noisy raw gyroscope data. In this test, we used simulated raw IMU data generated by applying inverse kinematics to ground-truth angles shown in Figure 3-3. The raw IMU gyroscope data has been generated and then a bias vector or  $[0.4 \ 0.4 \ 0.4]^T$  °/s has been added to gyroscope x, y and z axes respectively. In addition, a zero-mean Gaussian random noise with standard deviation 0.05 °/s has been added as well. As the AHRS system model integrates gyroscope measurements, orientation errors (drifts) will grow over-time as seen in Figure 3-4, Figure 3-5 and Figure 3-6. Due to these drifts, fusing the AHRS system model output with absolute source of orientation updates is required which is the topic of the coming sub-section.

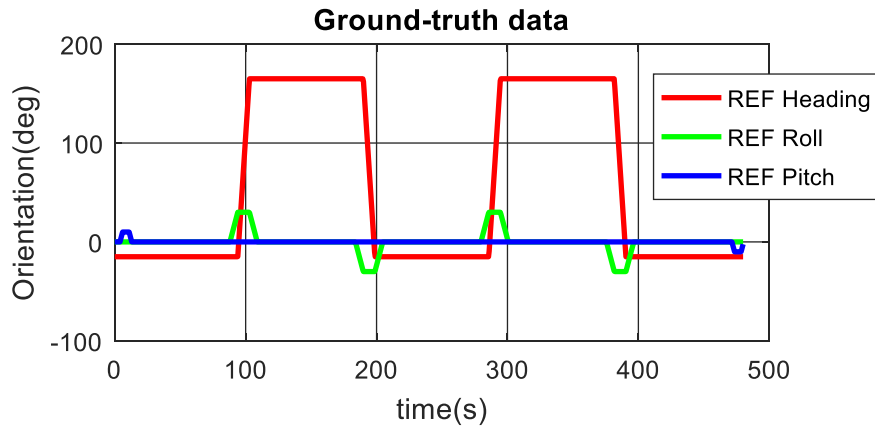
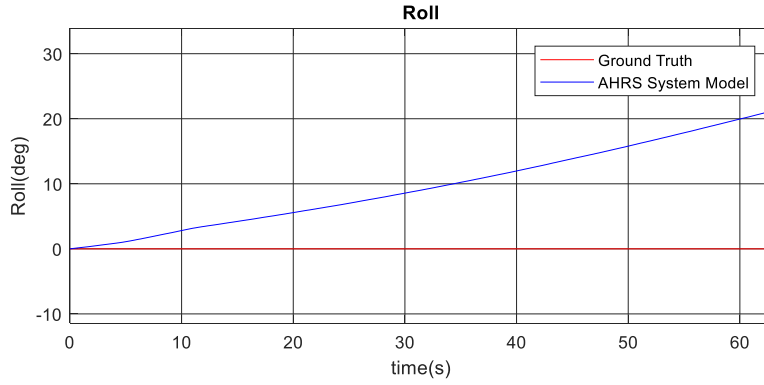
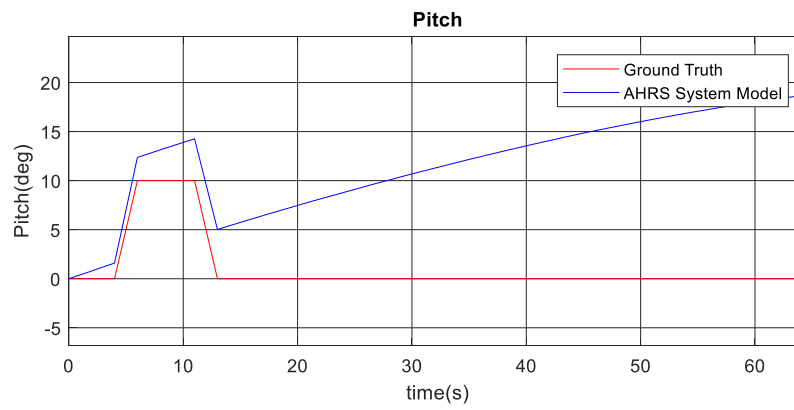


Figure 3-3: Ground-truth Simulated Angles



**Figure 3-4: Roll angle drifts of AHRS System Model in 60 seconds**



**Figure 3-5: Pitch angle drifts of AHRS System Model in 60 seconds**

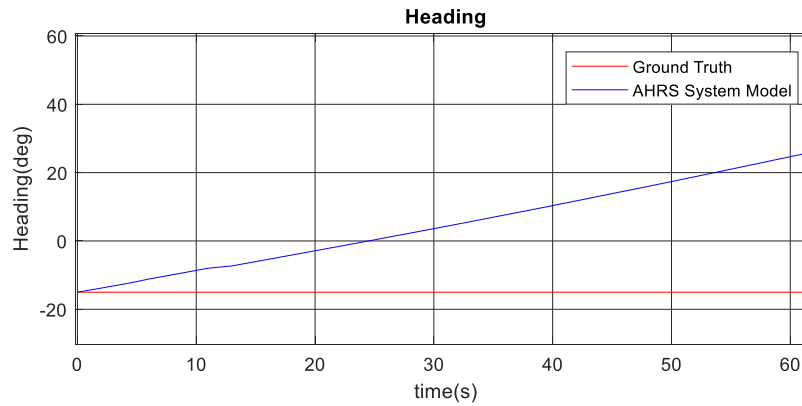


**Figure 3-6: Heading angle drifts of AHRS System Model in 60 seconds**

### 3.4 Absolute Tilt calculation from accelerometer

Tilt angles include pitch and roll. To perform a tilt measurement, use of measurements

from a tri-axial MEMS accelerometer and arctangent function is the most advantageous solution [20]. Tilt is most commonly expressed by determining its two component angles pitch and roll [50] against the components of the gravitational acceleration [51, 52, 53, 54]. Under low translational motion, accelerometers measurements ( $a_{SF}^B$ ) senses gravity  $g^L$  projected on body frame as follows:

$$a_{SF}^B = C_L^B g^L \quad (3.34)$$

Tilt angles can be calculated from accelerometer measurements as follows:

$$r_m = atan2(-a_{SFY}^B, -a_{SFZ}^B) \quad (3.35)$$

$$p_m = atan2\left(a_{SFX}^B, \sqrt{a_{SFY}^B{}^2 + a_{SFZ}^B{}^2}\right) \quad (3.36)$$

As the accelerometers include noise and errors, the tilt angles calculated by gravity measurements are noisy as can be seen from Figure 3-7 and Figure 3-8. Figure 3-7 and Figure 3-8 show the roll/pitch angles calculated by processing simulated accelerometer data. In this test the accelerometer data was contaminated by a random Gaussian noise of  $8 \text{ mg}$ .

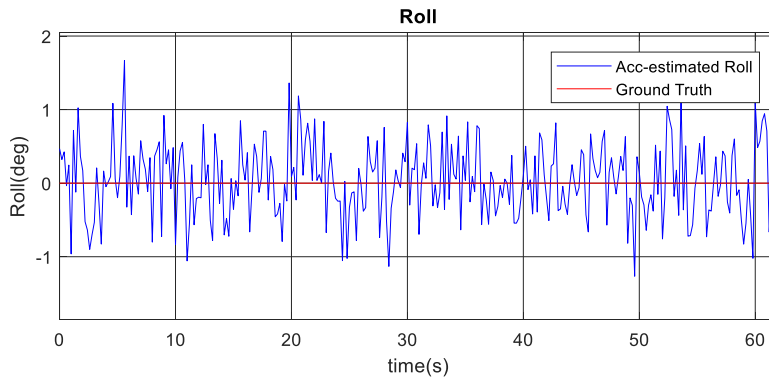


**Figure 3-7: Absolute Roll calculated from noisy Accelerometer data**

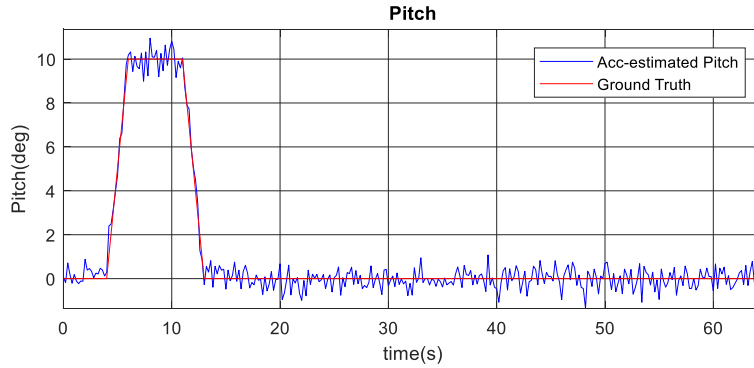


**Figure 3-8: Absolute Pitch calculated from noisy Accelerometer data**

Despite the noisy results, the advantage of tilt angles calculated by gravity is that it does not drift over time. Therefore, fusion with the output of the AHRS system model is ideal solution. To obtain full absolute 3D orientation, the only remaining angle that needs source of update is heading. Heading angle can be calculated by Magnetometer as will be discussed in the next subsection.

### 3.5 Absolute Heading Calculation from Magnetometer

A magnetometer [7] [31] [55] is used to obtain the heading direction of an object, by referencing the strength and direction of the earth's magnetic field. The magnetometer sensing element sensitivity tends to deteriorate due to the changing environment it operates in and produce errors which wouldn't be useful for the purpose it is needed for. The environmental conditions MEMS are usually exposed to are banking angle and elevation changes. One method used to remove errors due to these changes is coupling the magnetometer with an accelerometer to calculate a heading angle. Removing the banking, pitching and rolling effect on the sensors would be ideal [44]. Like accelerometer and gyroscopes, magnetometers suffer from errors too.

Two main categories of magnetic distortions can be classified as hard iron and soft iron. Hard iron relates to the constant disturbance in the magnetic field around the sensors caused by the surrounding structure having ferrous materials which tends to create its own magnetic field by its electronic components on board and then adds to the sensor's magnetic field. The disturbance caused this way is relatively constant and an offset or bias can be done to eliminate the hard iron distortions. Soft iron on the other hand, is normally the result of the material used to distort the magnetic field within the sensor itself and orientation with respect to the earth magnetic field. Due to these errors, magnetometer calibration and error compensation should be conducted before the application. However, this topic is out of the scope of this thesis. In this thesis, we have used a well-calibrated magnetometer as a source of absolute heading updates. If tilt angles are available, the heading angle can then be calculated from magnetometer as follows:

$$A_m = \text{atan2}(-m_y \cos(r) + m_z \sin(r) m_x \cos(p) + m_y \sin(r) \sin(p) + m_z \cos(r) \sin(p)) + D(l, L) \quad (3.37)$$

where  $m_x$ ,  $m_y$  and  $m_z$  are magnetometer measurements in the three axes and  $D(l, L)$  is the declination angle (i.e. deviation between magnetic north and true north [31]). Figure 3-9 show a portion of heading (Azimuth) angle estimation using raw magnetometer data. As can be seen in the figure, like tilt angles calculated from accelerometers, the heading angle calculated from magnetometer is very noisy but does not drift with time. In the next section, the EKF that fuses information from AHRS system model that uses the gyroscopes and tilt/heading measurements from accelerometer/magnetometer will be illustrated.

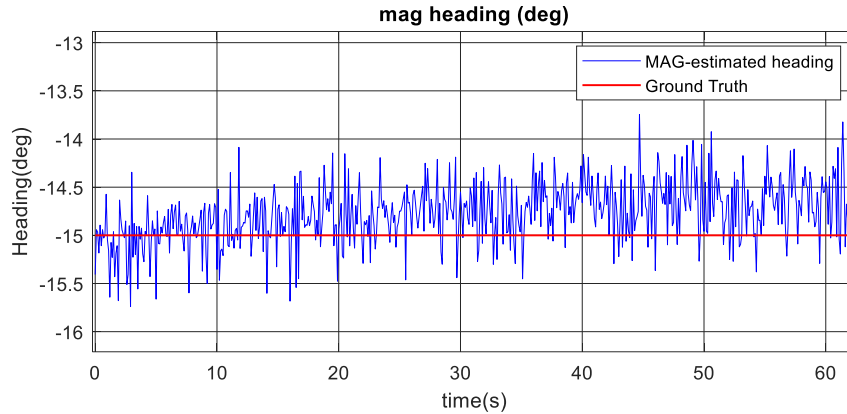


**Figure 3-9: Mag-estimated Heading on Simulated Data**

### **3.6 Integrated AHRS using Extended Kalman Filter (EKF)**

As discussed in earlier sections in this chapter, the basic two sources of information for attitude and heading are AHRS system model from gyroscopes and absolute tilt/heading from accelerometer/magnetometer. The AHRS system model output drifts due to mathematical integration. The accelerometer/magnetometer orientation output do not drift but they are very noisy. Fusing the two sources of information together results in best performance. The fusion will be implemented by an EKF. The EKF theory will be briefly discussed in the next sub-section.

#### **3.6.1 Kalman filter**

Kalman Filter is a form of algorithm used extensively in engineering for estimating unmeasured states of a process, however it was designed based on the assumption that the system is linear. As most practical systems are nonlinear, Extended Kalman Filter (EKF) was developed typically for non-linear discrete-time processes. EKF uses two models, system model and

measurement (update) model. The system model and measurement equations can be represented in the following general form:

$$\dot{x}(t) = f(x(t), u(t)) + w(t) \quad (3.38)$$

$$y(t) = h(x(t)) + v(t) \quad (3.39)$$

where  $x(t)$  is system states,  $u(t)$  is system input signal,  $w(t)$  is process noise and  $v(t)$  is measurement noise. If process noise and measurement noise are zero-mean Gaussian, EKF algorithm can provide an optimal estimation of state error  $\delta x$  by linearizing the system model and measurement model as follows [7]:

$$\delta\dot{x}(t) = F(t)\delta x(t) + G(t)w(t) \quad (3.40)$$

$$\delta y(t) = H(t)\delta x(t) + v(t) \quad (3.41)$$

where  $F$  is called transition matrix,  $G$  is called noise shaping matrix, and  $H$  is called the design matrix.  $F$ ,  $G$  and  $H$  matrices are given by:

$$F(t) = \frac{\partial f}{\partial x} \quad (3.42)$$

$$G(t) = \frac{\partial f}{\partial w} \quad (3.43)$$

$$H(t) = \frac{\partial h}{\partial x} \quad (3.44)$$

assuming  $w(t)$  and  $v(t)$  are zero-mean Gaussian noise with covariance matrices defined by:

$$Q(t) = \langle w(t)w(t)^T \rangle \quad (3.45)$$

$$R(t) = \langle v(t)v(t)^T \rangle \quad (3.46)$$

and  $\delta x$  is error vector with zero-mean and a covariance matrix  $P$  defined by:

$$P(t) = \langle \delta x(t)\delta x(t)^T \rangle \quad (3.47)$$

The optimal estimation of the error vector  $\delta x$  given measurements  $\delta y$  is calculated using two steps: prediction step and update steps. In discrete form, the prediction is given by

$$x_{k+1} = f(x_k, u_k) \quad (3.48)$$

$$P_{k+1} = (I + F_{k+1}T)P_k(I + F_{k+1}T)^T + G_{k+1}Q_{k+1}G_{k+1}^T T^2 \quad (3.49)$$

For simplicity, we will refer to the combined noise matrix  $G_{k+1}Q_{k+1}G_{k+1}^T$  as  $Q_d$ . Update step is implemented by first calculating a correction gain (Kalman Gain):

$$K_{k+1} = P_{k+1}H_{k+1}^T(H_{k+1}P_{k+1}H_{k+1}^T + R_{k+1})^{-1} \quad (3.50)$$

and correct the states by:

$$X_{k+1} = x_{k+1} + K_{k+1}[y_{k+1} - h(x_{k+1})] \quad (3.51)$$

And update the error covariance matrix by:

$$P_{k+1} = (I - K_{k+1}H_{k+1})P_{k+1} \quad (3.52)$$

### 3.6.2 Limitations of EKF

Although EKF is simple and efficient, performance is hugely sensitive to linearization point and noise parameter. If the linearization is performed around a significantly erroneous state, the linearization error will be large, and the filter will likely diverge. This can be avoided by

keeping the state corrected with each measurement update. The noise parameters need to be carefully tuned to avoid performance degradation and divergence, which is the topic of this thesis.

### 3.6.3 Modeling AHRS as EKF problem

#### 3.6.3.1 System Model

To solve the AHRS problem using EKF algorithm, AHRS system model is used as the EKF system model and tilt/heading angles calculated from accelerometer/magnetometer sensors are used as measurement (update models) [56, 57, 58]. The system input to the AHRS model is gyroscope measurement corrected for bias as follows:

$$\omega^b = \omega_m^b - b_g \quad (3.53)$$

where  $\omega_m^b$  is the measured angular rate,  $\omega^b$  is true angular rate,  $b_g$  is the gyroscope bias. The overall AHRS system model is then given by:

$$\dot{q} = \frac{1}{2}\Omega(\omega_m^b - b_g)q + w_q(t) \quad (3.54)$$

$$\dot{b}_g(t) = -\beta b_g(t) + \sqrt{2\beta_g\sigma_g^2}w_u(t) \quad (3.55)$$

where gyro bias ( $b$ ) is modeled as Gauss-Markov process of parameters  $\beta_g$  and  $\sigma_g^2$ ,  $w_u(t)$  is unity zero-mean Gaussian noise and  $w_q$  is the process noise resulting from the gyroscope high-frequency random noise (random walk noise).

#### 3.6.3.2 System States and Process Noise Matrix ( $Q$ )

The states of the system are the quaternion vector ( $q = [a \ b \ c \ d]^T$ ) and gyro bias ( $b_g = [b_x \ b_y \ b_z]^T$ ). However, because the quaternion vector has a redundant variable ( $a$ ), we only need three

variables ( $b, c$ , and  $d$ ) to fully describe the orientation and the forth variable ( $a$ ) can be easily calculated from the three variables using the relationship  $a^2 = 1-(b^2+c^2+d^2)$ . So, the states are given by the following vector:  $[b \ c \ d \ b_x \ b_y \ b_z]^T$  and we have six states in our EKF. The process noise covariance matrix is given by:

$$Q(t) = \langle w_q(t)w_q(t)^T \rangle = \begin{bmatrix} q_b & 0 & 0 & 0 & 0 & 0 \\ 0 & q_c & 0 & 0 & 0 & 0 \\ 0 & 0 & q_d & 0 & 0 & 0 \\ 0 & 0 & 0 & 1 & 0 & 0 \\ 0 & 0 & 0 & 0 & 1 & 0 \\ 0 & 0 & 0 & 0 & 0 & 1 \end{bmatrix} \quad (3.56)$$

### 3.6.3.3 Transition Matrix ( $F$ ) and Noise Matrix ( $G$ )

By linearizing the given AHRS system model, we can obtain the transition matrix  $F$  and noise shaping matrix  $G$ . The values of  $F$  and  $G$  are given by:

$$F = \frac{1}{2} \begin{bmatrix} 0 & (\omega_{m_z}^b - b_z) & -(\omega_{m_y}^b - b_y) & b & c & d \\ -(\omega_{m_z}^b - b_z) & 0 & (\omega_{m_x}^b - b_x) & -a & d & -c \\ (\omega_{m_y}^b - b_y) & -(\omega_{m_x}^b - b_x) & 0 & 0 & 0 & 0 \\ 0 & 0 & 0 & -2\beta_{gx} & 0 & 0 \\ 0 & 0 & 0 & 0 & -2\beta_{gy} & 0 \\ 0 & 0 & 0 & 0 & 0 & -2\beta_{gz} \end{bmatrix} \quad (3.57)$$

$$G = \begin{bmatrix} 1 & 0 & 0 & 0 & 0 & 0 \\ 0 & 1 & 0 & 0 & 0 & 0 \\ 0 & 0 & 1 & 0 & 0 & 0 \\ 0 & 0 & 0 & \sqrt{2\beta_{gx}\sigma_{gx}^2} & 0 & 0 \\ 0 & 0 & 0 & 0 & \sqrt{2\beta_{gy}\sigma_{gy}^2} & 0 \\ 0 & 0 & 0 & 0 & 0 & \sqrt{2\beta_{gz}\sigma_{gz}^2} \end{bmatrix} \quad (3.58)$$

the combined noise matrix used in the EKF equations is defined as

$$Q_d = GQG^T \quad (3.59)$$

### 3.6.3.4 Design Matrix ( $H$ ) and Measurement Covariance Matrix ( $R$ )

The measurement updates to the EKF come from the tilt/heading angles calculated by the accelerometer and magnetometer. Because the states of the EKF are quaternion, we convert the tilt/heading angles into quaternion and apply them as measurement updates to the EKF. In this case, the design matrix  $H$  and the measurement noise covariance matrix  $R$  are given by:

$$H = \begin{bmatrix} 1 & 0 & 0 & 0 & 0 & 0 \\ 0 & 1 & 0 & 0 & 0 & 0 \\ 0 & 0 & 1 & 0 & 0 & 0 \end{bmatrix} \quad (3.60)$$

$$R = \begin{bmatrix} R_r & 0 & 0 \\ 0 & R_p & 0 \\ 0 & 0 & R_h \end{bmatrix} \quad (3.61)$$

The Block diagram of AHRS-EKF framework is shown in Figure 3-10.

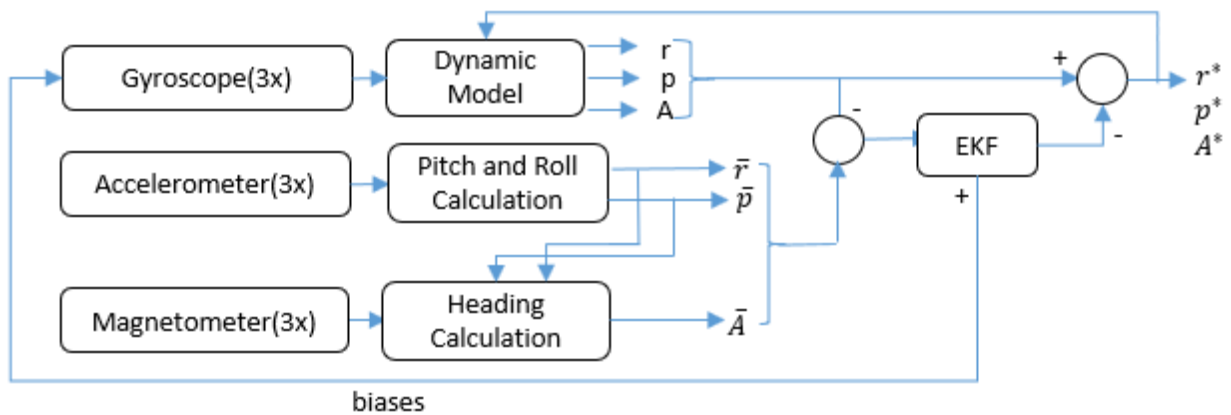


Figure 3-10: Block diagram of AHRS-EKF

### 3.6.4 AHRS-EKF $Q$ and $R$ Parameters Estimation Problem

As described in the previous section, the combined noise matrix  $Q_d$  is directly related to the random walk and Gauss-Markov parameters of the gyroscope measurements. In chapter (2), we discussed how AV can be used to estimate gyroscope random walk noise (used in  $Q$  matrix) and GM can be used to estimate preliminary values for GM parameters (used in  $G$  matrix) by processing long stationary record of gyroscope measurements. However, as will be seen in chapter (4), the preliminary values of  $Q_d$  estimated in this way are not guaranteed to lead to the best EKF performance [55, 59, 60]. As also explained in the previous section, the value of  $R$  represents the noise of the tilt/heading updates calculated from accelerometer/magnetometer. Therefore, there is no direct way to estimate  $R$ . As the performance of an EKF process depends largely on the accuracy of the knowledge of  $Q_d$  and  $R$  matrices, accurate estimation of these parameters is important. In the following chapter, we will explain the proposed procedure to tune these EKF noise parameters.

## 4 Chapter: AHRS using Genetically Optimized Kalman Filter

In this chapter, the proposed EKF noise parameters optimization approach is explained. Firstly, the nominal design point procedure is explained. Secondly, the EKF performance using the nominal design point is evaluated. Thirdly, the DoE analysis is demonstrated. Finally, the GA-based approach is explained.

### 4.1 Nominal Design Point

Nominal design point is an initial value for EKF noise parameters that can be used as a starting point to reach the optimized parameters values. In this work, the nominal design point value for  $Q_d$  parameter is simply calculated by applying AV and GM process modeling as explained in chapter (2). The nominal design value for  $R$  matrix is an initial guess based on preliminary observation of measurements. To keep the scope of varying parameters manageable in this work, we fixed the values of the initial error covariance matrix  $P$  and the random walk noise parameters  $[q_b \ q_c \ q_d]^T$ . So, the only parameters genetically tuned in this work are nine parameters, three gyroscope time constants  $[\beta_{gx} \ \beta_{gy} \ \beta_{gz}]$ , three gyroscope noise standard deviations  $[\sigma_{gx} \ \sigma_{gy} \ \sigma_{gz}]$ , and three angle measurement noise standard deviation  $[R_r \ R_p \ R_h]$  for roll, pitch, and heading updates respectively. The nominal design point is a vector given by:

$$r = [\beta_{gx} \ \beta_{gy} \ \beta_{gz} \ \sigma_{gx} \ \sigma_{gy} \ \sigma_{gz} \ R_r \ R_p \ R_h]$$

### 4.2 EKF Performance using the Nominal Design Point

The accuracy of the EKF using the Nominal Design Point parameters values is demonstrated.

### 4.2.1 Nominal Design Point Results : Simulation Test

In this test, we generated the raw IMU by using a simulator. The raw IMU gyroscope data has been generated and then a bias vector that has fixed value of  $[0.2 \ 0.4 \ 0.6]^T$  °/s and GM-noise of  $[0.01 \ 0.01 \ 0.01]^T$  °/s standard deviation and  $[100 \ 100 \ 100]^T$  seconds time-constant has been added to gyroscope x, y and z axes respectively. In addition, a high frequency random walk noise with standard deviation 0.05 °/s has been added as well. For the simulation data set, the nominal design point vector value was set to the following values:

$$r = [.01\text{deg}/\text{sec} \ .01\text{deg}/\text{sec} \ .01\text{deg}/\text{sec} \ 100\text{sec} \ 100\text{sec} \ 100\text{sec} \ 0.5 \ 0.5 \ 0.5]$$

The results of AHRS-EKF using these noise parameters are displayed in Figure 4-1, Figure 4-2 and Figure 4-3. Root Mean Square Error (RMSE) values for this test are shown in Table 4-1.

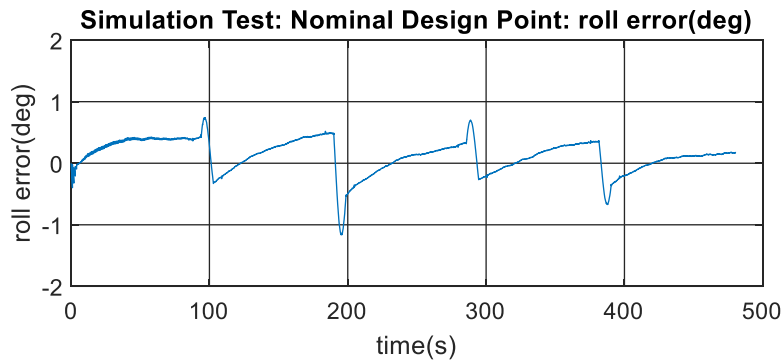


Figure 4-1: Roll error of simulation data using nominal design point

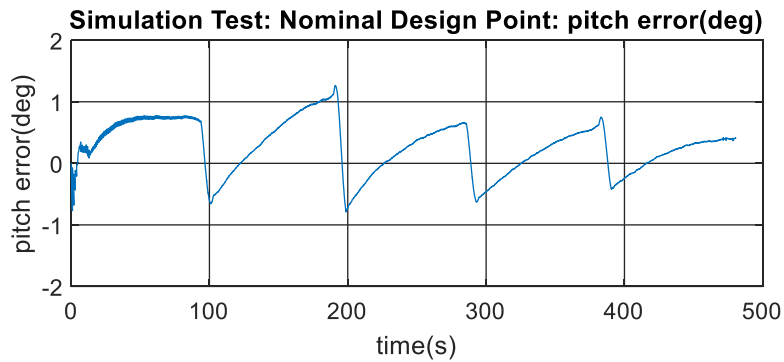
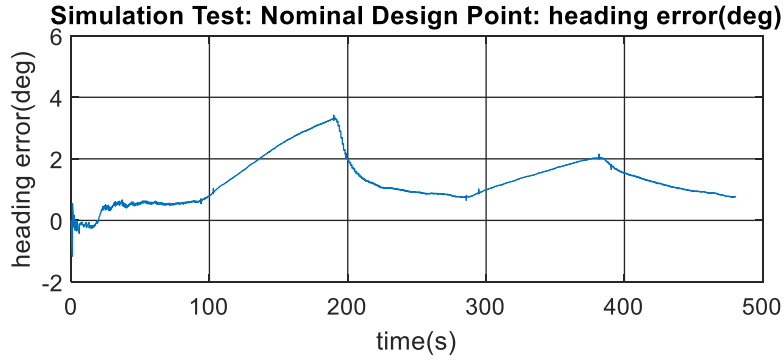


Figure 4-2: Pitch error of simulation data using nominal design point



**Figure 4-3: Heading error of simulation data using nominal design point**

**Table 4-1: Simulation Test: EKF-Performance using Nominal Design Parameters**

Roll RMS error	0.2973 °
Pitch RMS error	0.5021 °
Heading RMS error	1.5978 °
Overall Orientation Error	1.7 °

#### 4.2.2 Nominal Design Point Results: Zero-speed Experimental Test

In this analysis, we used real data from the MPU-9250 IMU. Data has been collected at zero-speed where orientation was changed manually. The magnetometer was already calibrated to obtain stable heading calculation. We took the following nominal design point values taken from the analysis performed in chapter (2):

$$r = [0.46\text{deg/s} \quad 0.44\text{deg/s} \quad 0.44\text{deg/s} \quad 1.62\text{hr} \quad 1.83\text{hr} \quad 1.83\text{hr} \quad 0.5 \quad 0.5 \quad 0.5]$$

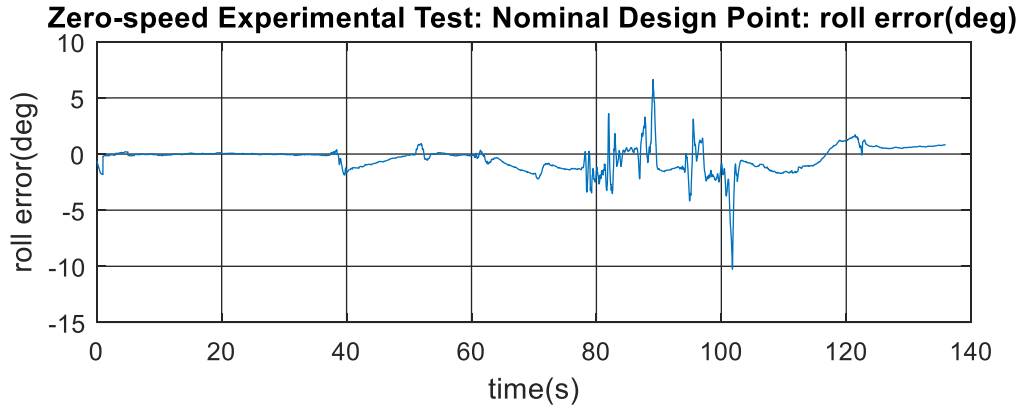


**Figure 4-4: Roll error of zero-speed physical data using nominal design point**

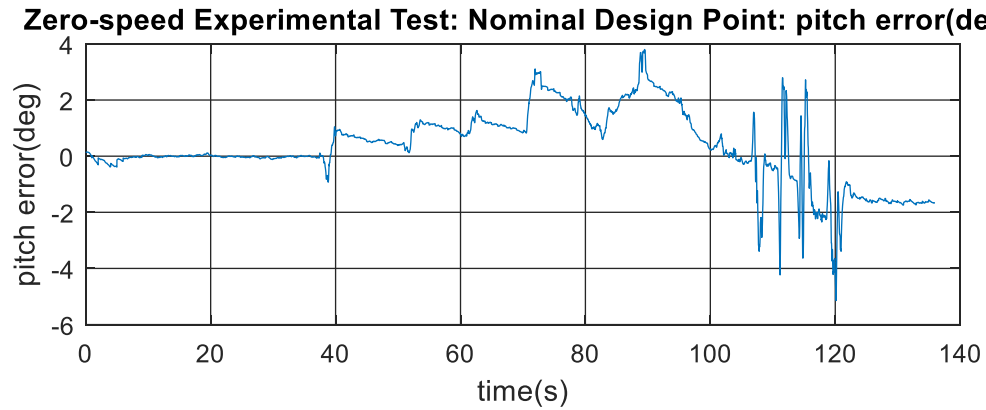


**Figure 4-5: Pitch error of zero-speed physical data using nominal design point**

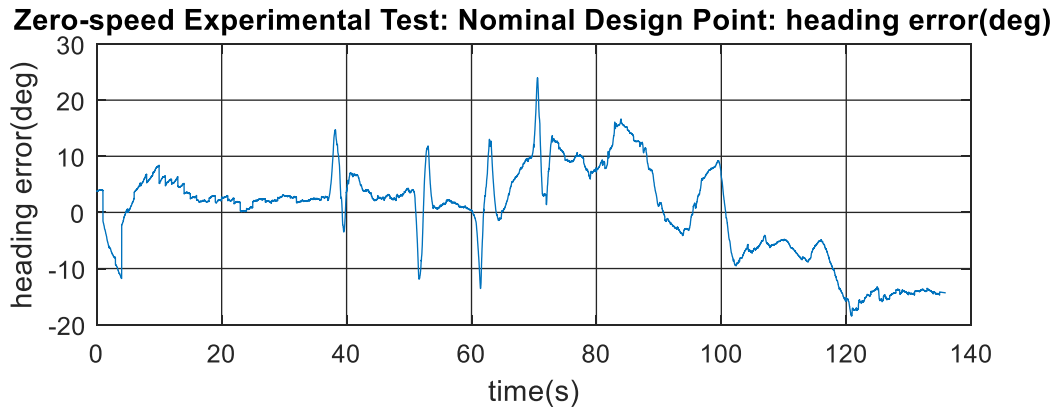


**Figure 4-6: Heading error of zero-speed physical data using nominal design point**

**Table 4-2: Zero-speed experimental Test: Nominal Design Parameters**

Roll RMS error	1.58 °
Pitch RMS error	1.93 °
Heading RMS error	8.13 °
Overall Orientation Error	8.5 °

### **4.3 Design of Experiment Analysis**

To check the optimality of the results of the nominal design point parameters, we applied the DoE approach to check the effect of varying the EKF noise parameters on the performance and compare the results with the nominal design point results. DoE is essentially a systematic method to determine factors affecting a process and its output [61, 62, 63]. It plays an important role in quality of the design, by allowing simultaneous testing of various factors and their effects and thereby facilitating design optimization. The advantages of DoE are; 1) it helps in identifying relationships between process parameters and their effect, 2) it provides an understanding of interactions among causative parameters, and 3) it determines the levels at which to set the controllable parameters to test alternative design and so on.

DoE normally works in four stages, 1) planning, 2) screening, 3) optimization, and 4) testing. Planning stage involves creating a plan for the experimentation. The plan would typically involve how the process parameters will be changed and how their interactions will be measured. During the screening process, large pool of potential factors shows up but not all maybe taken into consideration depending on their effect and their intended use. Next process is optimization to determine the best setting of the parameters that lead to best results. Finally, in the testing stage,

once all the criteria have been met during previous stages the process is tested to make sure it satisfies the desired specifications.

### 4.3.1 Application of DoE on AHRS-EKF Process

For simplicity, we will explain the concept of DoE on only three parameters which are elements of  $R$  matrix of the EKF-AHRS system given by  $R = \text{diag}([R_r \ R_p \ R_h])$ . We will test the effect of varying these three parameters on the accuracy of the orientation estimation results. We will vary the parameters of  $R$  by decreasing and increasing  $R$  values around the nominal design point  $\text{diag}([0.5 \ 0.5 \ 0.5])$ . We will refer to the decreased value by (-1) and increased value by (+1). Since three elements need 8 experiments ( $2^3$ ) for a full factorial experiment assigning a (-1) and (+1) values to each of the parameters. In each test, we varied the  $R$  matrix values and run the EKF and calculated the overall orientation error (RMSE). The results of these experiments are shown in Table 4-4.

**Table 4-3: Low and High Setting for the factors**

Parameter	Low Setting (-1)	High Setting (+1)
$R_r$	0.05	0.95
$R_p$	0.05	0.95
$R_h$	0.05	0.95

**Table 4-4: Error values for changing the R matrix**

Experiment	$R_r$	$R_p$	$R_A$	Overall Orientation Error (deg)
1	0.05	0.05	0.05	0.495
2	0.05	0.05	0.95	0.86
3	0.05	0.95	0.05	0.505
4	0.05	0.95	0.95	0.64
5	0.95	0.05	0.05	0.605
6	0.95	0.05	0.95	0.575
7	0.95	0.95	0.05	0.78
8	0.95	0.95	0.95	0.715

### Effect of changing $R$ matrix parameters

To study the effect of changing one parameter (e.g.  $R_r$ ), we consider the average RMSE in all experiments at which the value of  $R_r$  was increased (+1) (see the red highlighted cells in Table 4-4) and all experiments at which the value of  $R_r$  was decreased (-1) (see the green highlighted cells in in Table 4-4). We then take the average RMSE value in the -1 experiments and the +1 experiments which are given as follow:

$$RMSE(-1)_{R_r} = \frac{0.495 + 0.86 + 0.505 + 0.64}{4} = 0.6250 \quad (4.1)$$

$$RMSE(+1)_{R_r} = \frac{0.605 + 0.575 + 0.78 + 0.715}{4} = 0.6687 \quad (4.2)$$

Then we can calculate the overall average effect of changing  $R_r$  as follows:

$$S_{R_r} = RMSE(+1)_{R_r} - RMSE(-1)_{R_r} \cong 0.044 \quad (4.3)$$

The same procedure can be applied to calculate the average effect of changing  $R_p$  and  $R_h$  which are shown in Figure 4-7. The overall interpretation of Figure 4-7 is that increasing the values of  $R$  will cause larger errors which is expected as  $R$  is an indication of how EKF trusts the values of measurements. However, as can be observed from Figure 4-7,  $R_h$  is the most significant parameter. An increase in  $R_h$  value cause larger increase in RMSE compared to an increase in  $R_r$  and  $R_p$ . This gives an indication that it is more significant to change the value of  $R_h$  parameter. We can perform the same analysis on all the nine parameters in the design vector of the AHRS and study the effect of varying each parameter in the overall RMSE. This analysis will be given in chapter (5).

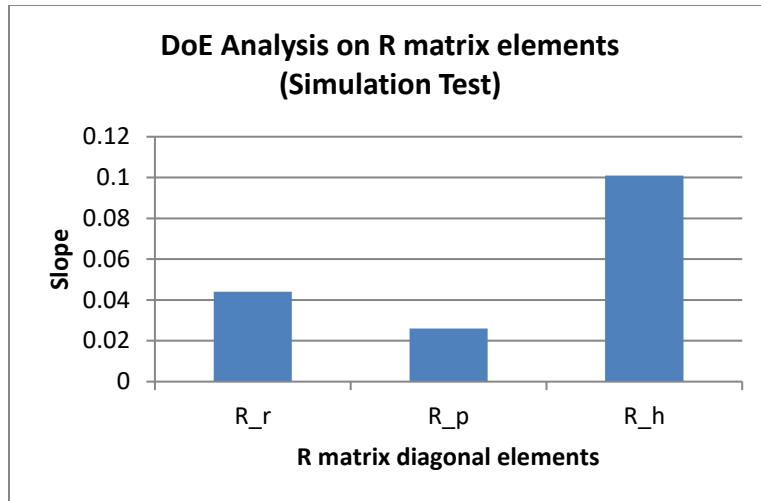


Figure 4-7: Main Effects of  $R$  parameters variations

#### 4.4 Optimizing the EKF parameters using Genetic Algorithms

In the previous sub-section, DoE analysis showed that better accuracy can be achieved by varying the EKF parameters. We also showed how DoE can be used to identify the most significant parameters that cause large change in the RMSE values. To achieve the best accuracy, EKF parameters need to be optimized. In this work, due to the lack of a closed form formula to calculate the optimal values for  $Q$  and  $R$  parameters, we used the GA to perform this optimization.

##### 4.4.1 GA Brief Background

Genetic Algorithm is a search heuristic which may follow one of Darwinian model of evolution– natural selection, Lamarckian Model or Baldwinian Model, for the process of natural selection where the offspring of the next generation are the fittest individuals from a population [64, 65, 66, 67]. Finding practical solution to a complex problem effectively is a job for genetic algorithms, they search through large and complex space environment in which there is a large set of candidate solutions and in which the search space is uneven.

The most widely recognized kind of GA works this way, a population is made with a gathering of individuals made arbitrarily. The individuals in the group are then assessed. In the crossover step, offspring is produced by mating parents and the most common method of production is single point crossover, but other methods can also be used to produce an offspring. Offspring then will take one section of the chromosome from each parent.

An offspring is then created by those individuals that have been chosen, after which the offspring are changed randomly. This proceeds until the point that an appropriate arrangement has been found or a specific number of generations have passed. As to guarantee that the individuals are not all the same, mutation which is the flipping of bits randomly, is done to prevent premature convergence. The probability of mutation is in the range of 1 and 2 tenths of a percent. GA loops over an iteration process with the following general steps to make the population evolve.

- 1) **SELECTION**: selecting individuals for reproduction.
- 2) **REPRODUCTION**: breeding of offsprings by the selected individuals using crossover and mutation.
- 3) **EVALUATION**: evaluation of the fitness of new chromosomes.
- 4) **REPLACEMENT**: replacing old population by the new ones

these overall steps are shown in Figure 4-8. Table 4-5 shows the basic GA algorithm implemented to find the best individual for a fitness function.

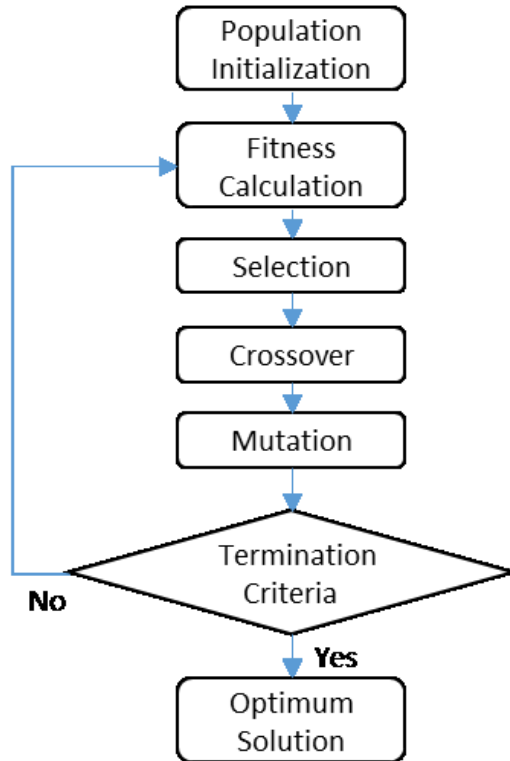


Figure 4-8: Basic structure of Genetic Algorithm

Table 4-5: Basic GA Algorithm

---

**Algorithm 4.1** GA Algorithm

---

- 1: Initialize population
  - 2: find fitness of population
  - 3: **while** (termination criteria is reached) do
  - 4:   parent selection
  - 5:   crossover with probability  $p_c$
  - 6:   mutation with probability  $p_m$
  - 7:   decode and fitness calculation
  - 8:   survivor selection
  - 9:   find best
  - 10: **return** best
-

#### 4.4.2 GA Example

Consider maximizing the following function,

$$f(x) = -x^3 + 30x^2 + 25x + 150, \quad 0 \leq x \leq 31$$

**Step 1:** Coding the variable 'x' into a finite length string can be done using five-bit unsigned binary integer, i.e. 0(00000) to 31(11111).

**Step 2:** Set the size of the population and select the initial population randomly. Initial population of size 5 is chosen in this example as shown in the table below. Note: Based on the requirement and application, any number of population size can be selected.

**Step 3:** Obtain the decoded x values for the generated population. For example, a random binary individual, 01010 is decoded like this,

$$01010 = 0 * 2^4 + 1 * 2^3 + 0 * 2^2 + 1 * 2^1 + 0 * 2^0 = 10$$

Similarly, all the rest of the individuals of the random population are decoded.

**Step 4:** The fitness function is calculated for each x value of the entire population. For example,

$$f(10) = -(10)^3 + 30 * (10)^2 + 25 * (10) + 150 = 2400$$

**Step 5:** Computation of the probability of selection using the formula,

$$\text{Prob}_i = \frac{f(x)_i}{\sum_{i=1}^n f(x)_i}$$

Where  $n$  is the number of the individuals in the population. Considering string 1,

$$\text{Prob}_1 = \frac{f(x)_1}{\sum_{i=1}^5 f(x)_i} = \frac{2400}{13818} = 0.1592$$

And the percentage probability is just 15.92%. The Probabilities of each are filled in the table.

**Step 6:** Now the expected count is calculated as

$$Expected\ count = \frac{f(x)_i}{(Avg(f(x)))_i}$$

$$(Avg(f(x)))_i = \frac{\sum_{i=1}^n f(x)_i}{n}$$

So expected count of string 1 is  $2400/3015.6=0.7956$  and the rest can also be calculated similarly.

**Step 7:** The next step is to find the actual count to select the individuals for the crossover cycle using Roulette wheel selection. The Roulette wheel, as shown below, is of 100% and the probability of selection for each individual is used as indicator to fit into the Roulette wheel.

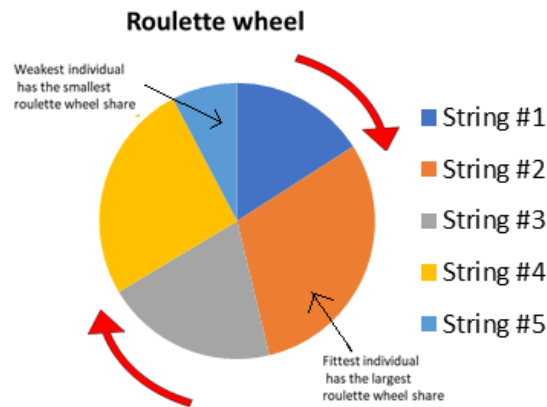


**Figure 4-9: Roulette wheel selection**

**Step 7:** Next, we write the mating pool based upon the actual count. The actual count of string no 1 is 1, hence it occurs once in the mating pool. The actual count of string no 2 is 2, hence it occurs twice in the mating pool. Since the actual count of string no 5 is 0, it does not occur in the mating pool. Similarly, the actual count of string no 3 and 4 being 1, they occur once in the mating pool.

**Table 4-6: GA Selection**

String No.	Randomly Selected Initial Population	x value	Fitness Value f(x)	Prob <sub>i</sub>	Percentage Probability	Expected Count	Actual Count
1	01010	10	2400	0.1592	15.92%	0.7956	1
2	10110	22	4572	0.3032	30.32%	1.5161	2
3	01100	12	3042	0.2017	20.17%	1.0088	1
4	11011	15	3900	0.2586	25.86%	1.2933	1
5	00110	6	1164	0.0772	7.72%	0.3859	0
Sum			15078	1.0000	100%	5.0000	5
Average			3015.6	0.2000	20%	1.0000	1
Maximum			4572				

**Step 8:** Single point crossover is performed where the crossover point is set to produce new offspring.

**Step 9:** ‘x’ values are decoded, and fitness values are re-calculated.

**Table 4-7: GA Crossover**

String No.	Mating Pool	Crossover point	Offspring after Crossover	x value	Fitness Value f(x)
1	01010	3	01110	14	3636
2	10110	3	10010	18	4488
2	10110	4	10100	24	4206
3	01100	4	01110	14	3636
4	11011	0	11011	15	3900
Sum					19866
Average					3973.2
Maximum					4488

**Step 10:** Mutation-flipping operation with a probability of 0.4 (but usually a very small number is chosen) results in new off springs as shown in the table below and ‘x’ values and fitness values are computed to complete one generation.

**Table 4-8: GA Mutation**

String No.	Offspring after crossover	Mutation Chromosomes	Offspring after mutation	x value	Fitness value f(x)
1	01010	00100	01110	14	3636
2	10110	00000	10110	18	4488
2	10110	00000	10100	24	4206
3	01100	10000	11100	28	2418
4	11011	00000	11011	15	3900
Sum					18648
Average					3729.6
Maximum					4488

These tables showed how the performance was improved from an average of 3015.6 to an average of 3729.6 in just one generation. Figure 4-10 shows the GA calculated in the first generation versus the absolute maximum of the function in the given range. This is a simple example to show how effective GA is and to elaborate the steps involved.

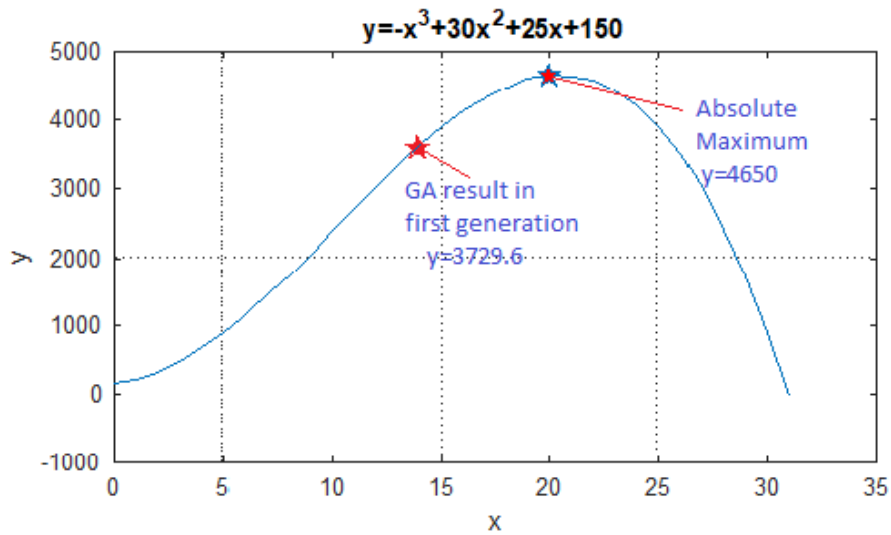


**Figure 4-10: GA Illustrative Example: maximizing a simple function**

#### 4.5 Application of GA to EKF-based AHRS

To benefit from the GA optimization capability in the EKF-AHRS system, we will model the design vector as the individual and we will apply the GA to find the best design vector that minimize the overall orientation RMSE in contrast to the work done in [68] [22] [69]. In GA, we can set boundaries or constraints on the values that the individual may take. In this thesis, to accelerate the processing of the GA, we will set lower and upper bounds values on the parameters in the design vector such that the most significant parameter which has greater effect on the RMSE reduction will have larger room for variation. For example, we set the allowable range of values for the parameter  $R_r$  as  $[R_{r_{nom}} - S_{R_r} C_{R_r}, R_{r_{nom}} + S_{R_r} C_{R_r}]$  where  $S_{R_r}$  is the DoE slope of  $R_r$  and  $C_{R_r}$  is a constant factor. This formula will make sure that each parameter has a range of possible values that is proportional to its contribution in the overall RMSE minimization. The overall EKF tuning procedure is given in Figure 4-11 . In the next chapter, chapter (5), we will apply the proposed tuning procedure on both simulation data and physical data and discuss the results.

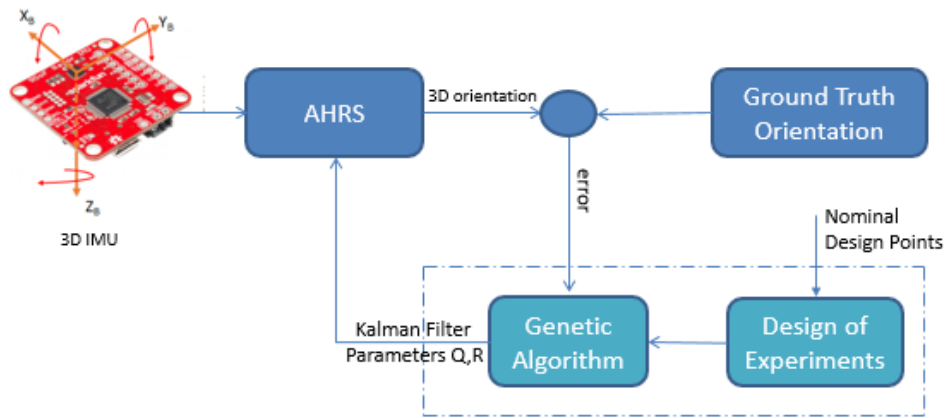


Figure 4-11: The proposed EKF tuning procedure

## 5 Chapter: Simulation and Experimental Results

In this chapter, we apply proposed noise parameter optimization method described in Chapter 4 to the AHRS-EKF problem. We start from the Nominal Design Point set described in Section 4.1 to evaluate the performance of the EKF-based AHRS and compare the results of the proposed parameter optimization method. We start by describing the data and then apply the EKF using the Nominal Design Point and apply the proposed GA-based optimization method and compare the filter performance in terms of orientation root mean square error (RMSE).

### 5.1 Simulation Test

The simulation environment is where the reference data was taken from a raw IMU data that was generated from a reference ground-truth trajectory. If position, velocity, and orientation of an object are available, inverse kinematics can be applied to generate error-free raw IMU data. To test the EKF under noise, different kinds of noises have been added to the raw IMU data to simulate a realistic environment.

#### 5.1.1 Ground Truth Data

Figure 5-1 below shows roll, pitch and heading angles in degrees versus time in seconds of ground truth simulated angles which serves as a reference.

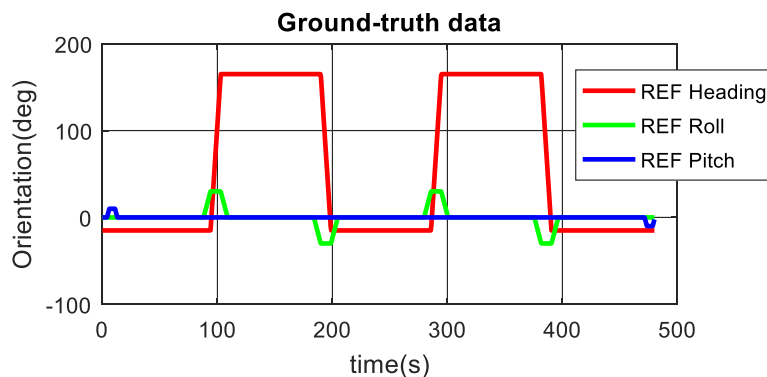


Figure 5-1: Ground Truth Simulated Angle

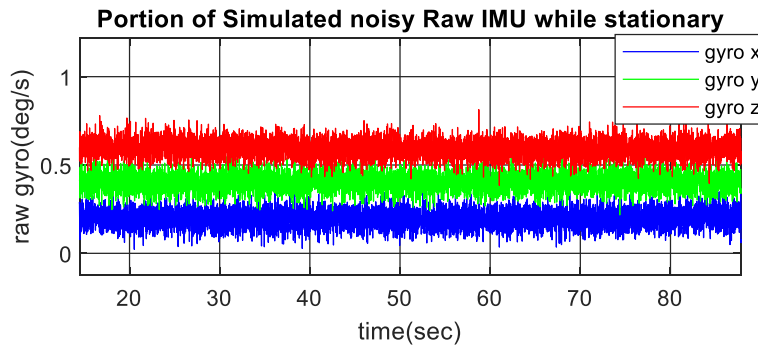
### 5.1.2 Simulation Noise Parameters

Table 5-1 below shows gyro and accelerometer noise parameters and their values that were added to simulate a raw IMU data, to make it close to real world performance.

**Table 5-1: Gyro and Accelerometer Noise parameters**

Gyro Noise Parameters	Value
Gauss-Markov Time constant vector (sec)	[100 100 100] <sup>T</sup>
Gauss-Markov Standard Deviation (°/sec)	[0.01 0.01 0.01] <sup>T</sup>
Random Walk Noise Standard Deviation (°/sec)	[0.05 0.05 0.05] <sup>T</sup>
Deterministic Bias Vector (°/sec)	[0.2 0.4 0.6]
Accelerometer Noise Parameters	Value
Random Walk Noise Standard Deviation (m/sec <sup>2</sup> )	[0.0048 0.0048 0.0048] <sup>T</sup>

Figure 5-2 below shows sample of simulated noisy raw IMU gyro output in (deg/s) while stationary for all (3) X, Y and Z axes plotted against time in seconds. Figure 5-3 shows part of simulated noisy raw IMU accelerometer in meters per second squared while stationary for X and Y axes versus time in seconds. Figure 5-4 shows portion of the simulated raw magnetometer data. To generate noisy magnetometer data, a 0.5° orientation error was added to the direction cosine matrix used to generate the raw magnetometer data.



**Figure 5-2: Portion of simulated noisy raw gyro stationary output**

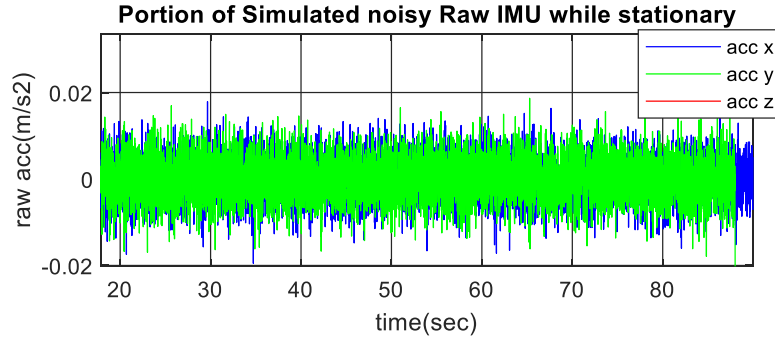


Figure 5-3: Portion of simulated noisy raw accelerometer stationary output

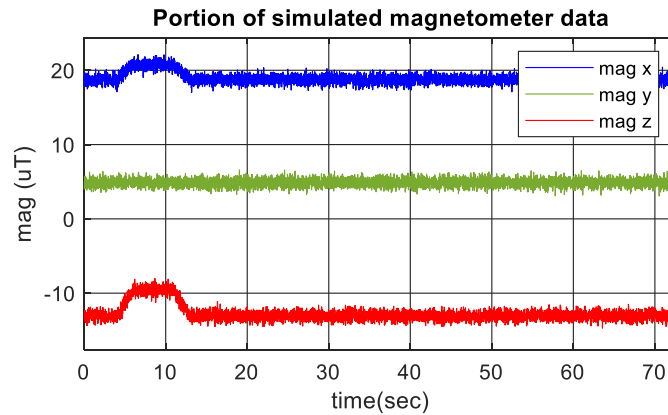


Figure 5-4. Portion of Simulated Raw Magnetometer Data

For the measurement noise matrix  $R$ , we set the nominal design value shown below:

$$R = \begin{bmatrix} R_r & 0 & 0 \\ 0 & R_p & 0 \\ 0 & 0 & R_h \end{bmatrix} = \begin{bmatrix} 0.5 & 0 & 0 \\ 0 & 0.5 & 0 \\ 0 & 0 & 0.5 \end{bmatrix} \quad (5.1)$$

### 5.1.3 Nominal Design Point Results on Simulation Data

As the data has been generated by simulation, the true values of both the system process noise  $Q$  and measurement noise  $R$  are known and they should lead to the best performance. We will verify this by comparing the results of the nominal design point and the genetically optimized EKF. It should be expected that the genetically optimized EKF should lead to similar results to the design point in this simulation test.

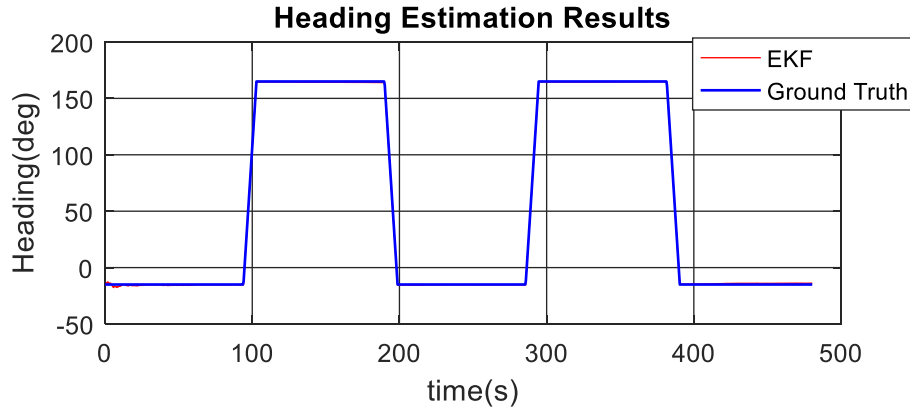


**Figure 5-5: Heading performance using nominal design point**

Figure 5-5 illustrates the similarities between heading result from the nominal design points and the heading from ground truth data, all plotted against time from 0 to 500 seconds. From this observation, although heading and ground truth both yield similar curves the small errors at each sample point resulted in sum of heading error which becomes significant as time passes.

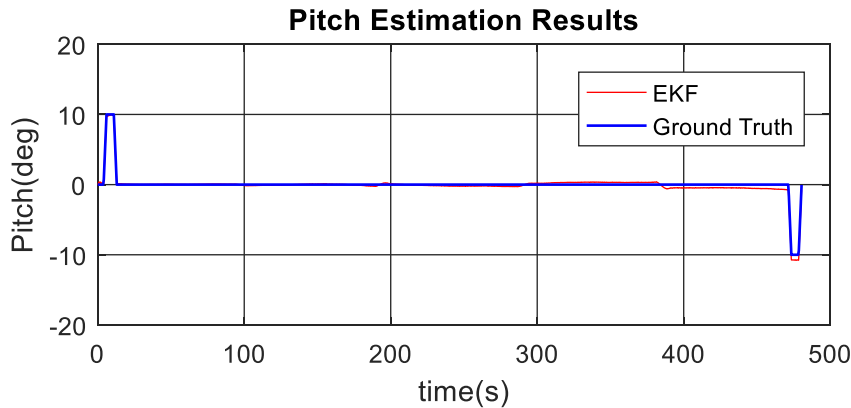


**Figure 5-6: Pitch performance using nominal design point**

Figure 5-6 shows the similarities between reference pitch and pitch data calculated from the nominal design points versus time in seconds. It can be seen that there isn't much difference between the reference pitch and pitch in the earlier stage, from 0 to 300 seconds. After the 300 second's time sample the difference started to increase slightly between both. Figure 5-7 shows the illustration of the difference in variation of the reference roll and roll from nominal design

points by plotting both versus time in seconds. From the observation it can be seen that during the time of 0 to 500 seconds the deviation between them is less compared to the pitch and heading errors as discussed in the previous figures.

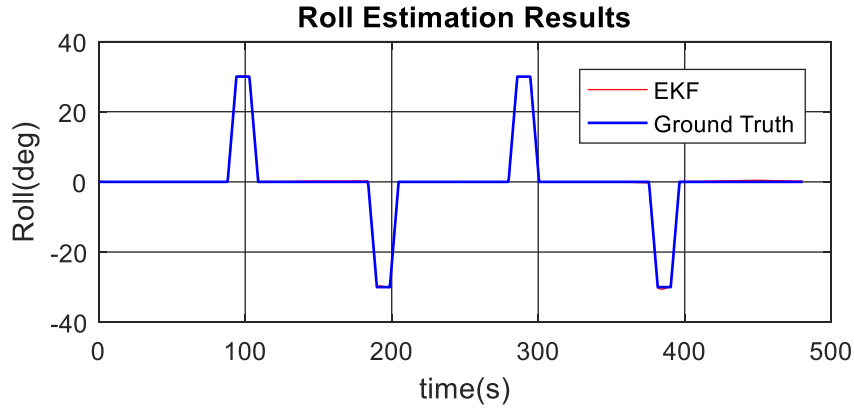


**Figure 5-7: Roll performance using nominal design point**

**Table 5-2: Performance of the EKF using nominal design parameters**

	<b>RMSE(deg)</b>
<b>Roll</b>	0.1763
<b>Pitch</b>	0.2912
<b>Heading</b>	0.6731
<b>Overall Orientation Error</b>	0.7543

Table 5-2 summarizes the roll, pitch and heading errors and sums them to get the RMS overall orientation error in degrees. Those error values show that the heading produced most of the error.

#### **5.1.4 Genetic Algorithm Results on Simulation Data**

In this section, we will apply the proposed parameters optimization method on the simulation data. As the nominal design point was already set to the noise parameters we already used to generate the simulation data, it is expected that the gain from applying the proposed

algorithm will be insignificant. We run the GA optimization using MATLAB GA toolbox on a TOSHIBA laptop with intel-iCore7 dual-core 2.4 GHz processor with 16GB RAM running Windows 10. MATLAB R2018a was used. The computation performance is measured in terms of number of GA generations used to get acceptable solution.

#### 5.1.4.1 DoE Analysis

Applying DoE to the simulation data set, to find out which of the parameters were more significantly affecting the EKF tuning, Figure 5-8 was plotted. The DoE analysis was applied on the 9 design parameters and overall orientation error in degrees is plotted against slope in Figure 5-8. As it can be seen the gyro z stdv parameter in the Q matrix and the roll and pitch parameters in the R matrix were much more significant than the rest implying that by directing the GA in this direction , we can tune the EKF faster.

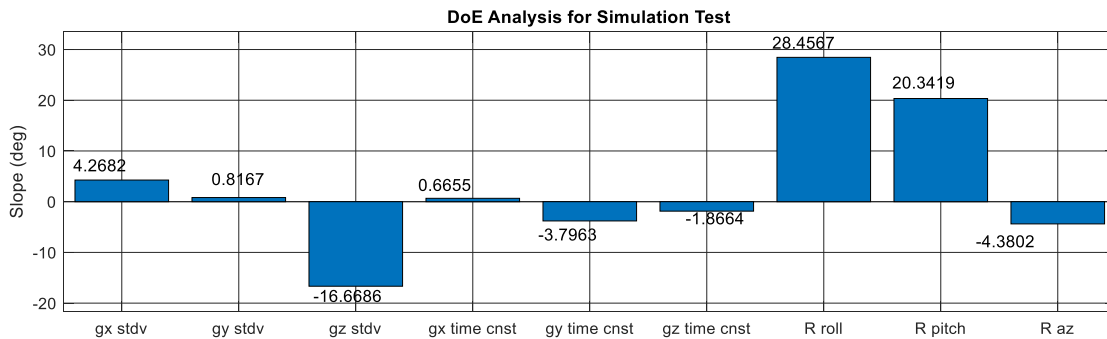


Figure 5-8: DoE Pareto Charts for the Q and R parameters of the Simulation Test

#### 5.1.4.2 GA Results

The implementation of the GA is tested on the simulation data set without combining the DoE analysis first and the result is plotted. Then the same procedure is taken by combining the DoE with the GA and the result are summarized for comparison.

## GA without DoE

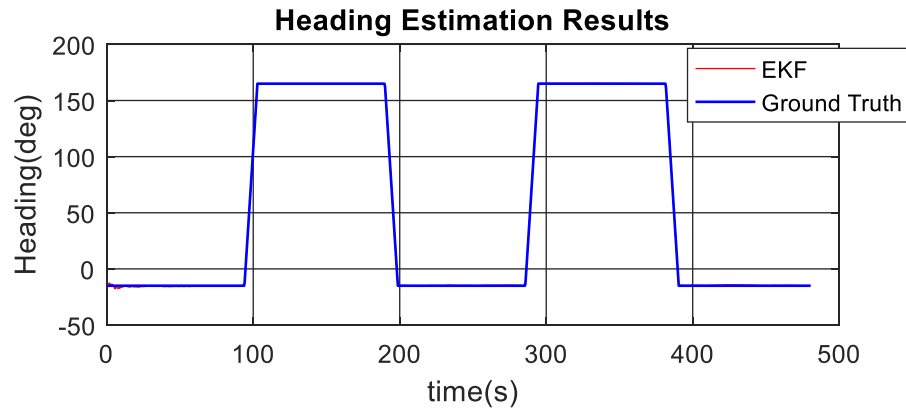


Figure 5-9: Heading angle output from GA only

Heading is calculated from the GA using the nominal design points listed in section 4.2.1 as initial values and setting the lower and upper bound for each of those parameters. Figure 5-9 illustrate the similarities between heading angle output from this algorithm and ground truth data in degrees, all plotted against time in seconds. From observation, heading and ground truth both yield similar curves between 0 to 500 second interval but those small errors added up to near a half a degree error through this short time.

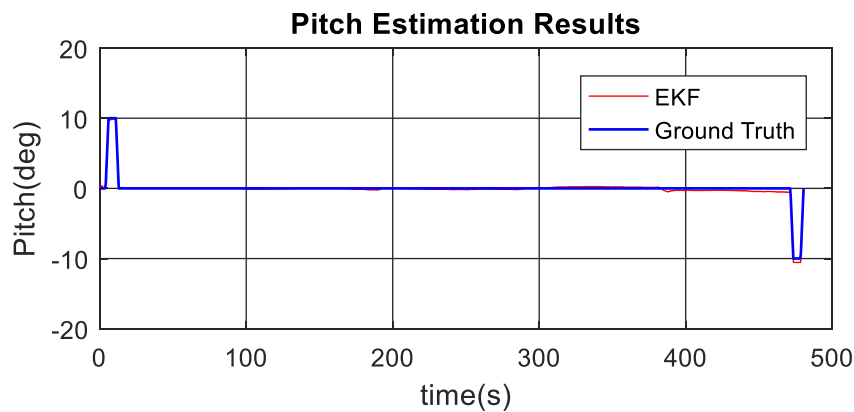
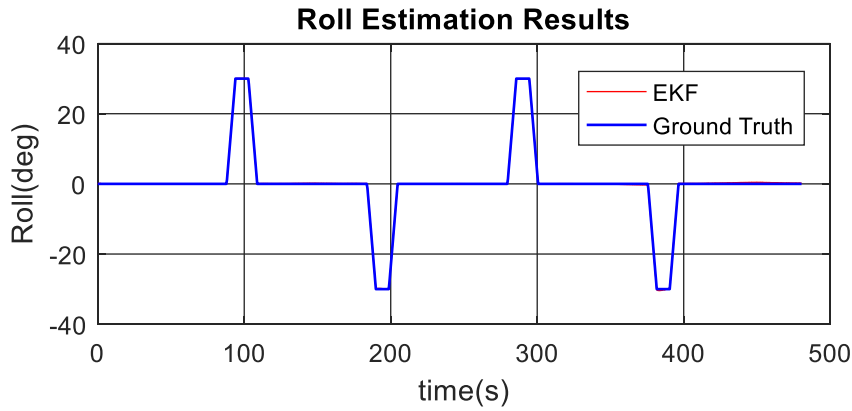


Figure 5-10: Pitch output from GA only on simulation data

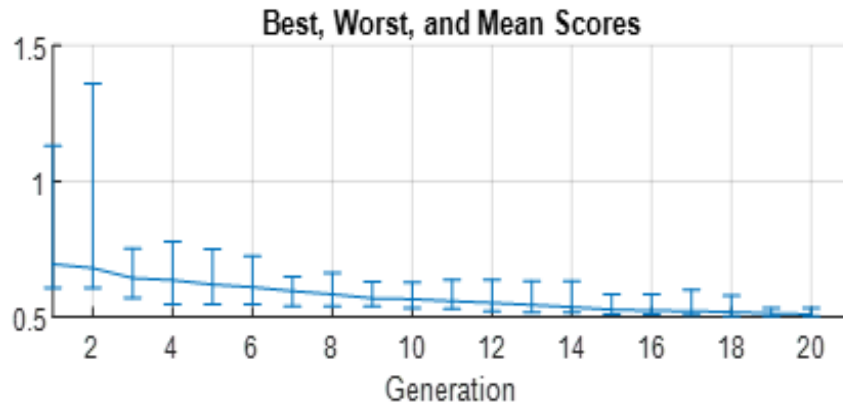
Similarly, Figure 5-10 plots reference pitch against pitch calculated using GA, plotted against pitch in degree versus time in seconds. As it can be seen, there isn't much difference

between the reference pitch and pitch from GA in the earlier stage, from 0 to 200 seconds. However, after 200 seconds interval, the difference started to increase slightly between both and the two colors begin to be seen obviously.



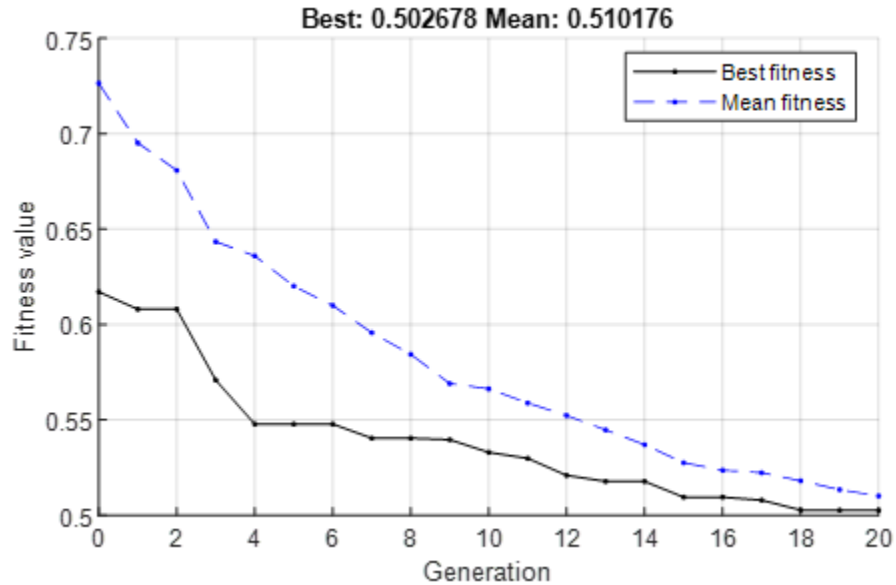
**Figure 5-11: Roll output from GA only on simulation data**

Figure 5-11 shows the illustration of the variation of the reference roll plotted against roll from GA in degrees versus time in seconds. From this observation, during the time of 0 to 500 seconds there wasn't much deviation from the reference.



**Figure 5-12: Best, worst and Mean scores for twenty generations of GA**

The fitness value of the best individuals versus generations is plotted in Figure 5-12 above. It shows the best, the worst and the mean scores that were obtained during the test for twenty generations.



**Figure 5-13: Best and Mean fitness values for GA optimization on simulation data**

Also, as shown in Figure 5-13, the best individual and the mean fitness differed when plotted together for twenty generations. The mean started converging after some iterations. GA converged to the design point value with slight improvement and the error values are summarized in Table 5-3. It gives the RMS error for each roll, pitch, heading and then the overall orientation errors in degree. Results are slightly better than the nominal design point parameters. However, as expected, the difference in the performance is not very significant because the nominal design point is taken from the true noise parameters set by the simulator.

**Table 5-3: EKF-Performance using GA without DoE for the simulation test**

	<b>RMSE (deg)</b>
<b>Roll</b>	0.1619
<b>Pitch</b>	0.2066
<b>Heading</b>	0.4342
<b>Overall Orientation Error</b>	0.507

### **GA with DoE**

The next procedure is introducing the DoE analysis result into the GA algorithm. Here, the ranges of GA upper and lower bounds for those tuning parameters are adjusted according to their significance based on the DoE analysis that we obtained. For instance, the R\_roll parameter in the R matrix has the highest range while the gyro x time constant has the lowest range referring to Figure 5-8. Figure 5-14 shows GA fitness curves with and without DoE for simulation data. The GA with DoE was able to find a better fitness value in a shorter time and converged quickly to a better result (less overall orientation error) compared to GA without DoE. The orientation error values for this test are shown in Table 5-4.

**Table 5-4: EKF-Performance using GA with DoE the simulation test**

	<b>RMSE (deg)</b>
<b>Roll</b>	0.1853
<b>Pitch</b>	0.1578
<b>Heading</b>	0.4159
<b>Overall Orientation Error</b>	0.4819

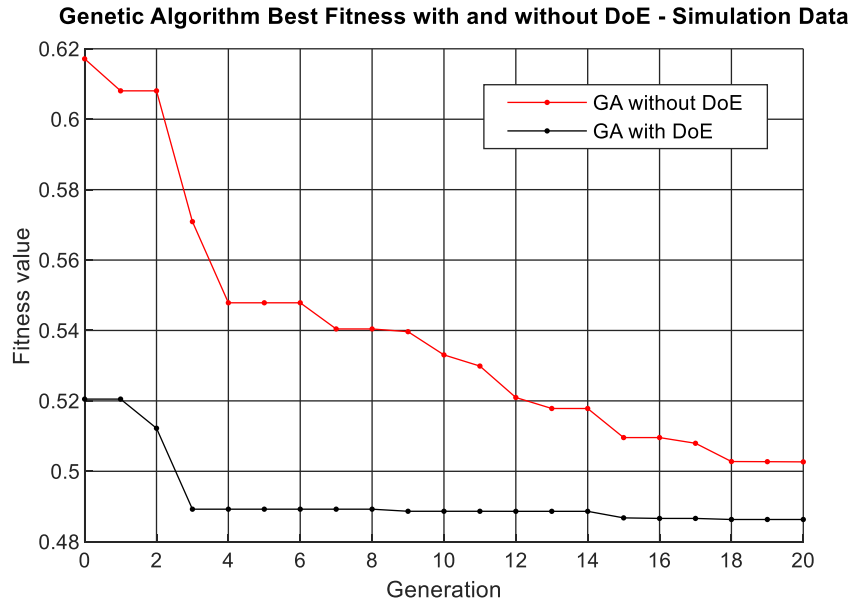


Figure 5-14: Comparison of GA fitness values with and without DoE

## 5.2 Zero-speed Experimental Test

In this test, zero-speed data has been collected by the reprogrammable SparkFun 9DoF Razor IMU-M0 which combines a SAMD21 microprocessor with an MPU-9250 9DoF IMU featuring three-axes accelerometer, gyroscope, and magnetometer sensors. The IMU orientation was changed manually while being stationary (no linear motion).

### 5.2.1 Ground-Truth Data and Raw IMU Data

The ground-truth was generated by applying post-processing smoothing to the angles estimated by well-calibrated accelerometer and magnetometer. Figure 5-15 shows raw gyroscope data in deg/sec plotted versus time in seconds. Figure 5-16 shows raw accelerometer data for all three axes. Measurements in the Z axis are affected the most by gravity from the start. Similarly, Figure 5-17 shows raw magnetometer data for all three axes. Figure 5-18 show the reference heading, roll and pitch angles plotted against time in seconds.

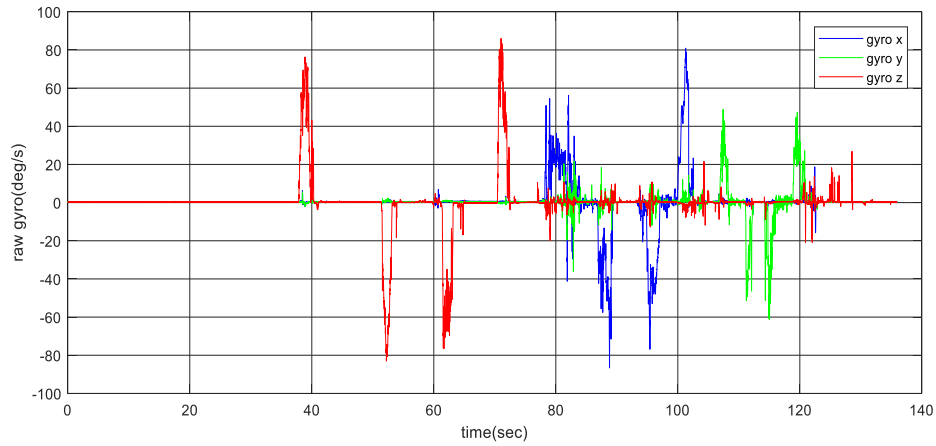


**Figure 5-15: Raw Gyro data of the Experimental Zero-speed Test**

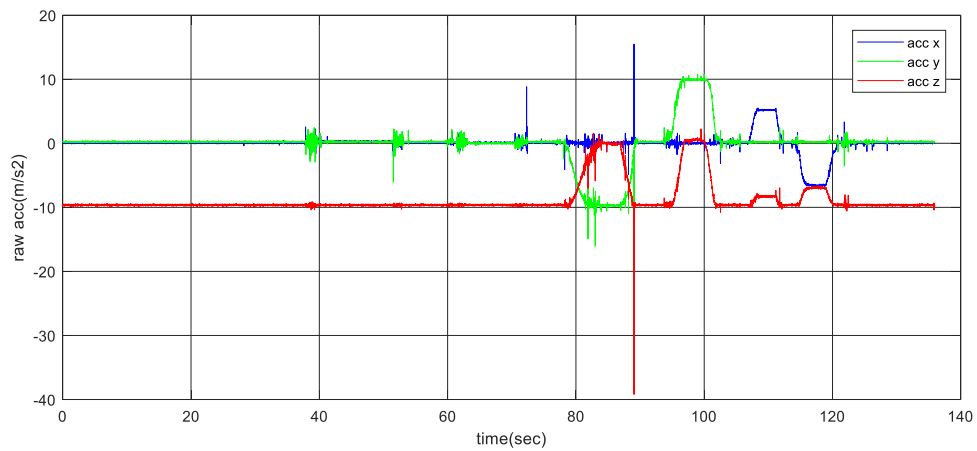


**Figure 5-16: Raw Accelerometer data of the Zero-speed Test**

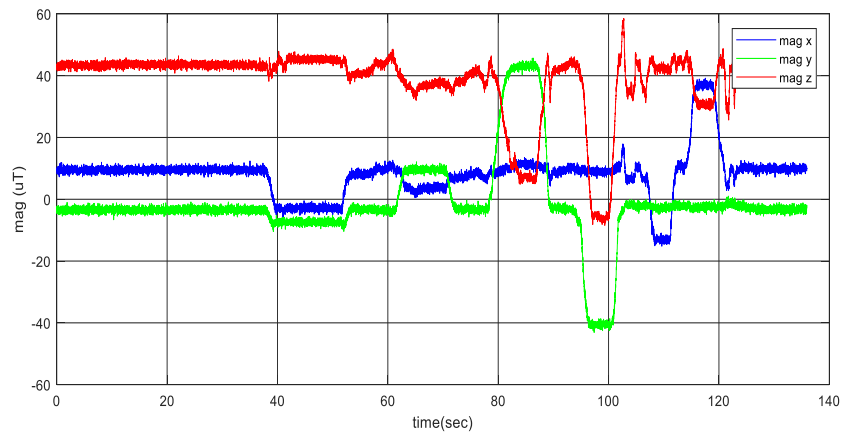


**Figure 5-17: Raw Magnetometer data of the Experimental Zero-speed Test**

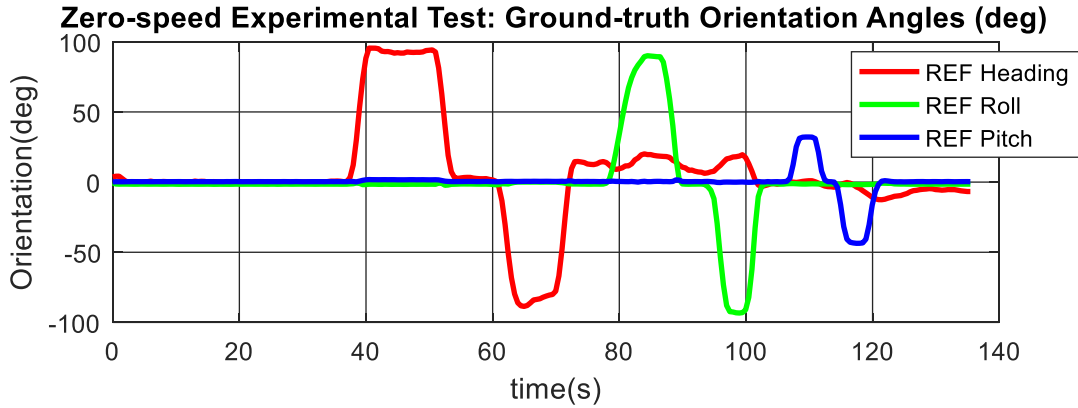


Figure 5-18. Ground-Truth Angles to evaluate the proposed EKF-design

### 5.2.2 Nominal Design Point

Nominal design points were obtained by applying GM and AV methods on a 7 hours records of stationary (no linear motion and no orientation changes) data collected. After the computation and plotting of the autocorrelation function, the gyro time constants and Gauss-Markov standard deviation were calculated for all the three axes. The estimated gyro standard deviation and time constants are used as the nominal design point. The values of the nominal design points for this test are listed in Table 5-5.

Table 5-5: GM-Estimated Noise Parameters

$\tau_{\omega_x}(h)$	$\tau_{\omega_y}(h)$	$\tau_{\omega_z}(h)$	$\delta_{\omega_x}(^{\circ}/s)$	$\delta_{\omega_y}(^{\circ}/s)$	$\delta_{\omega_z}(^{\circ}/s)$
1.62	1.83	1.83	0.46	0.44	0.44

The nominal  $R$  matrix parameters were set to 0.5 each to give the following diagonal matrix:

$$R = \begin{bmatrix} R_r & 0 & 0 \\ 0 & R_p & 0 \\ 0 & 0 & R_h \end{bmatrix} = \begin{bmatrix} 0.5 & 0 & 0 \\ 0 & 0.5 & 0 \\ 0 & 0 & 0.5 \end{bmatrix}$$

### 5.2.3 Nominal Design Point Results on Zero-speed Experimental Test

At first, like the simulation test procedure done in section 5.1, the experimental data set was tested using the nominal design points. Figure 5-19 shows comparison of experimental test heading data against the ground truth in degrees plotted versus time in seconds. Although, up to approximately the 60th second time step the heading output was able to follow the ground truth closely with a little drift initially, it is observed to introduce more error and drift more as time increased. Figure 5-20 illustrates the comparison of roll result and reference roll in degrees plotted against time in seconds. From observation it can be noted that during this period it was able to follow the ground truth curve and the error stayed relatively at the smaller degree. Figure 5-21 shows the comparison between pitch and reference pitch, with roll/pitch in degrees on the vertical side and time in seconds on the horizontal axis of the figure. The resulting pitch doesn't deviate that much from the reference pitch in the first half of the period but in the latter stages the difference between the two gets larger. Figure 5-22 show the gyro biases estimation. Table 5-6 shows a summary of the error the error with the heading RMS error being the largest.

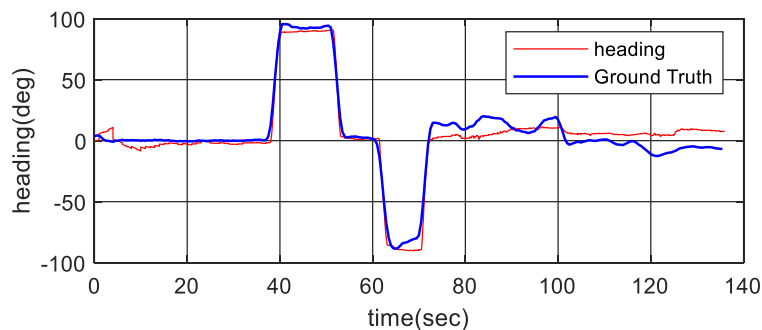
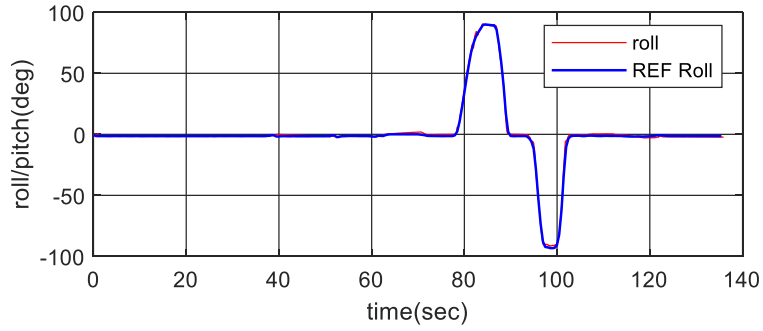
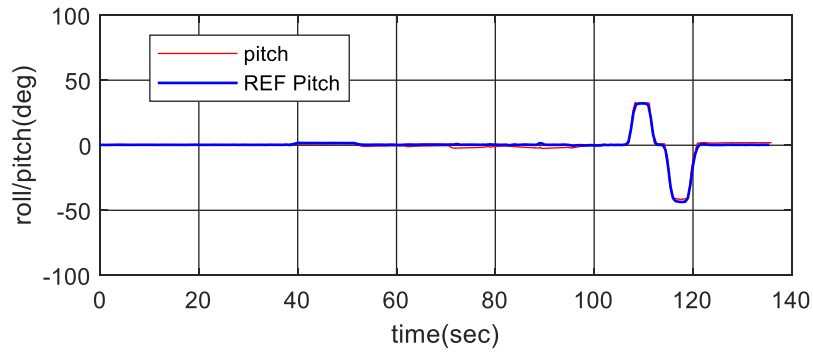


Figure 5-19: Heading results for zero-speed experimental test using nominal design point



**Figure 5-20: Roll results for zero-speed experimental test using nominal design point**



**Figure 5-21: Pitch results for zero-speed experimental test using nominal design point**

**Table 5-6: EKF results for zero-speed experimental test using nominal design point**

	<b>RMSE (deg)</b>
<b>Roll</b>	1.58 °
<b>Pitch</b>	1.93 °
<b>Heading</b>	5.13 °
<b>Overall Orientation Error</b>	5.71 °

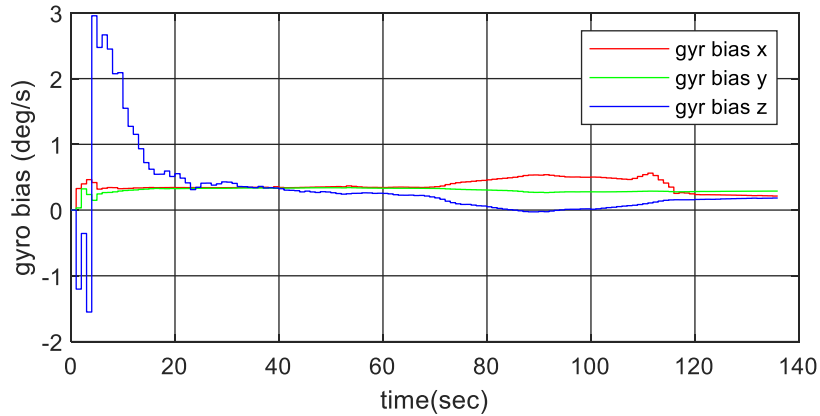


**Figure 5-22: Gyro biases estimation for the zero-speed experimental test**

### **5.2.4 Genetic Algorithm Results on Zero-speed Experimental Test**

In this sub-section, the GA optimization was run using MATLAB GA toolbox on a TOSHIBA laptop with intel-iCore7 dual-core 2.4 GHz processor with 16GB RAM running Windows 10. MATLAB R2018a was used. The computation performance is measured in terms of number of GA generations used to get acceptable solution. The population size was set to 50 and the maximum number of generations was set to 20.

#### **5.2.4.1 DoE Analysis**

DoE was applied to the real data, to find out which of the tuning parameters were more significantly affecting the EKF performance, and the pareto charts was plotted in Figure 5-23. It is observed that the roll and pitch parameters in the R matrix were much more significant than the rest implying that by directing the GA in this direction , we can tune the EKF faster.

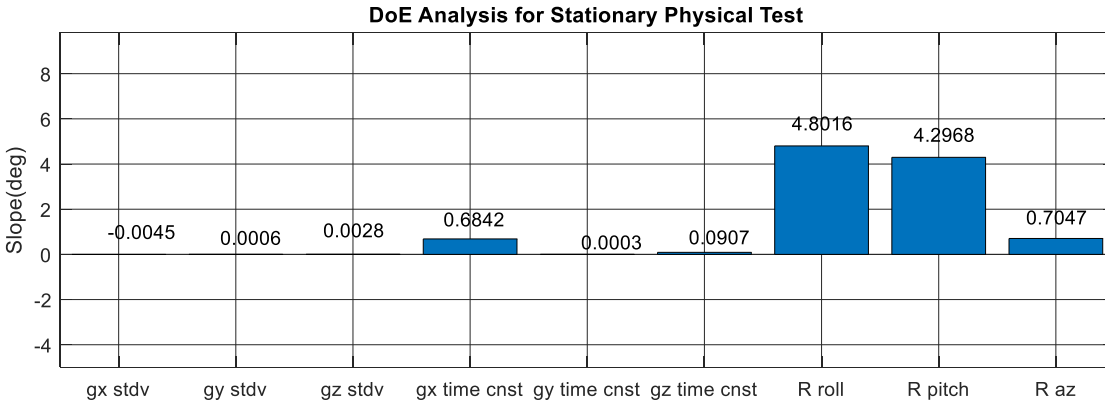


**Figure 5-23: DoE Pareto Charts for the Q and R parameters of zero-speed experimental test**

### 5.2.4.2 GA Results

The implementation of the GA is tested on the experimental data set without combining the DoE analysis first and the result is plotted. Then the same procedure is taken by combining the DoE with the GA and the results are summarized for comparison.

#### Results of GA without DoE

The fitness value of the best individuals when implementing GA without considering the DoE analysis is plotted in Figure 5-24 below. It shows the best, the worst and the mean scores that were obtained during the physical test for twenty generations. Also, as shown in Figure 5-25, the best individual and the mean fitness differ when plotted together for twenty generations. The best-fit convergence happened at the 16<sup>th</sup> generation. The numerical error value is shown in Table 5-7. As the table shows, the results are better than those of the nominal design point shown in Table 5-6 .

**Table 5-7: EKF-Performance using GA without DoE for the Physical Stationary Test**

	RMSE(deg)
<b>Roll</b>	0.27°
<b>Pitch</b>	0.15 °
<b>Heading</b>	3.90 °
<b>Overall Orientation Error</b>	3.91 °

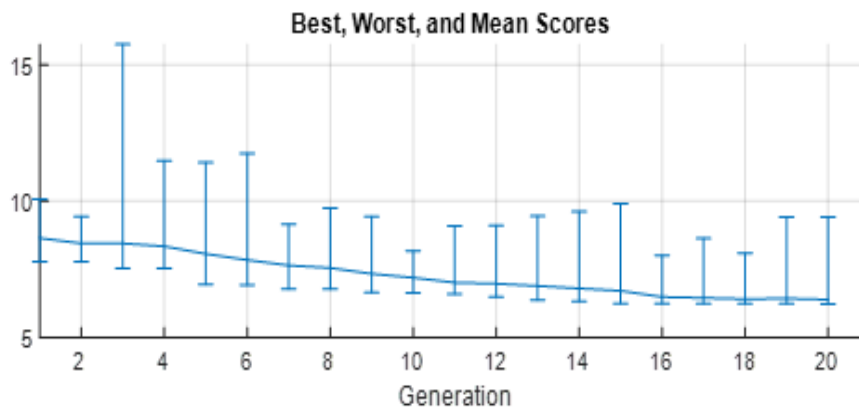


**Figure 5-24: Best, worst and Mean scores for twenty generations of GA**

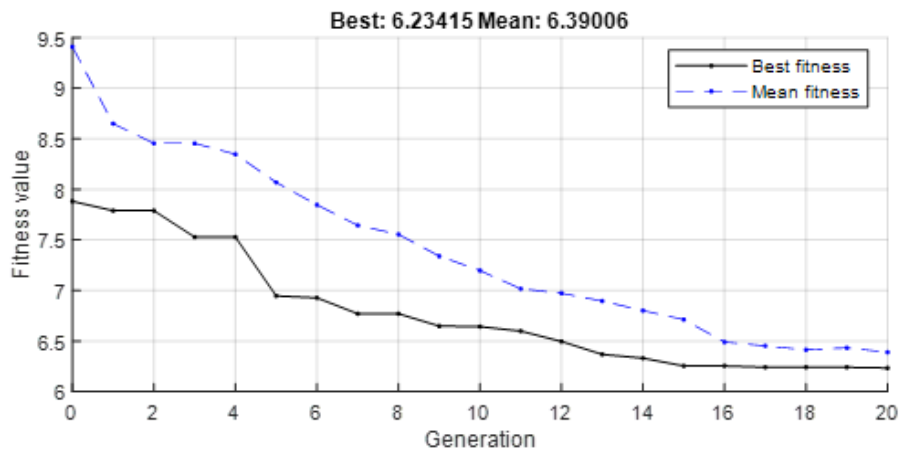


**Figure 5-25: Best and Mean fitness values for GA optimization**

## Results of GA with DoE

The next procedure is introducing the DoE analysis result into the GA algorithm. Here, the ranges of GA upper and lower bounds for those tuning parameters are adjusted according to their significance based on the DoE analysis that we obtained for the experimental test. For instance, the  $R_{roll}$  parameter in the R matrix has the highest range while the gyro y time constant has the lowest range referring to the pareto charts shown in Figure 5-23. Figure 5-27 shows the best, worst and means scores obtained with the use of DoE plotted on a graph of fitness value versus generation. In comparison to Figure 5-25, when DoE is utilized as proven by the result it takes less number of generations for the mean fitness to converge to the best individual fitness value, due to DoE finding the most effective factors and minimizing the search window for the GA. Figure 5-26 shows the comparison of GA without DoE and GA with DoE tested on real data. From the figure, it can be concluded that GA with DoE was able to find a fitness value with better accuracy in less generations (shorter time) compared to GA without DoE. Table 5-8 summarizes the magnitudes showing the performance of the EKF using GA and DoE.

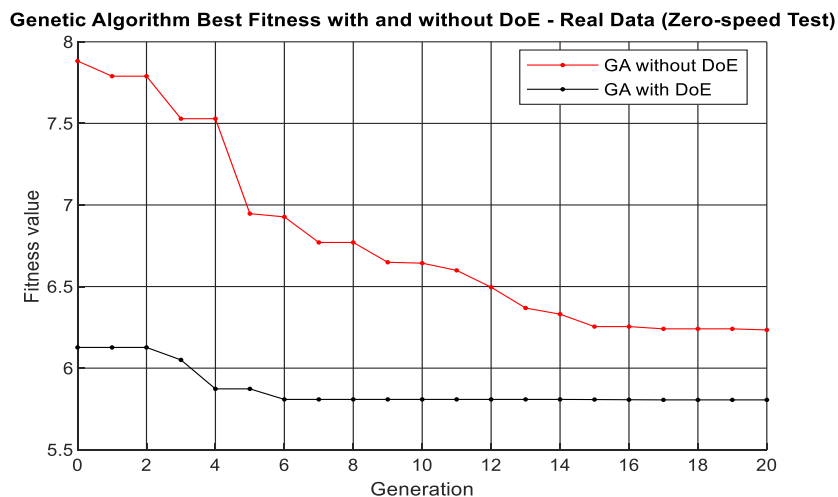
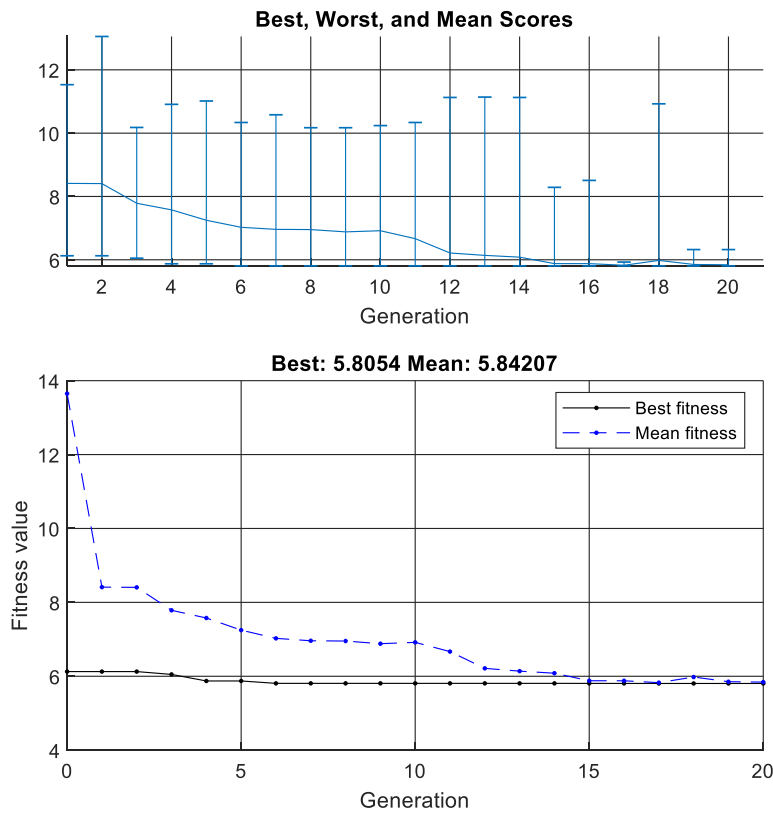


Figure 5-26: GA fitness with and without DoE for the zero-speed experimental test



**Figure 5-27: Fitness Value Statistics of GA with DoE**

**Table 5-8: Performance of DoE-supported GA for zero-speed experimental test**

	<b>RMSE(deg)</b>
<b>Roll</b>	0.21°
<b>Pitch</b>	0.13 °
<b>Heading</b>	3.50 °
<b>Overall Orientation Error</b>	3.51 °

### 5.3 Dynamic Physical Test

In this test, the MPU-9250 MEMS IMU was used with a GPS receiver (Ublox EKV-7) to collect GPS and IMU data on a moving land vehicle. This scenario is designed to test the performance of the proposed tuning method when the IMU is mounted to a dynamic platform.

#### 5.3.1 Ground-Truth Data

In this test, the ground truth has been generated by applying an INS/GPS filtering system available in the EMS lab [70]. This is an advanced EKF that performs full 3D IMU/GPS integration. The trajectory taken in this test is shown in Figure 5-28. Ground-truth orientation is shown in Figure 5-29 and Figure 5-30.

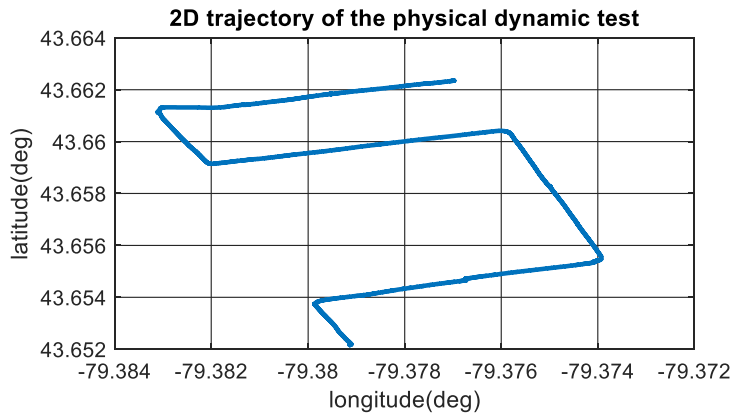


Figure 5-28: 2D trajectory taken in the dynamic test

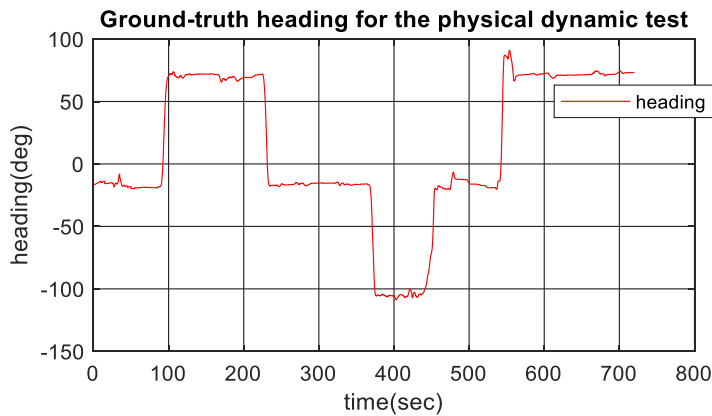


Figure 5-29: Ground-truth heading of the dynamic test

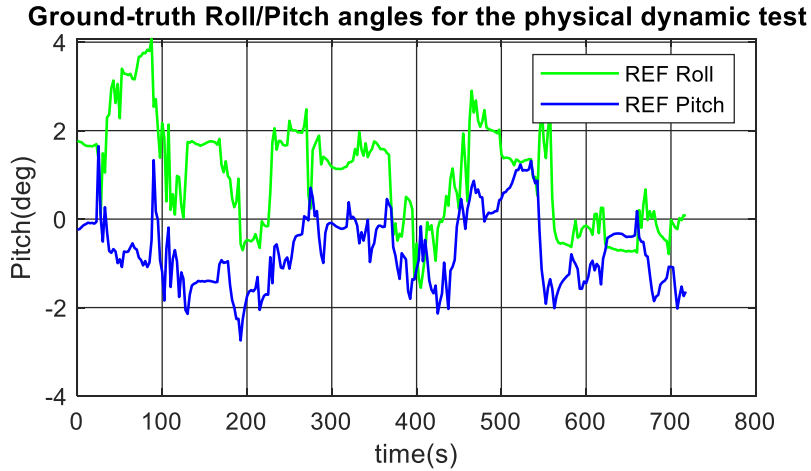


Figure 5-30: Ground-truth roll/pitch in the dynamic test

### 5.3.2 Raw IMU

Before using the raw accelerometer to calculate tilt angles, it was compensated for motion such that the accelerometer readings are only the gravity components that can be used for pitch/roll calculation. The heading updates was calculated by adding random noise to the ground truth heading. The raw gyro and the raw compensated accelerometer measurements are shown in Figure 5-31 and Figure 5-32.

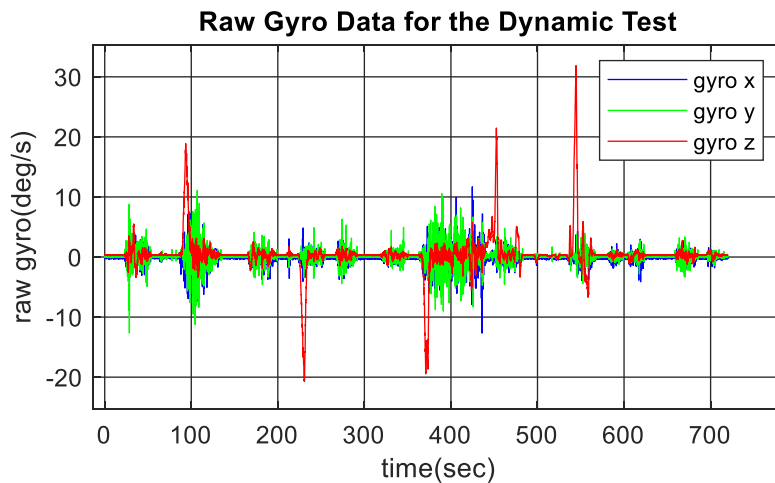


Figure 5-31: Raw gyroscope data of the dynamic test

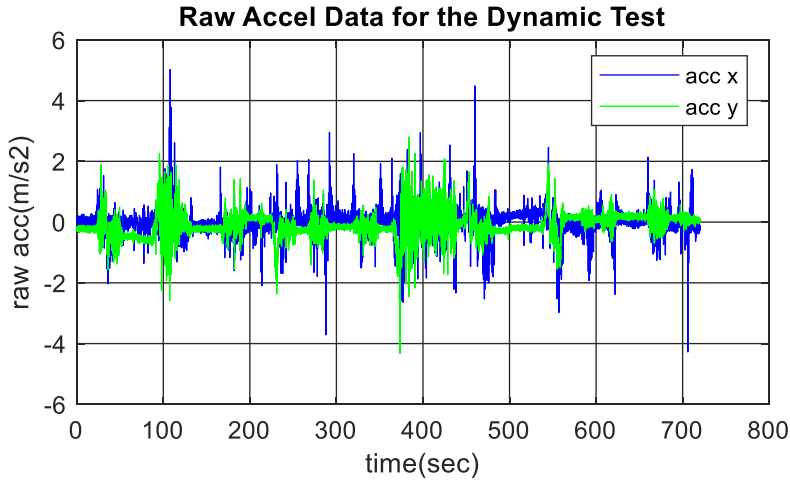


Figure 5-32: Raw X,Y accelerometer data of the dynamic test

### 5.3.3 Nominal Design Point Results on Experimental Dynamic Test

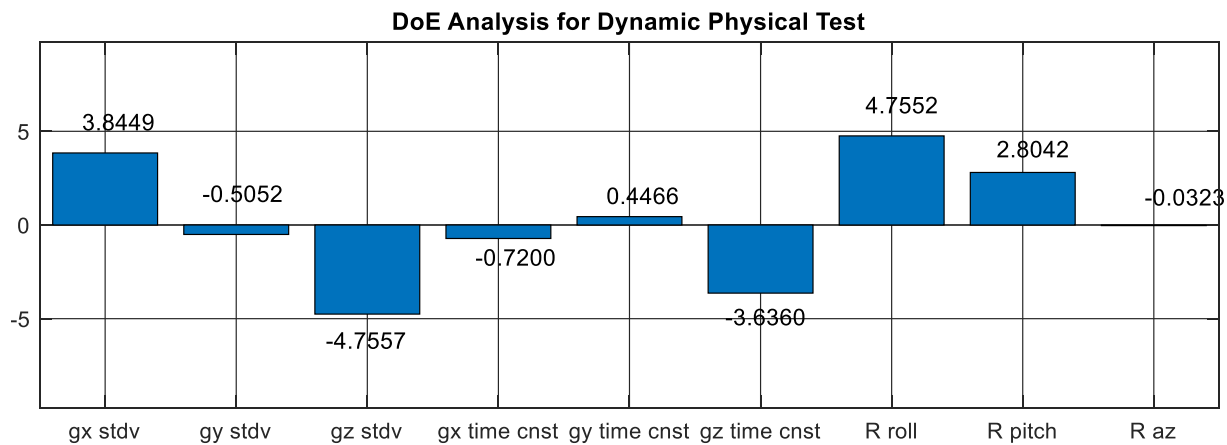
Table 5-9 shows the nominal design point results are of the dynamic experimental test. It is noticed that the orientation accuracy is better on the dynamic test than the static (stationary test). This is mainly due to two factors, 1) the usage of heading updates from GPS/INS integrated solution which is known to be better than magnetometer-driven heading. 2) the lower sampling rate which was 20Hz in this dynamic test. As discussed earlier, random walk effect is smaller when sampling rate is slower.

Table 5-9: EKF Results for dynamic experimental test using nominal design point

	RMSE(deg)
<b>Roll</b>	1.6°
<b>Pitch</b>	0.75°
<b>Heading</b>	2.01°
<b>Overall Orientation Error</b>	2.6763°

### 5.3.4 GA Results on Dynamic Experimental Test

We used the same computer platform with the same GA settings to run the tuning algorithm. In this time, we run the GA with DoE directly. The DoE analysis is shown in Figure 5-33. From Figure 5-33, it is evident that R roll, gyro z stdv, and gyro z time constant are the most significant factors affecting the EKF tuning than the rest of the factors. Figure 5-34 shows the best, worst and mean scores obtained with the use of DoE plotted on a scale of fitness value versus Generation. As shown on the bottom graph of the figure, it takes few generations for the mean fitness to converge to the best fitness, as DoE helps focus GA's search for the optimum fitness value.



**Figure 5-33: DoE Analysis for the dynamic experimental test**

Orientation is calculated from the GA by setting the lower and upper bound for each of those parameters using DoE analysis result. Figure 5-35 illustrates the similarities between heading angle output from this algorithm and ground truth dynamic data in degrees, both plotted against time in seconds. From observation, heading and ground truth yield similar curves between 0 to 700 second interval but those small errors added up to give  $0.9^{\circ}$  RMS error which accounts for the largest contribution in the overall orientation error.

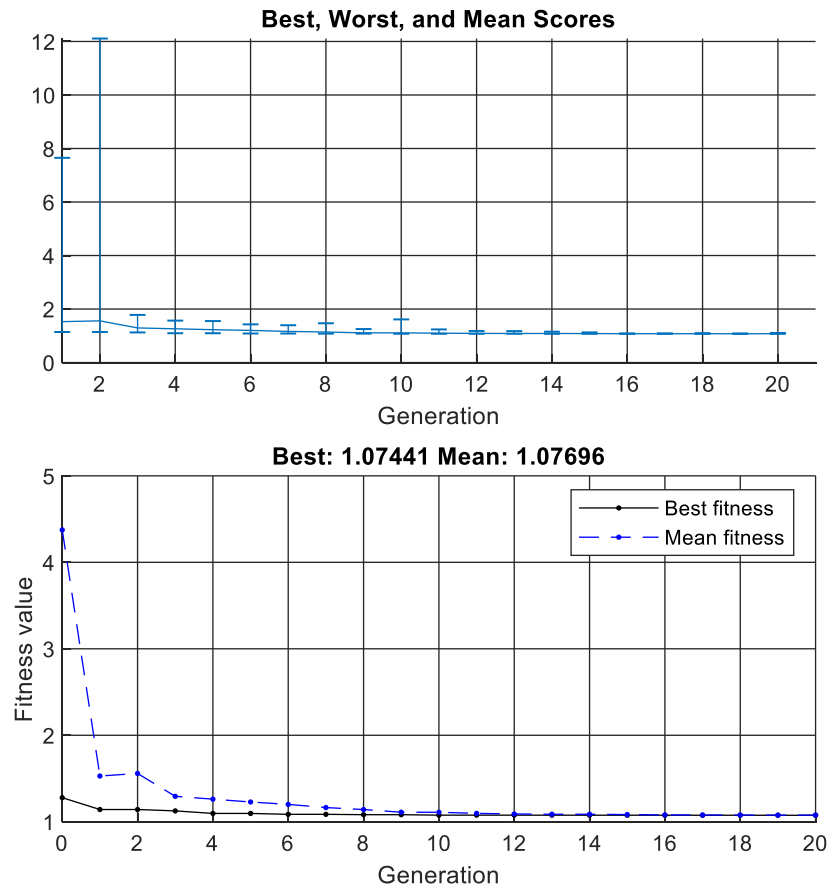


**Figure 5-34: Fitness Statistics of DoE-supported GA applied on dynamic experimental data**

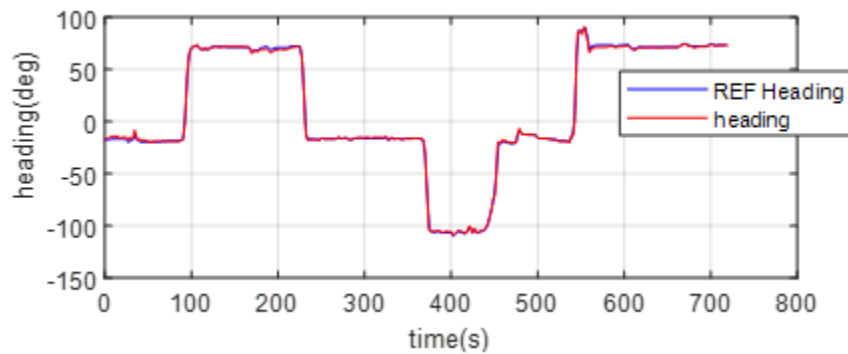


**Figure 5-35: Heading output for the dynamic physical test using GA with DoE**

Similarly, Figure 5-36 plots reference pitch against pitch calculated using GA and DoE on the dynamic physical data, versus time in seconds. Although there isn't much difference in the

curve between the pitch from the algorithm and reference pitch, the former is noisier which is due to gyro drifts.

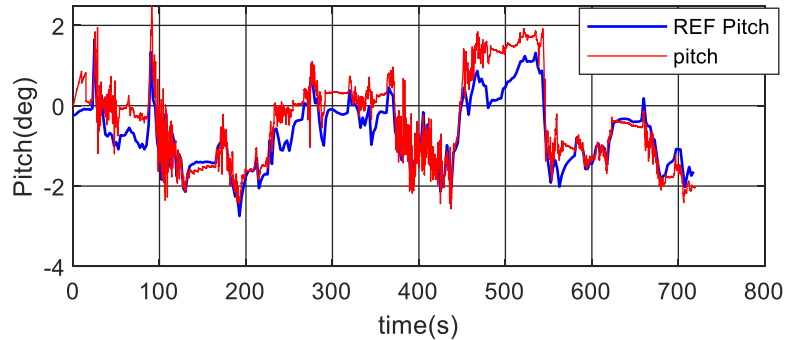


**Figure 5-36: Pitch output for the dynamic experimental test using GA with DoE**

Figure 5-37 shows the comparison between roll after the GA is implemented with DoE and the ground truth roll angle in degrees on the vertical side and time in seconds on the horizontal axis. The resulting roll doesn't deviate that much from the reference roll in the first half of the period except for being noisier. But in the latter stages, after about the 500<sup>th</sup> seconds time, the difference between the two gets larger.

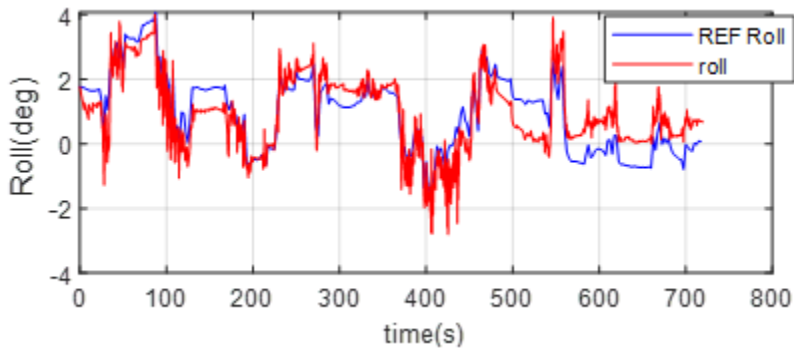


**Figure 5-37: Roll output for dynamic experimental test using GA with DoE**

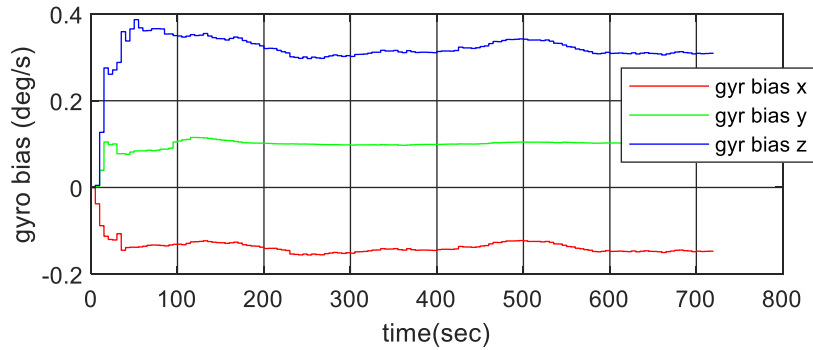


**Figure 5-38: Gyro biases for the dynamic test**

The gyro biases estimation in Figure 5-38 show that gyro x has the highest biases compared to the gyros in the y and z direction. Table 5-10 shows a summary of the overall orientation error in RMS error with the heading RMS error being the largest.

**Table 5-10: EKF-Performance for dynamic experimental Test**

	RMSE(deg)
<b>Roll</b>	0.6013°
<b>Pitch</b>	0.4755°
<b>Heading</b>	0.9°
<b>Overall Orientation Error</b>	1.074°

#### 5.4 Comment on Execution Time and Error values

The execution time and overall orientation error values of all tests are summarized in Table 5-11. As mentioned in section 5.1, the experiments were performed using the GA optimization using MATLAB R2018a GA toolbox on a TOSHIBA laptop with intel-iCore7 dual-core 2.4 GHz processor with 16GB RAM running Windows 10. To have a feeling of how these execution times compared to exhaustive search (trying all combinations), assuming we will change the 9 parameters where each parameter will be portioned into 5 values leading to 1953125 combinations.

The EKF execution time of one data epoch was averaged at 2 seconds. This means that the execution time to try all combinations is approximately 45 days! This simple analysis shows the efficiency of the GA-based search. Of course, other evolutionary-inspired search methods can be explored and compared to GA. However, this work is beyond the scope of this thesis.

It is difficult to develop a concrete accurate conclusion about typical AHRS error values of MEMS-based AHRS products. Different products report error values under different scenarios and conditions and it is difficult to verify these numbers in practice. However, to assess the accuracy of the developed AHRS in this thesis with respect to commercial AHRS, the error values of the MTi-G-710 AHRS commercial product is used as a reference which uses MEMS-based IMU. The MTi-G-710 AHRS overall orientation error value is reported as 1.67° [71] for dynamic tests which is slightly larger than the error value shown in Table 5-11 for the dynamic test. Given the reduction in tuning time and the systemic nature of the proposed technique, the advantages of the proposed parameter tuning method are clear.

**Table 5-11: Information summary of all experiments**

<b>Test</b>	<b>Sampling Rate</b>	<b>IMU Samples</b>	<b>Execution Time (minutes)</b>	<b>RMSE(°)</b>
Simulation	100 Hz	50000	90.41	0.4819
Zero-speed	100 Hz	13500	35.16	3.51
Dynamic	20 Hz	14400	26.96	1.074

## 6 Chapter: Conclusion

This thesis studied the MEMS-IMU error analysis using two common techniques; Allan Variance and Gauss-Markov random process modeling. The thesis then focused on one of the most important applications of MEMS-IMU which is Attitude and Heading Reference Systems (AHRS). The AHRS system model which are used to process raw IMU gyroscope measurements to calculate 3D orientation have been demonstrated. The effect of the IMU sensors errors have been shown by applying the AHRS system model to noisy raw gyroscope data. It was noticed that the IMU noise lead to significant error growth overtime. To limit this error growth, absolute tilt/heading angle updates from gravity measurements and magnetometer measurements were investigated. Although the tilt/heading angles calculated from accelerometer/magnetometer are absolute and they do not drift with time, they are very noisy. Therefore, Kalman filter was applied to fuse information from AHRS system model and tilt/heading angles measurements calculated from accelerometer/magnetometer.

Process noise and measurement noise parameters of AHRS are key values that affect the accuracy of Kalman filter. To tune noise parameters, this thesis developed a systematic approach that follows the following steps:

1. Allan Variance was used to estimate gyroscope high-frequency noise (random walk).
2. Gauss-Markov random process modeling was used to model gyroscope biases errors.
3. Initial value for measurement noise covariance was selected empirically.
4. Step 1,2 and 3 are used to obtain an initial design point (nominal design point).
5. Given a nominal design point, Deign of Experiment technique was applied to investigate the most significant noise parameters.

6. Genetic Algorithms was applied to optimize the Gauss-Markov parameters and the measurement noise covariance.
7. The fitness function of the Genetic Algorithm is the error between the EKF output and a ground-truth data set.

The procedure was applied on three different cases; 1) simulation data, 2) physical stationary test and 3) physical dynamic test. In the simulation test, a ground truth angles set was used to simulate raw IMU data. The raw IMU data was contaminated by high-frequency random noise (random walk), and biases. As the noise parameters in the simulation are already known, the performance of the nominal design point was acceptable. Thus, the improved gain from applying genetic algorithm was only 32%. In the stationary real-data test, a physical IMU was used to perform simple rotations while stationary. The improvement gained by applying genetic algorithm and DoE was approximately 39%. In the dynamic test, data from GPS and IMU mounted on a moving vehicle was used. The absolute angles measurement updates were generated from raw accelerometer after removing the motion effect from the accelerometer reading. The improvement on the dynamic test data was approximately 60%. Overall, in all test cases, comparison between the nominal design point accuracy and the genetic-based accuracy was performed. Results showed that although the nominal design point may generate acceptable results. However, better accuracy and significantly enhanced performance is obtained when genetic algorithms are applied.

## **6.1 Contributions**

The contributions of this thesis can be summarized as follows:

1. The introduction of a systematic way of tuning EKF parameters for more accurate AHRS.

2. The proposed design approach optimizes the EKF-parameters using a hybrid approach that combines Allan Variance, Gauss-Markov stochastic modeling and Genetic Algorithms supported by Design of Experiment analysis. Experimental results showed that the proposed method performed approximately 40% better in zero-speed scenario and 60% better in dynamic test scenario in comparison with conventional methods (Allan Variance and Gauss-Markov only).
3. The other major contribution of this thesis is the systematic analysis approach to integrate DoE principle into GA. This novel idea of tuning EKF parameters for the AHRS using the DoE helps to give emphasis on those parameters that affect the performance the most. This led to 5-15% increased performance in the overall orientation RMS error and 60% in the number of generations required in the genetic algorithm to converge to better accuracy
4. The following two conference papers have been published out of this work:

[1] **M. Gessesse**, M.M Atia, “Enhancing UAV 3D Orientation Estimation using Design of Experiment and Genetically Optimized Kalman Filter”, the 3<sup>rd</sup> Virtual Geoscience Conference, Kingston, ON, Canada, August 2018.

[2] **M. Gessesse**, M.M Atia, “Multi-sensor Attitude and Heading Reference System using Genetically Optimized Kalman Filter”, 61st IEEE International Midwest Symposium on Circuits and Systems Windsor, ON, Canada August 5th-8th, 2018.

## 6.2 Future work

The work presented in this thesis opens new research directions for systematic tuning of EKF-based AHRS. These new directions can be summarized as follows:

1. Tightly-coupled tests: In thesis work, we applied the method on AHRS that reads absolute angle measurements. This is known as “loosely-coupled” mode. In tightly-coupled mode, AHRS reads directly raw accelerometer and magnetometer measurements data. Tightly-coupled mode generally lead to better performance.
2. The method can be applied in full 3D position/velocity/attitude estimation using GPS/INS EKF. The GPS/INS system is more complex, and it involved larger number of parameters to be tuned.
3. The thesis work applied the method in post-processing offline mode. However, a more beneficial scenario is to apply the method in real-time. This could be performed by collecting a buffer of GPS data as ground-truth and run the tuning in real-time on this buffer to optimize the EKF noise parameters online in the field.

## References

- [1] M. H. Moghari and P. Abolmaesumi, "Comparing Unscented and Extended Kalman Filter Algorithms in the Rigid-Body Point-Based Registration," in *2006 International Conference of the IEEE Engineering in Medicine and Biology Society*, New York, NY, USA, 2016.
- [2] Z. J. K. S and L. O, "INS/GPS Tightly-coupled Integration using Adaptive Unscented Particle Filter," *The Journal of Navigation*, vol. 63, no. 3, pp. 491-511, 2010.
- [3] J. Iannacci, *RF-MEMS Technology for High-Performance Passives*, IOP Publishing Ltd, 2017.
- [4] G.-e.-H. Mohamed, *MEMS: applications*, 2nd ed., CRC Press/Taylor & Francis, CRC Press, Chapman and Hall/CRC, 2006.
- [5] K. Volker, *Inertial MEMS - Principles and Practice*, Cambridge University Press, 2011.
- [6] P. Minha and G. Yang, "Error and Performance Analysis of MEMS-based Inertial Sensors with a Low-cost GPS Receiver," 2008.
- [7] F. J. Aided Navigation, *GPS with High Rate Sensors*, 1 ed., New York: McGraw Hill, 2008.
- [8] M. HENRY and G. PAUL, "The Limits of In-Run Calibration of MEMS Inertial Sensors and Sensor Arrays," *NAVIGATION, Journal of the Institute of Navigation*, vol. 63, no. 2, pp. 127-143, 2016.
- [9] H. Geng, Z. Wang and Y. Cheng, "Distributed Federated Tobit Kalman Filter Fusion Over A Packet-delaying Network: A Probabilistic Perspective," in *IEEE Transactions on Signal Processing*, 2018.
- [10] V. K. Madyastha, V. C. Ravindra, S. M. Vaitheeswaran and S. Mallikarjunan, "A novel INS/GPS fusion architecture for aircraft navigation," in *2012 15th International Conference on Information Fusion*, Singapore, Singapore, 2012.
- [11] Z. Xing, Y. Xia, L. Yan, K. Lu and Q. Gong, "Multisensor Distributed Weighted Kalman Filter Fusion With Network Delays, Stochastic Uncertainties, Autocorrelated, and Cross-Correlated Noises," *IEEE Transactions on Systems, Man, and Cybernetics: Systems*, vol. 48, no. 5, pp. 716 - 726, 2018.
- [12] G. B. Robert and Y. H. Patrick, *Introduction to Random Signals and Applied Kalman Filtering*, 4th ed., New York: John Wiley, 2012.
- [13] N. Michał, W. Jan and S. Piotr, "Simplicity or Flexibility? Complementary Filter vs. EKF for Orientation Estimation on Mobile Devices," in *2015 IEEE 2nd International Conference on Cybernetics (CYBCONF)*, Gdynia, 2015.
- [14] Y. tawk, P. Tome, C. Botteron and P. Andre, "Implementation and Performance of a GPS/INS Tightly Coupled Assisted PLL Architecture Using MEMS Inertial Sensors," *Sensors*, 2014.
- [15] C. Wang, B. Ran, J. Zhang and X. Qu, "A Novel Approach to Estimate Freeway Traffic State: Parallel Computing and Improved Kalman Filter," *IEEE Intelligent Transportation Systems Magazine*, vol. 10, no. 2, pp. 180 - 193, 2018.
- [16] G. Alcan and M. Unel, "Robust hovering control of a quadrotor using acceleration feedback," in *2017 International Conference on Unmanned Aircraft Systems (ICUAS)*, Miami, FL, USA, USA, 2017.
- [17] A. Quinchia, G. Falco, E. Falletti, F. Dovis and C. Ferrer, "A Comparison between Different Error Modeling of MEMS Applied to GPS/INS Integrated Systems," *Sensors*, vol. 13, no. 8, pp. 9549-9588, 2013.

- [18] E.-S. Naser, H. Haiying and N. Xiaoji, "Analysis and Modeling of Inertial Sensors Using Allan Variance," *IEEE Transactions on Instrumentation and Measurement*, vol. 57, no. 1, pp. 140-149, 2008.
- [19] M. Miroslav and Š. Mikuláš, "Computation and Evaluation Allan Variance Results," in *2016 New Trends in Signal Processing (NTSP)*, Demanovska Dolina, Slovakia, 2016.
- [20] A. P. S. Z. N. A and E.-S. N, MEMS-Based INTEGRATED NAVIGATION, Norwood, MA: Artech House, 2010.
- [21] L. Wen, L. Qingdong, F. Yao and R. Zhang, "Maneuvering Acceleration Assisted Attitude Algorithm Design Based on Fuzzy Adaptive Kalman Filter," in *Proceedings of 2014 IEEE Chinese Guidance, Navigation and Control Conference*, Yantai, China, 2014.
- [22] T. Xin, L. Zhaofeng, H. Guowei, L. Nan, S. Yan and N. Jin, "Adaptive EKF Based on HMM Recognizer for Attitude Estimation Using MEMS MARG Sensors," *IEEE Sensors Journal*, vol. 18, no. 8, pp. 3299 - 3310, 2017.
- [23] T. Tanaka, S. M and U. V, "Optimal sensor design and zero-delay source coding for continuous-time vector Gauss-Markov process," in *IEEE 56th Annual Conference on Decision and Control (CDC)*, 2017.
- [24] M. Rodrigo and G. Antoni, "An Attitude and Heading Reference System (AHRS) based in a Dual Filter," in *ETFA2011*, Toulouse, France, 2011.
- [25] K. L, Y. L, S. K and Z. Y, "Attitude Heading Reference System Using MEMS Inertial Sensors with Dual-Axis Rotation," *Sensors*, vol. 14, no. 10, 2014.
- [26] J. W. Oliver, "An introduction to inertial navigation," 2007.
- [27] D. Meyer and D. Rozelle, "Milli-HRG inertial navigation system," *Gyroscopy and Navigation*, vol. 3, no. 4, p. 227-234, 2012.
- [28] X. Wang and L. Xiao, "Gyroscope-reduced inertial navigation system for flight vehicle motion estimation," *Advances in Space Research*, vol. 59, no. 1, pp. 413-424, 2017.
- [29] W. Sun, D. Wang, L. Xu and L. Xu, "MEMS-based rotary strapdown inertial navigation system," *Measurement*, vol. 46, no. 8, pp. Pages 2585-2596, 2013.
- [30] C. VIKAS and I. KRZYSZTOF, Mems fundamental technology and application, 6000 Broken Sound Parkway NW, Suite 300: CRC Press, 2013.
- [31] D. G. Paul, Principles of GNSS, INERTIAL, and multisensory integrated navigation system, BOSTON, LONDON: ARTECH HOUSE, 2013.
- [32] . V. Giorgio and . B. Gianmarco, Theoretical framework for in-car navigation based on Integrated GPS/IMU technologies, Vols. 27042, 27042, Luxembourg, : Publications Office, 2015.
- [33] . V. Navratil, H. Xu, . C. Toth, D. G. Brzezinska and Z. Koppanyi, Using Adaptive Motion Constraints to Support UWB/IMU Based Navigation, 2018.
- [34] H. M. Georges, D. Wang and Z. Xiao, "GNSS/low-cost MEMS-INS integration using variational Bayesian adaptive cubature Kalman smoother and ensemble regularized ELM," in *Mathematical Problems in Engineering*, 2015.
- [35] C. Fan, X. Hu, X. He, K. Tang and B. Luo, "Observability Analysis of a MEMS INS/GPS Integration System with Gyroscope G-Sensitivity Errors," *Sensors*, vol. 14, no. 9, 2014.

- [36] Y. Li, M. Efatmaneshnik and A. G. Dempster, "Attitude determination by integration of MEMS inertial sensors and GPS for autonomous agriculture applications," *GPS Solutions*, vol. 16, no. 1, p. 41–52, 2012.
- [37] V. M. Tereshkov, "A Simple Observer for Gyro and Accelerometer Biases in Land Navigation Systems," *The Journal of Navigation*, vol. 68, no. 4, pp. 635-645, 2015.
- [38] T. Y.K, W. M.S, C. J.A, H.-G. B.R and J. D.A, "Numerical double integration of acceleration measurements in noise," *Measurement*, vol. 36, no. 1, pp. 73-92, 2004.
- [39] R. Mebarki, V. Lippiello and B. Siciliano, "Vision-based and IMU-aided scale factor-free linear velocity estimator," *Autonomous Robots*, vol. 41, no. 4, p. 903–917, 2016.
- [40] G. W, B. J, B. U, G. W, H. M and H. E, "MEMS IMU for AHRS applications," in *2008 IEEE/ION Position, Location and Navigation Symposium*, Monterey, CA, USA, 2008.
- [41] J.-O. Nilsson and H. Peter, "Aligning the Forces—Eliminating the Misalignments in IMU Arrays," *IEEE Transactions on Instrumentation and Measurement*, vol. 63, no. 10, pp. 2498-2500, 2014.
- [42] J. Liu, . D. Wang, H. Wang and Y. Fan, "A Rigorous Approach for IMU Boresight Misalignment Calibration," in *2011 International Workshop on Multi-Platform/Multi-Sensor Remote Sensing and Mapping*, Xiamen, China, 2011.
- [43] B. R.k, L. Road, I. Shaveta and P. Ramjai, "An Improved Analytical Approach for Estimation of Misalignment Error of Sensing Axis in MEMS Accelerometers using Simple Tilt Measurements," *Sensors & Transducers*, vol. 189, no. 6, pp. 128-136, 2015.
- [44] M. M. Atia, *Multi-Sensor Integrated Navigation in Urban and Indoor Environments: GNSS, Inertial, and Range Sensors Integration*, K. Yu, Ed., Idea Group Inc, 2018, p. 46.
- [45] B. Altinoz and D. Unsal, "Look up table implementation for IMU error compensation algorithm," in *2014 IEEE/ION Position, Location and Navigation Symposium - PLANS*, 2014.
- [46] U. D and D. K, "Estimation of deterministic and stochastic IMU error parameters," in *Proceedings of the 2012 IEEE/ION Position, Location and Navigation Symposium*, 2012.
- [47] Z. Hongyu, W. Zhelong, S. Hong, H. Weijian and Q. Gao, "A time-controllable Allan variance method for MEMS IMU," *INDUSTRIAL ROBOT: AN INTERNATIONAL JOURNAL*, vol. 40, no. 2, pp. 111-120, 2013.
- [48] M. . H. Elder, "MEMS IMU stochastic error modelling," *Systems Science & Control Engineering*, vol. 5, no. 1, pp. 1-8, 2016.
- [49] P. G. Savage, *Strapdown Analytics - Second Edition*, MN, USA: Strapdown Associates, Inc., 2000.
- [50] P. S, "Determining pitch and roll in inexpensive land navigation systems," *J. Aeronautica Integra*, vol. 1, no. 3, p. 93–97, 2008.
- [51] H. M and K. C, "Dual-axis tilt sensor based on micromachined accelerometers," *Sensors*, vol. 3, no. 4, p. 91–94, 1996.
- [52] F. I, P. F and A. B. N, "Autocalibration of triaxial MEMS accelerometers with automatic sensor model selection," *IEEE Sensors Journal*, vol. 12, no. 6, p. 2100–2108, 2012.
- [53] Ł. S, O. W and B. M, "Sensing tilt with MEMS accelerometers," *IEEE Sensors Journal*, vol. 6, no. 6, p. 1669–1675, 2006.
- [54] Ł. Sergiusz, G. Robert and B. Maciej, "Selection of MEMS Accelerometers for Tilt Measurements," *Journal of Sensors*, vol. 2017, no. 9796146, 2017.

- [55] A. Sanketh, "GPS Aided Attitude and Heading Reference System using MEMS Sensors," in *2016 Indian Control Conference (ICC)*, Hyderabad, India, 2016.
- [56] S. Mie, Y. Okuyama, Y. Sato, Y. Chan, N. K. Dang and B. A. Abderazek, "Real-Time UAV Attitude Heading Reference System Using Extended Kalman Filter for Programmable SoC," in *2017 IEEE 11th International Symposium on Embedded Multicore/Many-core Systems-on-Chip (MCSoc)*, Seoul, South Korea, 2017.
- [57] H. Tang and Z. Shen, "An attitude estimate method for fixed-wing UAV s using MEMS/GPS data fusion," in *2017 First International Conference on Electronics Instrumentation & Information Systems (EIIS)*, Harbin, China, 2017.
- [58] . M. T. Sabet, . H. M. Daniali, A. Fathi and E. Alizadeh, "A Low-Cost Dead Reckoning Navigation System for an AUV Using a Robust AHRS: Design and Experimental Analysis," *IEEE Journal of Oceanic Engineering*, vol. PP, no. 99, pp. 1-13, 2017.
- [59] V. Avrutov, D. Buhaiov and V. Meleshko, "Gyrocompassing Mode of the Attitude and Heading Reference System," in *2017 IEEE 4th International Conference Actual Problems of Unmanned Aerial Vehicles Developments (APUAVD)*, Kiev, Ukraine, 2017.
- [60] H. Yahua, G. Jiachao, Y. Tianyi, W. Cheng, YufengJin and S. Guangyi, "High Accuracy Extend Kalman Filter for Posture Measurement based on Attitude and Heading Reference System," in *2017 IEEE International Conference on Real-time Computing and Robotics (RCAR)*, Okinawa, Japan, 2017.
- [61] J. Antony, *Design of Experiments for Engineers and Scientists*, 2nd ed., Burlington, 2014.
- [62] G. Peter and J. Bradley, *Optimal Design of Experiments*, John Wiley & Sons, Incorporated, 2011.
- [63] D. Cox and N. Reid, *The theory of the design of experiments*, Chapman & Hall/CRC, 2000.
- [64] J. Shiqiang, F. Weiping, L. Dexin and W. Wen, "Research on Application of Genetic Algorithm for Intelligent Mobile Robot Navigation Based on Dynamic Approach," in *2007 IEEE International Conference on Automation and Logistics*, Jinan, China, 2007.
- [65] G.-O. J, R. D.R, L.-M. D and C. E.F, "Genetic algorithms based predictive control for mobile robot navigation in changing environments," Porto, Portugal, 2001.
- [66] V. d. O. Átila and A. F. Marcelo, "Dynamic Planning Navigation Technique Optimized with Genetic Algorithm," in *2014 Joint Conference on Robotics: SBR-LARS Robotics Symposium and Robocontrol*, Sao Carlos, Brazil, 2014.
- [67] R. Qian, W. Bo, D. Zhihong and F. Mengyin, "An optimization self-calibration method of rotational inertial navigation system based on genetic algorithm," in *Proceedings 2013 International Conference on Mechatronic Sciences, Electric Engineering and Computer (MEC)*, Shengyang, China, 2013.
- [68] X. Yang and Y. Jia, "Optimization of control parameters based on genetic algorithms for spacecraft attitude tracking with input constraints," *Nerocomputing*, vol. 177, pp. 334-341, February 2016.
- [69] S. Poddar, S. Hussain, S. Ailneni, V. Kumar and A. Kumar, "Tuning of GPS aided attitude estimation using evolutionary algorithms," *International Journal of Intelligent Unmanned Systems*, vol. 4, no. 1, pp. 23-42, 2016.
- [70] Carleton University, "Embedded Multi-sensor Systems (EMS) Lab," 1 9 2016. [Online]. Available: <https://carleton.ca/embedded-systems/>. [Accessed 2018 7 11].
- [71] Xsens, "MTi-G-710," Xsens, [Online]. Available: <https://www.xsens.com/products/mti-g-710/>. [Accessed 1 August 2018].

- [72] E. Ezzaldeen, Z. Junchuan, Z. Jieying and L. Otmar, "A New Loosely Coupled DCM Based GPS/INS Integration Method," 2012.
- [73] X. Linlin, W. Jianguo and L. Yindong, "Quadratic EKF algorithm enhancements for low cost tightly-coupled AHRS/GPS," 2008.
- [74] M. Grewal and A. Andrews, Kalman Filtering Theory and Practice, Englewood Cliffs, NJ: Prentice-Hall, 1993.
- [75] B. Marian, G. Rafal, C. Roman and S. Grzegorz, "Attitude and Heading Reference System Based on 3D Complementary Filter," in *2014 19th International Conference on Methods and Models in Automation and Robotics (MMAR)*, Miedzydroje, Poland, 2014.
- [76] S. Abolfazl and A. H. Mazinan, Mathematical modeling of spacecraft guidance and control system in 3D space orbit transfer mission, Springer International Publishing, 27 October 2015.
- [77] D. Slanzi, D. D. Lucrezia and I. Poli, Querying Bayesian networks to design experiments with application to IAGY serine esterase protein engineering, European Centre for Living Technology, Ca' Minich, S. Marco 2940, 30124 Venice, IT: Elsevier, 15 December 2015.
- [78] N.-S. Pai, W.-C. Li, M.-H. Chou and P.-Y. Chen, "Flight control for a quadrotor of attitude control based on android system and using optimal-tuning design," *Computers & Electrical Engineering*, vol. 54, no. 1, pp. 170-184, August 2016.
- [79] M. TayyebTaher and S. M. Esmailzadeh, "Model predictive control of attitude maneuver of a geostationary flexible satellite based on genetic algorithm," *Advances in Space research*, vol. 60, no. 1, pp. 57-64, July 2017.
- [80] A. Rezvani, M. Izadbakhsh and M. Gandomkar, "Microgrid dynamic responses enhancement using artificial neural network-genetic algorithm for photovoltaic system and fuzzy controller for high wind speeds," *International Journal of Numerical Modelling*, vol. 29, no. 2, 15 June 2015.
- [81] Z. Chen, L. Zhong, X. Liu and B. Cong, "Adaptive Fuzzy PD+ Control for Attitude Maneuver of Rigid Spacecraft," vol. 18, no. 2, 20 March 2015.
- [82] Analog Devices, "ADIS16475 (Rev. A)," 2017. [Online]. Available: <http://www.analog.com/media/en/technical-documentation/data-sheets/ADIS16475.pdf>. [Accessed 08 07 2018].
- [83] Analog Devices, "ADIS16475 (Rev. A)," 2017. [Online]. Available: <http://www.analog.com/media/en/technical-documentation/data-sheets/ADIS16475.pdf>. [Accessed 08 07 2018].
- [84] J. Antony, Design of Experiments for Engineers and Scientists, Ed.: 2nd ed. Burlington , 2014.
- [85] P. Maussion, "Design of Experiments in electrical engineering: Applications in control and modeling," in *IEEE*, Nottingham, UK, 2017.
- [86] M. Tawfik, S. Monteso, F. Garcia-Loro, E. Sancristobal, E. Ruiz, G. Díaz, A. C. Santo, J. Peire and M. Castro, "Computer Applications in Engineering Education," *Novel design and development of advanced remote electronics experiments*, pp. 327- 336, May 2015.
- [87] InvenSense Inc., "RS-MPU-6000A-00," 19 08 2013. [Online]. Available: <https://www.invensense.com/wp-content/uploads/2015/02/MPU-6000-Register-Map1.pdf>. [Accessed 09 07 2018].
- [88] InvenSense Inc, 17 01 2014. [Online]. Available: [https://cdn.sparkfun.com/assets/learn\\_tutorials/5/5/0/MPU9250REV1.0.pdf](https://cdn.sparkfun.com/assets/learn_tutorials/5/5/0/MPU9250REV1.0.pdf). [Accessed 08 07 2018].

[89] Natural Resources Canada, "Magnetic field calculator," Natural Resources Canada, [Online]. Available: <http://www.geomag.nrcan.gc.ca/calc/mfcal-en.php>. [Accessed 11 7 2018].